Quantitative Physiologically-Based Sleep Modeling: Dynamical Analysis and Clinical Applications

A thesis submitted for the degree of
Masters of Science

by

Benjamin D. Fulcher

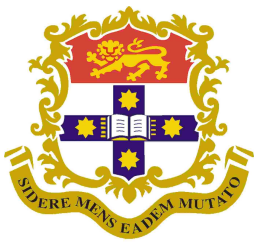

School of Physics
University of Sydney
Australia

September 2008

Declaration of originality

To the best of my knowledge, this thesis contains no copy or paraphrase of work published by another person, except where duly acknowledged in the text. Excepting parts of the mathematics presented in Sec. 2.3.2, which is based on work from my Honours thesis, this Masters thesis contains no material which has previously been presented for a degree at the University of Sydney or any other university.

Benjamin D. Fulcher

Included papers and attribution

Listed below are details of the papers on which Chapters 2 to 4 are closely based.

Chapter 2 **Modeling the Impact of Impulsive Stimuli on Sleep-Wake Dynamics**

B. D. Fulcher, A. J. K. Phillips, P. A. Robinson

Submitted to *Phys. Rev. E*

I was primarily responsible for this work, with an overall contribution of about 80%.

Chapter 3 **Physiologically-Based Modeling of Subjective Fatigue During Sleep Deprivation**

B. D. Fulcher, A. J. K. Phillips, P. A. Robinson

To be submitted to *J. Sleep Res.*

I was primarily responsible for this work, with an overall contribution of about 90%.

Chapter 4 **A Quantitative Physiologically-Based Model of the Sleep-Wake Switch Including the Orexin Group**

B. D. Fulcher, A. J. K. Phillips, P. A. Robinson

To be submitted to *J. Theor. Biol.*

I was primarily responsible for this work, with an overall contribution of about 90%.

Acknowledgements

I would like to thank a number of people for aiding my health, sanity, happiness, and academic development.

Firstly I would like to thank Prof. Peter Robinson for supervising this work. Feedback on manuscripts was always rapidly delivered and helpful. I thank Peter especially for his support in the weeks leading to the submission of this thesis. I have learnt a lot about research science and the processes involved in doing a good job of it from preparing this thesis, much of which I have Peter to thank for. I now feel much more confident as a research scientist from what I have learnt during my time in the Complex Systems group.

I would also like to thank Andrew Phillips for his frequent, helpful, and informative discussions throughout the year. His chair but 8.5 baby steps from mine, Andrew was always willing to help, keeping my sometimes crazy ideas in check, and providing invaluable insights into the model (which is, after all, his) and its implications for the wider field. Feedback on manuscripts was always detailed and helpful. His suggestion to explicitly model $\mathcal{T}$ using the inverse square scaling relationship known from saddle-node bifurcation theory, was particularly high-five worthy. I now use the backslash-comma convention between numbers and units, a revolution in the way I now use LaTeX. Andrew's sympathy towards my sense of humour, including "butch" manuscript additions, and "confirmed acid-head" phrases was also much appreciated. It is indeed a privilege for any one to be part of a workplace with access to "sensitive male nancy boys" right next door – they are amongst the best MET PEOPLE I've ever... I have had many maximums of enjoyment, have witnessed many extremums in behaviour, yet have never experienced any minimums in enjoyment

during my visits to Room 373.

I thank my family for their love and support, throughout this year and throughout my life. Crucial to both my personality and this thesis has been their unconditional encouragement and support. Finally, I'd like to thank my friends. Their company has enabled me to maintain sufficiently good spirits to continue making the trek in to my office to press *F5* some more. In the language of the proposed fatigue model of Chapter 3, their application of $W_{\text{happiness}}$ at high $D_{\text{what's the point}}$ has kept me from incurring 'catastrophic lapses' in spirit. Firstly, the Thai brigade: Felix, Dekker, Hugo, Parry, Matt, and Alex (in decreasing order of dedication) for their company and belief in the cause. The daily Sahand-led *Campos* pilgrimage is a ritual that I have become dependent upon, with the intoxicating ambience now beginning to infuse itself into the rest of my life, not to mention the grotesque catch-phrases. The evolved holiday crew: Anuey, Harshini, Jacqui, Mee-Eun, Shana, Stasie, and Tristan are amongst the most beautiful people in the world and have made a huge contribution to my W drive, particularly at high D when it's the most needed [c.f., Fig. 3.5(b)]. Ok, getting there, to Saranpaal and Nuwan for thinking the way I do, to Barry, Parth, and Dado for being simply great guys, to Lai for being herself, and to bf-Ying for some inspiring starts to the day. Last, but not least, I'd like to thank myself for writing such a comprehensive set of acknowledgments.

Summary

In this thesis, a recently developed physiologically-based model of the sleep-wake switch [1] is analyzed and applied to a variety of clinically-relevant protocols. In contrast to phenomenological models, which have dominated sleep modeling in the past, the present work demonstrates the advantages of the physiologically-based approach. Each of the three chapters containing new research, Chapters 2–4, is self-contained and includes its own abstract, introduction, summary, and discussion. However, the chapters are intended to be read in order, with each chapter assuming some familiarity with the content of the previous chapter(s).

Chapter 1 contains a brief overview of the sleep research field and places the new research contained in this thesis within this wider context. In particular, the role of sleep modeling in the field is explained, and the physiologically-based approach used throughout this work is distinguished from other methodologies. The Phillips-Robinson sleep model, which is used throughout this thesis, is also introduced.

Chapter 2 contains dynamical and linear stability analyses of the Phillips-Robinson model, including a general framework for determining its response to arbitrary external stimuli. The effects of near-stable wake and sleep *ghosts* on the model's dynamics are investigated, and the results are interpreted in terms of their behavioral significance. The wake ghost, for example, provides a mechanism for stabilizing brief awakenings during sleep, and suggests a method for simulating fatigue during sleep deprivation (as treated in Chapter 3 of this thesis). A separation of the model time scales forms the motivation for

a convenient two-dimensional representation in which to analyze the model's response to impulse external stimuli. The remainder of Chapter 2 demonstrates the utility of this framework by applying it to impulsive sensory stimuli during sleep, which are modeled according to their known physiological mechanism. Identifying the wake ghost as a sensible definition of 'wake' allows us to define the arousal threshold, whose predicted variation is found to match experimental data from the literature. In simulating a sleep fragmentation protocol, the model simultaneously reproduces the body temperature and arousal threshold variation measured in another existing clinical study.

Chapter 3 exploits the dynamical analysis undertaken in Chapter 2, focusing on the role of the wake ghost as a waking state at high values of the model's sleep drive. However, in this chapter the dynamics are explained in non-mathematical, qualitative terms for an intended clinical audience. To simulate sleep deprivation, an addition *wake-effort* drive is required to maintain wakefulness during normal sleeping periods. We interpret this drive both physiologically and psychologically, and demonstrate quantitative agreement between the model's output and experimental subjective fatigue-related data. As well as subjective fatigue, the model is simultaneously able to reproduce adrenaline excretion and body temperature variations. The physiological modeling approach allows us to elucidate connections between clinically-measurable quantities and the physiological interactions and drives that produce them.

In Chapter 4, the model is extended to include the orexinergic neurons of the lateral hypothalamic area. The equations governing the extended model are analyzed rigorously and used as a basis for interpreting its dynamics. Using the general framework developed in Chapter 2 for incorporating external stimuli into the model, we present a new representation for understanding how external influences acting over long time scales produce changes to the model's fundamental equilibrium structure. Due to the dynamics of the orexin group, the extended model exhibits sleep inertia, and an inhibitory circadian projection to the orexin group produces a postlunch dip in performance – both of which

are well-known behavioral features. Including both homeostatic and circadian inputs to the orexin group, the model produces a waking arousal variation that quantitatively matches published clinical data.

A summary of the main results of the thesis and suggestions for future research directions are discussed in Chapter 5.

Contents

Chapter 1

Overview

This thesis is concerned with a physiologically-based approach to quantitatively modeling the neuronal dynamics that give rise to sleep-wake dynamics. In this chapter, a brief overview of background and associated sleep research material is presented to put the new research of Chapters 2–4 into context. Key aspects of the field of sleep research are briefly summarized in Sec. 1.1, focusing predominantly on the role of sleep modeling. The two main approaches to modeling sleep-wake dynamics are then compared: phenomenological sleep models are discussed in Sec. 1.2, followed by physiologically-based models in Sec. 1.3. Some of the open questions for sleep modeling are discussed in Sec. 1.4. Note that more specific and detailed information is given in each of Chapters 2–4 as required; this chapter is intended to provide a wider overview.

1.1 Sleep Research

Throughout human history the nature and purpose of sleep have been questions of fundamental interest. Sleep was initially thought to be an idle state of the mind and brain, being described by Robert MacNish in 1834 as "an intermediate state between wakefulness and death" [2]. However, with the discovery of the human electroencephalogram (EEG) [3] and rapid eye movements (REM),

sleep began to be recognized as an active and dynamic process.

Current sleep research involves a diverse range of disciplines, including clinicians, biologists, physiologists, mathematicians, neuroscientists, and theoreticians. Clinical studies cover a broad range of problems, including performance variation [4, 5], shift work, forced desynchronization and circadian and diurnal rhythms [6–11], sleep deprivation [12–15], sleep fragmentation [16–22], sleep restriction [23–27], and the impact of light [28–30], pharmaceuticals [31–37], and other sensory effects [38] on sleep-wake dynamics. Clinical sleep research can also help to suggest treatment for sleep-related pathologies including sleep apnea-hypopnea syndromes [39–45], restless legs syndrome [46], insomnia [47], and narcolepsy [48]. Physiologically-based studies aim to understand the neuronal-level interactions that govern arousal state dynamics. Relevant neuronal populations and their neuromodulatory interactions are investigated, including the impact of external drives and influences [49–55]. Theoretical studies aim to incorporate phenomenological and physiologically-based ideas into qualitative phenomenological [56], quantitative phenomenological [6, 57–61], and physiologically-based neuronal network [1, 62–64] models. As a whole, sleep models aid an intuitive and more detailed understanding of the timing of sleep and wake, have quantitative predictive power, and elucidate connections between clinical observations and the physiological mechanisms that produce them.

Understanding the importance of sleep is a fundamental goal, which also has wide-reaching practical significance for society. Despite attracting much research attention, there is still no consensus as to the origin and functional significance of sleep [39, 65]. Clinically-based studies have therefore taken the general approach of inferring the role of sleep and the mechanisms governing it by empirically studying the consequences of various disruptions to the normal sleep-wake schedule. Although such studies have limited utility in understanding the role of sleep and arousal on a deeper, mechanistic level, they nevertheless yield significant and applicable results. For example, the increasing trend in

modern society of submitting workers to increasing work loads raises concerns as to the health implications of such a practice [66, 67]. Indeed, general neglect of sleep and the increasing reliance on stimulants and depressants to maintain artificial sleep schedules present further potential health concerns [68]. Clinical sleep studies have helped to determine the importance of sleep for learning and memory [69, 70] and performance [12, 71]. In some professions, including the medical, military, and transport industries, around-the-clock workloads are required. Since fatigue-related accidents can prove fatal, clinical studies can help to improve safety and productivity in these workplaces [7].

While the utility of empirical, clinically-based studies is undeniable, there is great potential for theoretical sleep models to provide even more powerful predictions; as a means of guiding experimental work and interpreting clinical results more precisely, as well as yielding useful predictions in their own right. Sleep models are potentially able to predict and optimize sleep-wake schedules for any number of applications, including jet lag, shift work, and pharmaceutical treatments for sleep disorders. As well as providing general insights into the mechanisms behind sleep-related phenomenons, theoretical simulations may circumvent the need to expend both money and time to conduct a series of clinical studies. Progress in sleep modeling has relied on the results of both clinical and physiological experiments. In this chapter we distinguish between two broad classes of sleep models: phenomenological models that explain the results of experiments in terms of an empirically-motivated framework, and physiologically-based models that target the neuronal-level interactions from which behavioral information is subsequently inferred. These two distinct approaches are treated in turn in the following two sections.

1.2 Phenomenological Sleep Models

It is currently understood that three main drives control the dynamics between sleep and wake: a *homeostatic* 'sleep pressure', that builds during wake and is

relieved with sleep, a $\sim 24\,\mathrm{h}$ periodic *circadian* oscillation, which is entrained to the day-night cycle by photic input, and an *ultradian* rhythm, which controls the architecture of sleep, including transitions between rapid eye movement (REM) and non-rapid eye movement (NREM) sleep. The seminal *two-process* model of Borbély [56], combined the homeostatic and circadian drives into a phenomenological framework that was able to explain the timing of sleep and wake. Borbély proposed that a homeostatic *Process S*, restricted to lie between two circadian thresholds, grows during wake and falls during sleep, as depicted in Fig. 1.1. When Process S rises as high as the upper circadian threshold, sleep is triggered, and when it falls as low as the lower threshold, wake is triggered. Due to the shape of the Process S time series [which was inferred from the variation of EEG slow-wave activity (SWA) [72]] and the topology of the circadian thresholds, this structure gives rise to an oscillatory switch-like alternation between sleep and wake.

In a quantitative implementation of Borbély's qualitative model, Daan *et al.* [57] proposed that external influences affect the circadian thresholds. With suitable adjustments, the authors were able to reproduce a variety of sleep-wake-related phenomena, including internal desynchronization in the absence of external time cues, sleep fragmentation, simulation of fatigue during sleep deprivation, recovery from sleep deprivation, and shift work [57]. Other elaborations of the two-process model have since incorporated the ultradian rhythm [73] and sleep inertia, the latter yielding the so-called 'three-process' model [60, 61, 74]. Quantitative phenomenological sleep models proposed since largely build on the precedent established by the two-process model and its derivatives [58, 75]. However, whilst successful for the protocols they have been calibrated against [59], the predictive power of these models for more general regimens is limited [76].

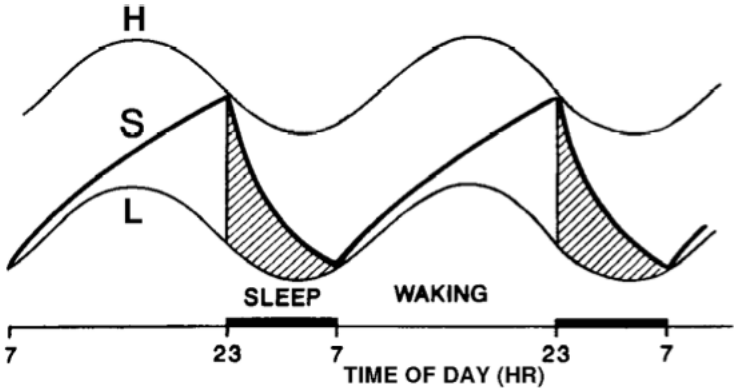

Figure 1.1: *Schematic of Borbély's two-process model [56], including the upper (H) and lower (L) circadian thresholds and the resulting time course of the homeostatic Process S. Figure adapted from [77].*

1.3 Physiologically-Based Sleep Modeling

In this section physiologically-based sleep modeling is summarized, including a brief overview of sleep-wake physiology and the main approaches to modeling it. Complete physiological details are not presented here, but can instead be found in the relevant later chapters.

In recent years, knowledge about the physiological interactions responsible for sleep-wake dynamics has become increasingly detailed. The basic dynamics between sleep and wake can be understood in terms of the interactions between the wake-active monoaminergic brainstem nuclei (MA) and the sleep-active ventrolateral preoptic area (VLPO) of the hypothalamus. Monoaminergic neurotransmitters inhibit the VLPO, and the VLPO inhibits the MA via GABAergic projections [50, 51, 78]. Thus, the activity of each group suppresses the activity of the other, reducing the subsequent inhibition onto itself, and thereby indirectly reinforcing its own activity [49]. This behavior results in extended periods of either sleep (activated VLPO and suppressed MA) or wake (activated MA and suppressed VLPO), with rapid transitions between the two states – much like a 'flip-flop' circuit [79, 80]. Sleep-wake dynamics are thus characterized by two distinct states, with rapid transitions between them

and minimal time spent in intermediate states. The discovery of this neurological 'flip-flop' circuit explains how rapid switch-like sleep-wake transitions can result from the slowly-varying circadian and homeostatic drives that govern them.

As the physiological basis for sleep-wake behavior has become clearer, sleep models have been proposed that target the physiology directly. This physiologically-based approach is fundamentally different to the phenomenological one; the neuronal interactions that underpin sleep-wake dynamics are modeled instead of the empirical dynamics themselves. A number of such models have been proposed [62–64], but they tend to incorporate large numbers of neuronal populations and drives, with many resulting free parameters. Without sufficient physiological and behavioral constraints, physiological models that include large neuronal networks to explain relatively simple behavior risk encountering the same disadvantages as phenomenological models – simply fitting to empirical trends whilst providing limited physiological insights.

The sleep model developed recently by Phillips and Robinson [1] focuses on the sleep-wake flip-flop described above. It models the mutual inhibition of the VLPO and MA nuclei and includes the circadian and homeostatic drives. The model makes several important simplifications: it groups the monoaminergic populations as a single entity, and does not include time varying acetylcholine-related, orexinergic, or cortical inputs. The parameters of the Phillips-Robinson model are fitted from a small number of experiments [1, 81], but it is able to predict the results of many. Thus far, the model has been able to predict optimal recovery protocols from sleep deprivation, sleep latency times, and has offered qualitative descriptions of pathologies including narcolepsy [1, 81]. In this thesis, the model is extended to treat the impact of short auditory tones during sleep in Chapter 2, the prediction of fatigue-related measures across a period of total sleep deprivation in Chapter 3, and the simulation of waking performance variation in Chapter 4.

A schematic of the Phillips-Robinson model that is used in Chapters 2 and

3 is illustrated in Fig. 1.2(a). An extended version of the model that includes the Orx group is shown in Fig. 1.2(b), and is introduced and characterized in Chapter 4. Both models use an established methodology in which the microscopic structures of neuronal populations are averaged over, yielding continuum descriptions relevant for dynamics on a larger scale than that of the individual neuron [82, 83]. This is appropriate here where sleep-wake dynamics, including transitions between states, occur on a much longer time scale than that of the neuronal interactions within and between nuclei. This physiologically-based approach has been successfully applied to the corticothalamic system previously, reproducing characteristics of the EEG, including spectral peaks during waking and sleeping states, evoked response potentials, measures of coherence and spatiotemporal structure, and generalized epilepsies and low-dimensional seizure dynamics [84–86]. The same approach has also been applied to the basal ganglia [87]. A wider modeling goal is to incorporate the individual models of different parts of the brain into a single 'working brain' model. By linking models of the cortex, thalamus, basal ganglia, hypothalamus and brainstem nuclei, a broader and more complete understanding of large-scale brain dynamics as a whole may be gained. A schematic of the 'first cut' of such a model is depicted in Fig. 1.3, and is the subject of ongoing work.

1.4 Open Questions

Now that a brief overview of the wider field, including the role of sleep modeling, has been presented, we focus on the research presented in this thesis. In this section, a number of outstanding tasks in the sleep research field are discussed as a means of setting the research of Chapters 2–4 in the wider context of the field.

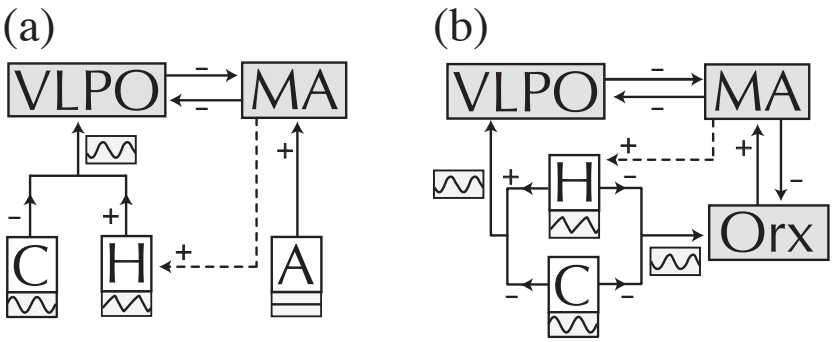

Figure 1.2: *Schematics of the sleep models used in this thesis. (a) The Phillips-Robinson model used in Chapters 2 and 3, which focuses on the mutual inhibition between the MA and the VLPO, and includes the circadian C and homeostatic H drives, as well as the time-averaged drive A to the MA. (b) An extension of the Phillips-Robinson sleep model that includes the orexin group of the lateral hypothalamic area (Orx). This model is introduced in Chapter 4 of this thesis. Excitatory (+) and inhibitory (−) interactions are shown with arrows. A schematic of the typical oscillatory time evolution of each drive is also displayed in a small rectangle.*

1.4.1 The Impact of External Stimuli

In addition to providing an accurate description of normal sleep-wake dynamics, a useful predictive sleep model must also include the impact of external influences, which are prevalent in reality. External stimuli may be in the form of pharmacological stimulants and sedatives, physical exercise and rest, the consumption of food and drink, temperature fluctuations, or auditory tones, for example. The impact of light has received a detailed treatment in phenomenological models of the circadian oscillator [28, 88, 89]. In addition, some empirically-based numerical models (e.g., [90]) take into account the intake of alcohol and caffeine, for example. However, despite the prevalence and significance of external stimuli, no studies have yet been able to rigorously treat the impact of general external stimuli on arousal-state dynamics. The most comprehensive progress in this direction to date has been made using quantitative implementations of the two-process model [57, 58]. However, being

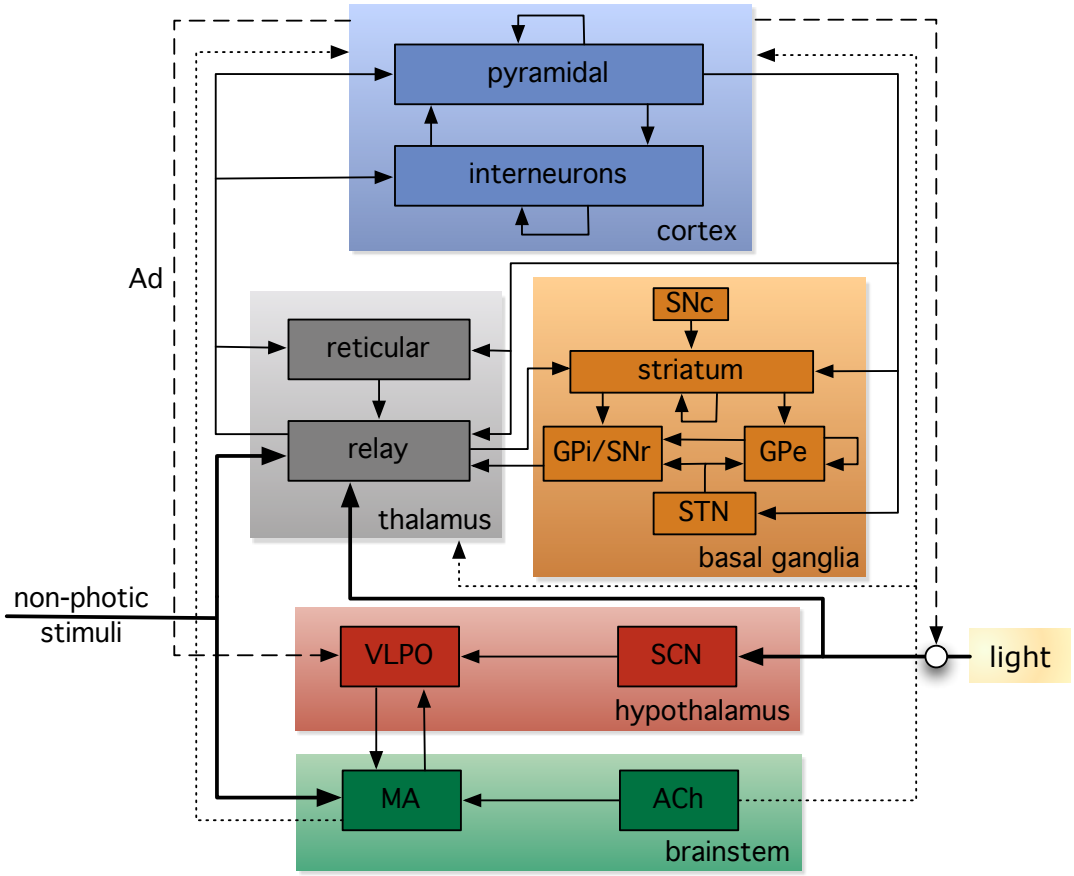

Figure 1.3: *Schematic of a 'first-cut working brain model'. As well as the brainstem and hypothalamic neuronal components that make up the Phillips-Robinson sleep model, this extended model includes the corticothalamic and basal ganglia neuronal populations and their interactions.*

phenomenological in nature, the process of modeling external stimuli is usually *ad hoc* and aimed at reproducing specific sets of experimental data.

In Chapter 2 of this thesis, we develop a framework for incorporating arbitrary external stimuli into the Phillips-Robinson model. External stimuli are modeled in terms of their neuronal mechanism whence the model quantitatively predicts the resulting time varying neuronal dynamics. Clinically measurable information can be extracted from the model's output, including arousal levels, sleep latencies, and sleep lengths, for example. A major advantage of this approach is that it elucidates the physiological mechanisms underpinning the behavioral changes caused by a given stimulus or combination of stimuli. In addition, all external stimuli can be represented on a unified scale, in terms of the relevant neuronal drives that they produce. In Chapter 2, the proposed system is used to treat impulsive sensory stimuli occurring during sleep, yielding dynamics that exhibit close agreement with clinical data obtained from the literature. The framework for modeling the impact of external stimuli developed in Chapter 2 of thesis is a general one and is expected to be used to model a variety of particularly sensory and pharmacological stimuli in future work.

1.4.2 Total Sleep Deprivation

As mentioned previously, clinical studies often focus upon the impact of sleep deprivation as a means of inferring the functional significance of sleep. Sleep deprivation research may be useful in guiding safer practices for night drivers, medical clinicians, and air traffic controllers, for example. The task of modeling total sleep deprivation comprehensively, including the dynamics of fatigue and performance, is therefore an important one. Within the two-process model, sleep deprivation is simulated by allowing Process S to rise above its upper circadian threshold (where sleep is usually triggered), as shown in Fig. 1.4. The difference between Process S and the upper threshold is taken to be a measure of 'fatigue' [57]. The model predicts a fatigue variation that includes an

oscillating (circadian) component and an increasing (homeostatic) component and is qualitatively consistent with the well-known clinical variation [91]. However, being phenomenological in nature, the physiological processes responsible for the fatigue variation are unclear. Furthermore, the mechanisms by which a subject is able remain awake and rise above the upper circadian threshold, which should trigger sleep, are not explained. Sleep deprivation has been modeled within the Phillips-Robinson model previously [81], dealing predominantly with the concept of 'sleep debt' and the prediction of optimum recovery protocols. In Chapter 3 we use aspects of the dynamical analysis of the model performed in Chapter 2, to justify a new, physiologically-based method for modeling sleep deprivation. An additional physiological drive, due to cortical or orexinergic afferents, is required to maintain wakefulness at high sleep pressure. We hypothesize a connection between the need to exert this drive and fatigue-related measures; e.g., via distraction from normal cognitive performance. Indeed, the model exhibits quantitative agreement with subjective fatigue-related measures calculated in a number of clinical sleep deprivation studies. The work presented in Chapter 3 is the first physiologically-justified simulation of fatigue and performance during sleep deprivation.

1.4.3 The Orexin Group: Narcolepsy and Performance

The orexin A and orexin B neurotransmitters (also termed hypocretin 1 and 2) were simultaneously discovered by Sakurai *et al.* [92] and de Lecea *et al.* [93] in 1998. Produced by neurons in the lateral hypothalamic area (LHA), they have since been implicated in numerous neurological processes, including a key role in the regulation of sleep and wakefulness [51, 94]. However, the Orx group was not explicitly included in the original Phillips-Robinson sleep model [1, 81]; rather, its dynamics were effectively averaged over, contributing a constant drive to the MA. Loss of orexin is thought to be the cause of the neurodegenerative pathology narcolepsy, which is characterized by a weakening

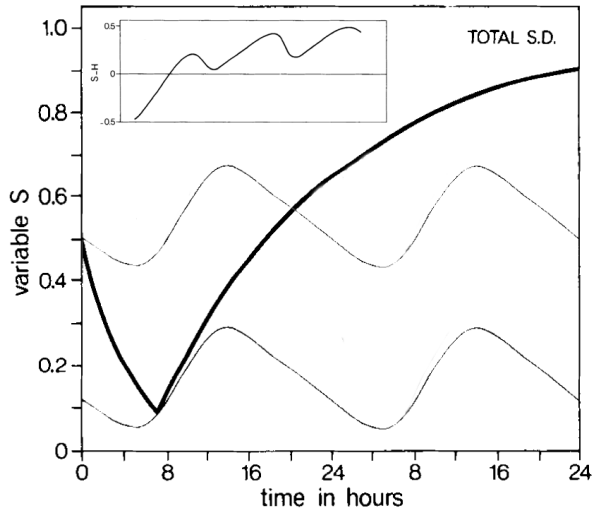

Figure 1.4: *A simulation of sleep deprivation using an implementation of the two-process model [57]. Process S is allowed to rise above the maximum circadian threshold, and the difference between variable S and the upper circadian threshold gives an indication of subjective fatigue. The predicted fatigue variation is shown inset, yielding the same qualitative variation measured in clinical sleep deprivation studies. This figure was adapted from [57].*

of the usual sleep-wake distinction [95–99]. Narcoleptics experience disturbed sleep, drowsiness, and uncontrollable daytime napping [100]. In Chapter 4, the orexin group is included explicitly as a neuronal population, as shown in Fig. 1.2(b). The relevant neuronal interactions and the circadian and homeostatic inputs are modeled according to the known physiology. We show that decreasing the drive to the MA group from Orx produces changes in the model's equilibrium structure that are qualitatively consistent with the clinical symptoms of narcolepsy. Furthermore, the Orx group is linked to sleep inertia [101, 102], circadian input to the Orx produces a postlunch dip in arousal [103], and the arousal variation resulting from combined circadian and homeostatic input to Orx is found to agree with existing experimental data [104].

Chapter 2

Modeling the Impact of Impulsive Stimuli on Sleep-Wake Dynamics

Abstract

A neuronal population model of the sleep-wake switch is extended to incorporate impulsive external stimuli. The model includes the mutual inhibition of the sleep-active neurons in the hypothalamic ventrolateral preoptic area (VLPO) and the wake-active monoaminergic brainstem populations (MA), as well as circadian and homeostatic drives. Arbitrary stimuli are described in terms of their relative effects on the VLPO and MA nuclei and represent perturbations on the normal sleep-wake dynamics. By separating the model's intrinsic time scales, an analytic characterization of the dynamics in a reduced model space is developed. Using this representation, the model's response to stimuli is discussed, including the latency to return to wake or sleep, or to elicit a transition between the two states. Since sensory stimuli are known to excite the MA, we correspondingly investigate the model's response to auditory tones during sleep, as in clinical sleep fragmentation studies. The arousal threshold is found

to vary approximately linearly with the model's total sleep drive, which includes circadian and homeostatic components. This relationship is used to reproduce the clinically observed variation of the arousal threshold across the night, which rises to a maximum near the middle of the night and decreases thereafter. In a further application of the model, time-of-night arousal threshold and body temperature variations in an experimental sleep fragmentation study are replicated. It is proposed that the shift of the extremums of these curves to a greater magnitude later in the night is due to the homeostatic impact of the frequent nocturnal disturbances. Drawing on the underlying neuronal interactions, the model presented here predicts arousal state responses to external stimuli. This methodology is fundamentally different to previous approaches that model the clinical data within a phenomenological framework. As a result, a broader understanding of how impulsive external stimuli modulate arousal is gained.

2.1 Introduction

It is currently understood that three main drives regulate sleep-wake dynamics: a *homeostatic* 'sleep pressure', that builds during wake and is relieved with sleep, a $\sim 24\,\mathrm{h}$ periodic *circadian* oscillation, which is entrained to the day-night cycle by photic input, and an *ultradian* rhythm, which controls the architecture of sleep, including transitions between rapid eye movement (REM) and non-rapid eye movement (NREM) sleep. Sleep-wake modeling derives much from the two-process model of Borbély [56] which, motivated by the variation of EEG slow-wave activity (SWA) [72], combined the homeostatic and circadian drives into a conceptual framework that was able to explain the timing of sleep and wake. Quantitative implementations of the two-process model have since been able to reproduce a wide variety of sleep-wake phenomena, including subjective fatigue during sleep deprivation, internal desynchronization, fragmented sleep during continuous bedrest, and the sleep durations of shift workers [57], as well as ultradian variations in SWA [73]. Quantitative phenomenological sleep

models proposed since build on the precedent established by the two-process model [58, 75]. However, whilst successful for the protocols they have been calibrated against [59], the predictive power of these models for general regimens is limited [76].

By incorporating knowledge of the neuronal interactions that give rise to sleep-wake dynamics, physiologically-based sleep models can be developed that provide insights into the neurological processes that underpin their behavioral predictions. Sleep-wake dynamics are characterized by rapid transitions between two distinct states: sleep and wake, and result from the mutual inhibition between sleep-active neurons in the ventrolateral preoptic area (VLPO) of the hypothalamus and wake-active monoaminergic neuronal populations (MA) in the brainstem [49]. The activity of each group suppresses the activity of the other, which reduces the subsequent inhibition on itself, i.e., the firing of each group indirectly reinforces its own firing. This behavior results in extended periods of either sleep (activated VLPO and suppressed MA) or wake (activated MA and suppressed VLPO), with rapid transitions between the two states dictated by the slowly-varying circadian and homeostatic sleep drives; much like a 'flip-flop' circuit [79]. The circadian signal is the result of molecular-level oscillations in the suprachiasmatic nucleus (SCN) [50], while the homeostatic sleep drive is believed to result from the accumulation of sleep-promoting metabolic byproducts [105]. Physiologically-based sleep models have recently been constructed that incorporate these neurological drives and interactions. Their parameters are in principle physiologically measurable and dynamical restrictions on model parameters can be used to infer physiological information. A number of such models have been proposed [62–64], but they tend to incorporate large numbers of neuronal populations and drives, with many resulting free parameters. The Phillips-Robinson sleep model [1], used in this chapter, set a more modest target of modeling the well-substantiated physiology of the sleep-wake switch. Its parameters are fitted from a small number of experiments yet it is able to predict the results of many. Thus far, the model has been able to predict

optimal recovery protocols from sleep deprivation, sleep latency times, and has offered qualitative descriptions of pathologies including narcolepsy [1, 81].

External stimuli that disturb the normal sleep-wake cycle are prevalent in reality and it is therefore important that they are thoroughly understood. Such stimuli may promote arousal in the form of stimulants such as caffeine and sensory reactions to bright light or loud noise, or promote sleep in the form of inactivity, dim light, or sedative drugs including antihistamines. Despite the success of quantitative phenomenological models in reproducing a wide variety of clinical observations, the effects of general external stimuli have not yet received a detailed treatment. Indeed, the incorporation of external stimuli into phenomenological models poses a particular challenge because a physiological foundation is lacking. In contrast, as we will demonstrate, knowledge of the mechanistic pathway of an external stimulus provides a natural avenue for its inclusion into a physiologically-based model. The major benefit of this approach is its ability to encompass a wide variety of stimuli on a common scale, in terms of their impact on the relevant arousal-producing nuclei. Ultimately, the behavioral outcome of a given stimulus can be understood in terms of its underlying neurological mechanism.

Our aims in this chapter are threefold: (i) to present a rigorous investigation of the general dynamics of the Phillips-Robinson model, (ii) to illustrate its correspondence with several specific clinical measures, and (iii) to lay the groundwork for future, more clinically oriented investigations. In Sec. 2.2, we summarize the relevant physiology and introduce the Phillips-Robinson model. A theoretical characterization of the model is undertaken in Sec. 2.3, including a separation of model time scales that allows an equilibrium and linear stability analysis in a reduced two-dimensional model space. In Sec. 2.4, we consider the impact of general impulsive stimuli characterized by drives to the sleep-active VLPO and wake-active MA populations, explaining the results in terms of the dynamical features of the model. In Sec. 2.5, we consider arousing impulses during sleep, replicating the time-of-night arousal threshold curves observed

clinically. A subsequent calibration from the intensity of an auditory stimulus to the mean increase in MA cell-body potential required to provoke an arousal allows us to reproduce the arousal threshold and body temperature variation in another sleep fragmentation study.

2.2 Physiology and Modeling

We begin with a brief summary of the relevant sleep-wake physiology and an overview of the Phillips-Robinson model [1].

2.2.1 Physiology

The overall arousal state of the brain is controlled by a series of brainstem nuclei, collectively termed the ascending arousal system (AAS), which diffusely project neuromodulators to the cerebrum [50, 106, 107]. Based on common effects and temporal patterns of activity, brainstem AAS nuclei can be broadly classified as monoaminergic (MA) or acetylcholine-related (ACh). The MA group includes nuclei that use monoaminergic neurotransmitters: the histaminergic tuberomammillary nucleus (TMN), norepinephrinergic locus coeruleus (LC), serotoninergic dorsal raphé nucleus (DR), and dopaminergic ventral tegmental area (VTA) [31, 107, 108]. The ACh group includes nuclei that express acetylcholine, including the pedunculopontine (PPT) and laterodorsal (LDT) tegmental nuclei in the mesopontine tegmentum [109, 110]. The orexin population of the lateral hypothalamus excites MA and ACh neuronal populations during wake, thereby acting to stabilize the waking state [111, 112].

Circadian and homeostatic drives are integrated in the ventrolateral preoptic area (VLPO) of the hypothalamus, affecting the AAS via inhibitory GABAergic projections from there [50, 51, 78]. The 24 h periodic circadian signal originates in the suprachiasmatic nucleus (SCN) and maintains the entrainment of

the sleep-wake cycle to the light cycle through projections to the VLPO, primarily via the dorsomedial nucleus of the hypothalamus (DMH) [50, 51, 113]. The homeostatic drive increases with time spent awake, which is believed to be due to a net build up of the somnogenic metabolic byproduct adenosine in the basal forebrain [107, 114, 115], disinhibiting the VLPO [50, 51]. During sleep, metabolic rates are low and adenosine is cleared faster than it is produced [115–117]. Mutual inhibition between the MA group and the VLPO gives rise to the sleep-wake 'flip-flop', with each group disinhibiting its own activity [49, 79]. During wake, the MA group is active and the VLPO is suppressed, while the converse occurs during sleep.

2.2.2 The Phillips-Robinson Model

Phillips and Robinson incorporated the above physiology into a neuronal population model [1], considering the average properties of large populations of neurons and their interactions, as has been done previously for the corticothalamic system [82–84]. Each population $j = m, v$, where m represents the MA and v represents the VLPO, has a mean cell-body potential $V_j(t)$ relative to resting and a mean firing rate $Q_j(t)$. The relationship of Q_j to V_j is approximated by a sigmoid [82], with

$$Q_j = S(V_j) = \frac{Q_{\max}}{1 + \exp[-(V_j - \theta)/\sigma']}, \tag{2.1}$$

where $Q_{\max}$ is the maximum possible firing rate, θ is the mean firing threshold relative to resting, and $\sigma'\pi/\sqrt{3}$ is its standard deviation [84]. Due to the small spatial extent of the relevant nuclei, we assume spatial homogeneity of each population and neglect propagation delays.

Neuronal dynamics are represented by

$$\tau_v \dot{V}_v + V_v = \nu_{vm} Q_m + D_v, \tag{2.2}$$

$$\tau_m \dot{V}_m + V_m = \nu_{mv} Q_v + D_m, \tag{2.3}$$

where the ν_{jk} weight the input from population k to j, τ_j is the decay time for the neuromodulator expressed by group j, and D_j represents the external drive to population j. In the presence of external stimuli, the drive terms can be written in the form

$$D_v = D_v^0 + \Delta D_v, \tag{2.4}$$

$$D_m = D_m^0 + \Delta D_m, \tag{2.5}$$

where normal sleep-wake dynamics are governed by the drives D_j^0, and the ΔD_j represent perturbations. It is convenient to represent the drives in vector form so that the sum of the unperturbed drive $\mathbf{D}^0 = (D_v^0, D_m^0)$ and the perturbation $\Delta\mathbf{D} = (\Delta D_v, \Delta D_m)$ gives the total drive $\mathbf{D} = (D_v, D_m) = \mathbf{D}^0 + \Delta\mathbf{D}$. All types of perturbative external stimuli, including sensory and pharmaceutical effects, are encapsulated in $\Delta\mathbf{D}$.

Nominal input to the VLPO

$$D_v^0 = \nu_{vc} C + \nu_{vh} H, \tag{2.6}$$

includes circadian (C) and homeostatic (H) components. The 24 h periodic circadian drive is taken to be well-entrained to the daily fluctuation in light intensity and is approximated as a sinusoidal function of time

$$C(t) = \sin \omega t + c_0, \tag{2.7}$$

where $\omega = (2\pi/24)\,\mathrm{h}^{-1}$ and c_0 is a constant offset. An oscillation amplitude of unity is used without loss of generality – the actual amplitude is absorbed into ν_{vc}.

The homeostatic sleep drive is represented by the somnogen level H, which represents the concentration of extracellular adenosine in the basal forebrain. The somnogen clearance rate is assumed to be proportional to its concentration, with production approximated as a linear function of Q_m because MA activity

is well correlated with arousal [118] and, presumably, metabolism. Assuming that $Q_m = 0$ results in negligible net production yields

$$\chi \dot{H} + H = \mu Q_m, \tag{2.8}$$

where χ is the characteristic somnogen clearance time and μ is a constant. The value of H grows during wake to a maximum at sleep onset, and decreases during sleep to a minimum at the end of a sleep period.

The unperturbed drive D_m^0 to the MA represents input from groups including acetylcholine and orexin. The ACh group is influenced by the homeostatic variation of adenosine concentration [105, 119], and its interaction with the MA group may produce the $\sim 90\,\text{min}$ ultradian oscillation [50]. Orexinergic activity also varies, with factors including emotion, energy homeostasis, and reward systems [112]. However, in the current form of the model, the time-varying input from these groups is not explicitly considered, instead being averaged to a constant, intermediate level of activity $D_m^0 = A$. This approximation allows us to focus on the 'flip-flop' dynamics between sleep and wake. A dynamic drive D_m^0 would modulate the arousal state within sleep and wake, and will be explored in a future version of the model.

The above formulation is represented schematically in Fig. 2.1. Model parameters have been constrained elsewhere by both dynamics and physiology to produce realistic sleep-wake behavior [1, 81], with current values shown in Tab. 4.1. When external perturbations are excluded ($\boldsymbol{\Delta}\mathbf{D} = 0$) we obtain 'normal' model output, shown as a time series in Fig. 2.2. The arousal state alternates between periods of wake with high V_m, low V_v, and increasing H, and periods of sleep with high V_v, low V_m, and decreasing H. Plotting V_m or V_v against the oscillatory D_v, as shown in Fig. 2.3, reveals hysteresis – the mutual inhibition between the VLPO and MA groups gives rise to sleep and wake branches at high and low D_v, respectively, and an intermediate bistable region in which both states exist simultaneously. As D_v oscillates with a 24 h period,

Table 2.1: *Nominal model parameter values obtained from [81].*

Param.	Value	Param.	Value	Param.	Value
$Q_{\max}$	$100\,\mathrm{s}^{-1}$	ν_{vm}	$-2.1\,\mathrm{mV\,s}$	μ	$4.4\,\mathrm{nM\,s}$
θ	$10\,\mathrm{mV}$	ν_{mv}	$-1.8\,\mathrm{mV\,s}$	χ	$45\,\mathrm{h}$
σ'	$3\,\mathrm{mV}$	ν_{vh}	$1\,\mathrm{mV\,nM}^{-1}$	τ_v, τ_m	$10\,\mathrm{s}$
A	$1.3\,\mathrm{mV}$	ν_{vc}	$-2.9\,\mathrm{mV}$	c_0	4.5

the arousal state evolves around the hysteresis loop, alternating between sleep and wake accordingly.

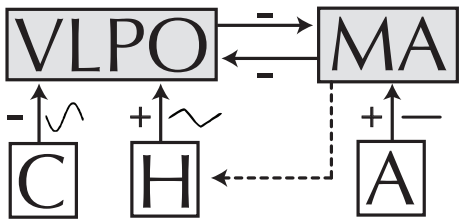

Figure 2.1: *Schematic of the Phillips-Robinson model of the sleep-wake switch. The mutually inhibitory VLPO and MA populations form the core of the model, which also includes circadian (C) and homeostatic (H) drives to the VLPO and the constant drive A to the MA. Excitatory (+) and inhibitory (−) interactions are shown with arrows and arousal state feedback from the MA to H is shown dashed. A schematic of the typical time evolution of each drive is also displayed [c.f., Figs 2.2(c) and (d)].*

2.3 Analysis of the Model

In this section, different representations of the model dynamics are explored. Following a description of the reduced manifold in V_v–V_m–D_v space, a linear stability analysis in V_v–V_m space is undertaken that exploits a separation of the model's intrinsic time scales. The analysis in this section provides a convenient

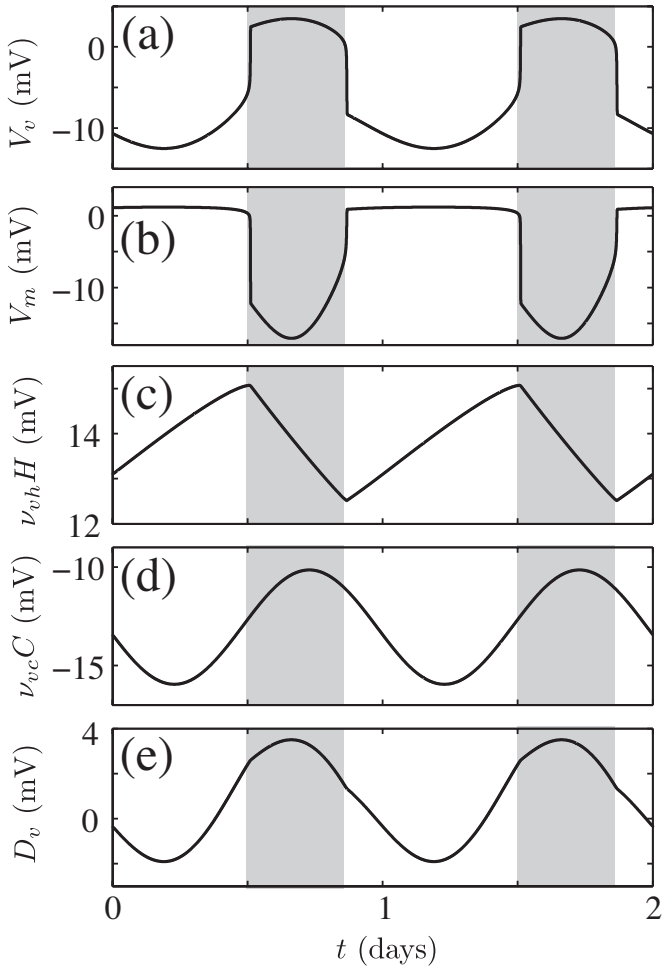

Figure 2.2: *Normal, unperturbed output from the Phillips-Robinson model. Time series are shown for (a) V_v [Eq. (2.2)], (b) V_m [Eq. (2.3)], (c) $\nu_{vh}H$ [c.f. Eq. (2.8)], (d) $\nu_{vc}C$ [c.f. Eq. (2.7)], and (e) $D_v = D_v^0 = \nu_{vc}C + \nu_{vh}H$ [Eq. (2.6)]. Sleep periods are shaded.*

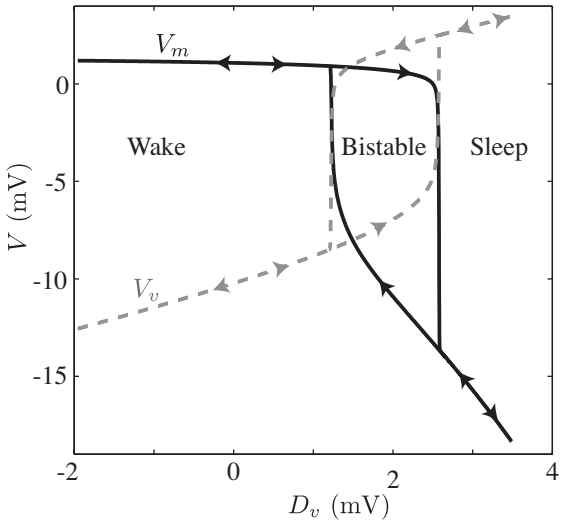

Figure 2.3: *Hysteresis in the Phillips-Robinson model. The mean cell-body potentials V_m (solid black line) and V_v (dashed gray line) are plotted against D_v, showing hysteresis. Wake (low D_v), sleep (high D_v), and bistable (intermediate) regions are labeled. The arousal state alternates between sleep and wake as the 24* h *periodic sleep drive D_v oscillates with time.*

framework with which to study the model's response to impulsive external stimuli, which is covered in Secs 2.4 and 2.5.

2.3.1 A Separation of Time Scales

In the absence of external stimuli ($\Delta\mathbf{D} = 0$), the Phillips-Robinson model is formulated in terms of two distinct time scales: that of the sleep-wake transitions ($\sim 10\,\text{min}$) governed by the time constants τ_m and τ_v, and that of the drive D_v ($\sim 1\,\text{day}$), governed by the time constants ω^{-1} and χ. Since τ_m, $\tau_v \ll \omega^{-1}$, χ, it follows that V_v [Eq. (2.2)] and V_m [Eq. (2.3)] evolve on a much faster time scale than the circadian [Eq. (2.7)] and homeostatic [Eq. (2.8)] drives. On short time scales we can therefore approximate $\dot{D}_v \approx 0$. In this regime, D_v can be treated as a control parameter and the system simplifies to the *layer problem* of Fenichel theory [120], which is characterized by rapid attraction onto the *reduced manifold* defined by $\dot{V}_v = \dot{V}_m = 0$. On longer time

scales we have the *reduced problem*: attraction onto the reduced manifold is considered complete and evolution through V_v–V_m–D_v space is along the manifold. The reduced manifold consists of stable sleep and wake branches joined by an unstable branch, as shown in Fig. 2.4. Projections of the reduced manifold onto reduced two-dimensional subspaces yields bifurcation curves showing hysteresis for V_m and V_v as functions of D_v, and a monotonic curve in V_v–V_m space.

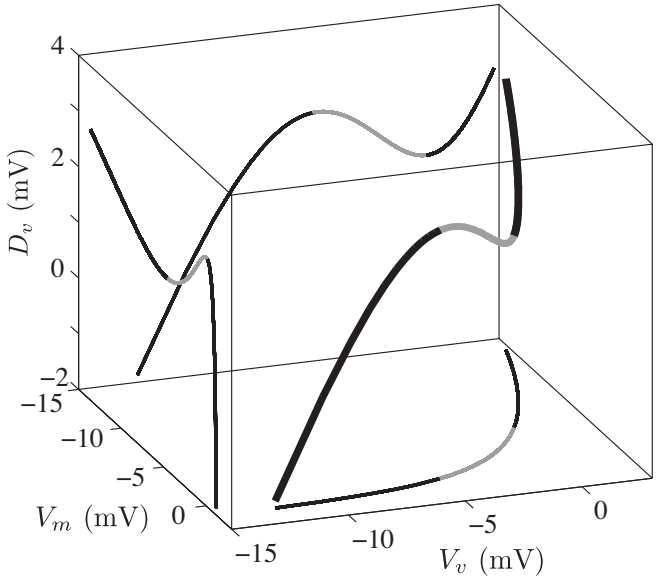

Figure 2.4: *The reduced manifold in V_v–V_m–D_v space. Stable sleep (high V_v, low V_m) and wake (low V_v, high V_m) branches (black lines) are connected by the intermediate unstable branch (gray line). Projections of the manifold onto the two-dimensional subspaces are also plotted.*

2.3.2 A Reduction to V_v–V_m Space

Treating D_v as a control parameter, we are motivated to explore slices of constant D_v in V_v–V_m space. Model dynamics in this space can be understood in

terms of the nullclines, $\dot{V}_v = 0$:

$$V_v = \nu_{vm} S(V_m) + D_v, \tag{2.9}$$

and $\dot{V}_m = 0$:

$$V_m = \nu_{mv} S(V_v) + D_m. \tag{2.10}$$

The intersection of the nullclines defines an equilibrium point (V_v^*, V_m^*), which can be written implicitly in terms of V_v^* as

$$\tau_v \dot{V}_v = -V_v^* + \nu_{vm} S\left[\nu_{mv} S(V_v^*) + D_m\right] + D_v = 0, \tag{2.11}$$

or in terms of V_m^* as

$$\tau_m \dot{V}_m = -V_m^* + \nu_{mv} S\left[\nu_{vm} S(V_m^*) + D_v\right] + D_m = 0. \tag{2.12}$$

Movement through the V_v–V_m plane is determined by the velocity vector field

$$\dot{\mathbf{V}} = (\dot{V}_v, \dot{V}_m), \tag{2.13}$$

which has magnitude $\dot{V} = |\dot{\mathbf{V}}| = (V_v^2 + V_m^2)^{1/2}$.

The drives are slowly-varying and are treated as control parameters, whence $\dot{V}_v$ and $\dot{V}_m$ are functions of V_v and V_m only. The Jacobian matrix $\mathbf{J}$ of the resulting two-dimensional system evaluated at an equilibrium (V_v^*, V_m^*) is

$$\mathbf{J}|_{(V_v^*, V_m^*)} = \left.\begin{pmatrix} \partial\dot{V}_v/\partial V_v & \partial\dot{V}_v/\partial V_m \\ \partial\dot{V}_m/\partial V_v & \partial\dot{V}_m/\partial V_m \end{pmatrix}\right|_{(V_v^*, V_m^*)} \tag{2.14}$$

$$= \begin{pmatrix} -\tau_v^{-1} & \frac{\nu_{vm}}{\tau_v} S'(V_m^*) \\ \frac{\nu_{mv}}{\tau_m} S'(V_v^*) & -\tau_m^{-1} \end{pmatrix}, \tag{2.15}$$

where

$$S'(x) = \frac{d}{dx}S(x) = \frac{\exp\left(-\frac{x-\theta}{\sigma'}\right)}{Q_{\max}}S^2(x), \tag{2.16}$$

which is positive definite. The trace T and determinant Δ of the Jacobian are given by

$$T \equiv \mathrm{Tr}[\mathbf{J}] = -(\tau_m^{-1} + \tau_v^{-1}), \tag{2.17}$$

$$\Delta \equiv \det[\mathbf{J}] = \tau_m^{-1}\tau_v^{-1}\left[1 - \nu_{mv}\nu_{vm}S'(V_v^*)S'(V_m^*)\right], \tag{2.18}$$

and we have

$$T^2 - 4\Delta = (\tau_m^{-1} - \tau_v^{-1})^2 + 4\tau_m^{-1}\tau_v^{-1}\nu_{mv}\nu_{vm}S'(V_v^*)S'(V_m^*). \tag{2.19}$$

Since $T < 0$ and $T^2 - 4\Delta > 0$, the fixed points are either stable nodes ($\Delta > 0$) or saddle points ($\Delta < 0$) [121]. The eigenvalues $\lambda_\pm = \left(T \pm \sqrt{T^2 - 4\Delta}\right)/2$ of the Jacobian are

$$\lambda_\pm = \frac{1}{2}\left[-(\tau_m^{-1} + \tau_v^{-1}) \pm \sqrt{(\tau_m^{-1} - \tau_v^{-1})^2 + 4\tau_m^{-1}\tau_v^{-1}\nu_{mv}\nu_{vm}S'(V_v^*)S'(V_m^*)}\right]. \tag{2.20}$$

For each equilibrium, there exist invariant linearized subspaces to which the corresponding invariant manifolds of the nonlinear system are tangent, according to the Stable Manifold Theorem [122, 123]. We proceed by solving the eigenvalue problem $(\mathbf{J} - \lambda\mathbf{I})\mathbf{v} = 0$, where $\mathbf{I}$ is the $2\,\mathrm{x}\,2$ identity matrix and the eigenvector $\mathbf{v}$ is the column vector (v_1, v_2):

$$\begin{pmatrix} -\tau_m^{-1} - \lambda_\pm & \frac{\nu_{mv}}{\tau_m}S'(V_v^*) \\ \frac{\nu_{vm}}{\tau_v}S'(V_m^*) & -\tau_v^{-1} - \lambda_\pm \end{pmatrix}\mathbf{v} = \mathbf{0}. \tag{2.21}$$

Expanding the first row of this matrix equation yields

$$\frac{v_2}{v_1} = \frac{\tau_m(\tau_m^{-1} + \lambda_\pm)}{\nu_{mv}S'(V_v^*)}, \tag{2.22}$$

the sign of which is opposite to that of $\tau_m^{-1}+\lambda_\pm$ because $\nu_{mv} < 0$ and $S'(V_v^*), \tau_m > 0$. From Eq. (2.20),

$$\tau_m^{-1} + \lambda_\pm = \frac{1}{2}\left[(\tau_m^{-1} - \tau_v^{-1}) \pm \sqrt{(\tau_m^{-1} - \tau_v^{-1})^2 + 4\tau_m^{-1}\tau_v^{-1}\nu_{mv}\nu_{vm}S'(V_v^*)S'(V_m^*)}\right]. \tag{2.23}$$

The magnitude of the square root term in Eq. (2.23) is greater than $|\tau_m^{-1} - \tau_v^{-1}|$, ensuring that $\tau_m^{-1} + \lambda_+ > 0$ and $\tau_m^{-1} + \lambda_- < 0$. Therefore, from Eq. (2.22), the eigenvector $\mathbf{v}_+$ (corresponding to λ_+) has $v_2/v_1 < 0$, and $\mathbf{v}_-$ (corresponding to λ_-) has $v_2/v_1 > 0$. Also, because $T < 0$ implies that $|\lambda_-| > |\lambda_+|$, trajectories evolve rapidly in the $\mathbf{v}_-$ eigendirection (with a positive gradient in the V_v–V_m plane) and approach fixed points along the weaker $\mathbf{v}_+$ eigendirection (with a negative gradient in the V_v–V_m plane). We refer to the fast and slow invariant manifolds of the nonlinear system as W^- and W^+, respectively.

In the current form of the model, τ_m is set equal to τ_v for simplicity (for $\tau_m \neq \tau_v$, the population with the smaller time constant slaves to the dynamics of the population with the larger time constant [1]). Writing $\tau \equiv \tau_v = \tau_m$, the eigenvalues in this case are given by

$$\lambda_\pm = \tau^{-1}\left[-1 \pm \sqrt{S'(V_v^*)S'(V_m^*)}\right], \tag{2.24}$$

and the ratio v_2/v_1 in the two eigendirections are negatives of each other:

$$\frac{v_2}{v_1} = \pm\sqrt{\frac{\nu_{vm}S'(V_v^*)}{\nu_{mv}S'(V_m^*)}}. \tag{2.25}$$

The eigenvalues $\lambda_\pm$ are plotted as a function of D_v in Fig. 2.5. Consistent with the hysteresis picture shown in Fig. 2.3, we have a pair of negative eigenvalues at low D_v corresponding to the stable 'wake node', and at high D_v corresponding to the stable 'sleep node', with a bistable region in which both stable nodes and a saddle point exist simultaneously. For normal parameters, there exist two saddle-node bifurcations that define the extent of the bistable

region, associated with the annihilation of the sleep and wake nodes, respectively. Bifurcation points occur at an equilibrium: $\dot{V}_m(V_m) = 0$ [Eq. (2.12)] when $d/dV_m[\dot{V}_m(V_m)] = 0$ [121]. Combining these conditions, we find that bifurcation points are solutions of

$$S'\left[S^{-1}\left(\frac{V_m - D_m}{\nu_{mv}}\right)\right] S'(V_m) - \nu_{mv}^{-1}\nu_{vm}^{-1} = 0, \tag{2.26}$$

for V_m, where the inverse sigmoid $S^{-1}(x)$ is defined over $0 < x < Q_{\max}$ by $S^{-1}(x) = -\sigma \ln(Q_{\max}/x - 1) + \theta$. The V_v and D_v values corresponding to a bifurcation point can henceforth be determined from Eqs (2.10) and (2.12), respectively. For the nominal model parameters used in this chapter, the bistable region extends from $D_v = 1.45\,\mathrm{mV}$ (annihilation of the sleep node) to $2.46\,\mathrm{mV}$ (annihilation of the wake node). Note that the hysteresis loop attained by integrating the model equations (shown in Fig. 2.3) is wider than the theoretical bifurcation curve [shown in Fig. 2.6(a)] because the nonzero time constants τ_v and τ_m cause the system to lag behind the bifurcation curve.

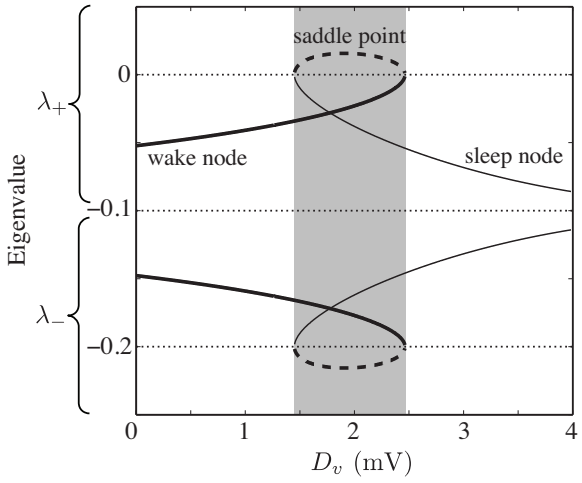

Figure 2.5: *Eigenvalues $\lambda_\pm$ of the Jacobian as a function of the control parameter D_v at a saddle point (dashed), wake node (thick), and sleep node (solid), as obtained from Eq. (2.24). The bistable region is shaded and the lines $\lambda = -\tau^{-1} = -0.1$, $\lambda = 0$, and $\lambda = -0.2$ are dotted.*

2.3.3 Nullcline Dynamics

Dynamics in V_v–V_m space corresponding to the above analysis can be interpreted in terms of the time evolution of the nullclines. The drive D_v translates the $\dot{V}_v = 0$ nullcline [Eq. (2.9)] horizontally and the drive D_m translates the $\dot{V}_m = 0$ nullcline [Eq. (2.10)] vertically. Taking $\Delta\mathbf{D} = 0$, the drive $D_m = D_m^0 = A$ to the MA is constant, and the drive $D_v = D_v^0$ to the VLPO – and hence the position of the V_v nullcline – is oscillatory. Normal dynamics therefore result from the 24 h periodic oscillation of the V_v nullcline relative to the stationary V_m nullcline. The correspondence between the hysteresis and nullcline representations of the model is illustrated in Fig. 2.6. These two-dimensional representations can be obtained from the reduced manifold in V_v–V_m–D_v space, shown in Fig. 2.4, by taking a projection onto the D_v–V_m plane [Fig. 2.6(a)], or slices through constant D_v [Fig. 2.6(b)-(d)]. At low and high D_v, the nullclines intersect at a single point, representing the stable wake and sleep nodes, respectively. At intermediate D_v, corresponding to the bistable region of the hysteresis loop, the nullclines have three points of intersection: two stable nodes and one saddle point. The invariant manifolds plotted in Fig. 2.6 are obtained by following the flow $\dot{\mathbf{V}}$ after applying small perturbations in the directions given by Eq. (2.25). The W^+ manifolds from the two nodes and the saddle point connect with one another in the bistable region, with the stable invariant manifold W^- of the saddle point, shown dot-dashed in Fig. 2.6(c), forming a separatrix between *sleep* and *wake basins* in V_v–V_m space. A trajectory with an initial condition in the sleep or wake basin will attract onto the sleep or wake node, respectively. These characteristic topological features of V_v–V_m space will facilitate an understanding of the model's response to impulsive external stimuli in Sec. 2.4.

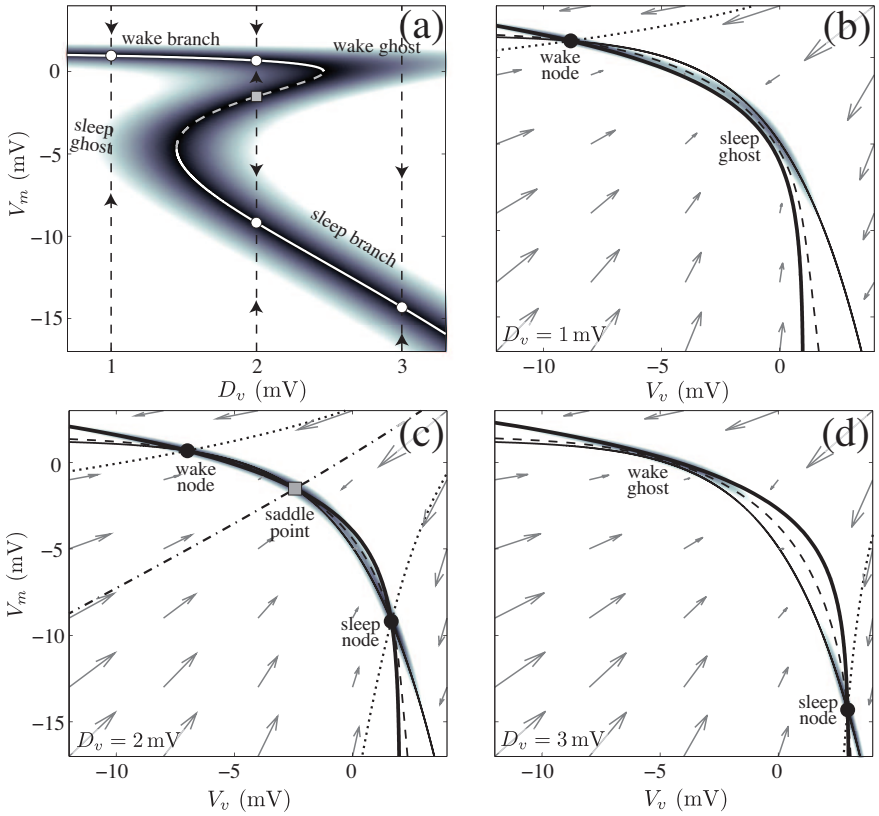

Figure 2.6: *Correspondence between (a) the D_v–V_m hysteresis representation and (b)–(d) the V_v–V_m nullcline representation of the model. (a) Bifurcation diagram for V_m against the control parameter D_v, showing hysteresis. Arrows indicate the direction of $\dot{V}_m$ for $D_v = 1, 2, 3$ mV. Regions of low $\dot{V}$ have been shaded, from $\dot{V} = 0$ (black) to $\dot{V} > 0.05\,\mathrm{mV\,s^{-1}}$ (white), where the minimum $\dot{V}$ (across variation in V_v) has been collapsed onto this picture. (b)–(d) V_v–V_m plots showing the V_v nullcline [Eq. (2.9)] (thick solid line), V_m nullcline [Eq. (2.10)] (thin solid line), stable nodes (circles), saddle points (squares), the W^+ manifold (dashed), the W^- manifold of stable nodes (dotted), the separatrix formed by the stable invariant manifold W^- of the saddle point (dot-dashed), the velocity vector field $\dot{\mathbf{V}}$ [Eq. (2.13)] (arrows), and regions over which $\dot{V} < 0.1\,\mathrm{mV\,s^{-1}}$ (shading) for (b) $D_v = 1\,\mathrm{mV}$, a stable wake node, (c) $D_v = 2\,\mathrm{mV}$, in the bistable region, and (d) $D_v = 3\,\mathrm{mV}$, a stable sleep node. Near-stable wake and sleep ghosts (c.f., Sec. 2.3.4) are also labeled.*

2.3.4 Ghosts

Following the annihilation of the wake and sleep nodes due to saddle-node bifurcations, regions of near-stability are retained, in the form of low $\dot{V}$. This is a general property of the saddle-node bifurcation – the low velocity region is termed a saddle-node remnant, or *ghost* [121]. The *sleep* and *wake ghosts* of our model are illustrated in Figs 2.6(b) and (d), respectively, and both ghosts are labeled in the hysteresis picture of Fig. 2.6(a). As a consequence of the low $\dot{V}$ region, trajectories evolve slowly through a bottleneck in the vicinity of the ghosts [121]. In our model, this behavior can be interpreted as brief awakenings during sleep (lingering in the wake ghost), or brief naps during wake (lingering in the sleep ghost). The time taken to pass through a bottleneck, and hence a measure of the duration of a brief awakening or nap, obeys a square-root scaling law: $|D_v - D_v^*|^{-1/2}$, where D_v^* is a bifurcation value [121]. Thus, increasing proximity to a ghost increases the time taken to pass through it. This idea will be elaborated upon in Sec. 2.4.2 and the effect of the ghosts on the model dynamics in response to stimuli will be discussed in Sec. 2.5.

2.4 Impulsive External Stimuli

Having characterized the dynamics of the model in V_v–V_m space, we now explore its response to external stimuli, which are represented as time-dependent vectors $\Delta\mathbf{D}(t) = [\Delta D_v(t), \Delta D_m(t)]$. Pharmacological agents and sensory stimuli alike can be modeled by the relative effects of their mechanistic pathway on the VLPO and MA groups, with stimulants presumably characterized by $\Delta D_m \geq 0$ and $\Delta D_v \leq 0$, and sedatives by $\Delta D_m \leq 0$ and $\Delta D_v \geq 0$. The resulting perturbation on the sleep-wake dynamics can be deduced by solving the model equations. This method for treating external stimuli applies generally, but in this chapter we focus on impulsive stimuli acting over short time scales. In Sec. 4.4.1, the opposite limit is considered: the impact of slowly-varying

external stimuli. What is meant by an impulsive stimulus is explained in Sec. 2.4.1, and the arousal state responses to such stimuli are explored in Sec. 2.4.2. Then, in Sec. 2.5, excitatory sensory stimuli applied during sleep are modeled.

2.4.1 Impact of Stimulus Duration

For a drive acting on a time scale $\ll 24\,\mathrm{h}$, we can neglect variation in D_v, which is treated as a constant over the duration of the impulse. Such *impulsive* drives can be analyzed as trajectories through V_v–V_m space at a constant D_v. Further, for drives acting on a time scale $\ll \tau_m, \tau_v = 10\,\mathrm{s}$, trajectories through V_v–V_m space will be minimumslly affected by the vector field $\dot{\mathbf{V}}$ during the impulse. In this high-amplitude, short-duration (δ-function) limit, the impact of a perturbative drive can be determined analytically. For a drive ΔD_m directed at the MA group, for example, we use Eq. (2.3):

$$\tau_m \dot{V}_m = -V_m + \nu_{mv} Q_v + D_m^0 + \Delta D_m. \tag{2.27}$$

Assuming that $|\Delta D_m| \gg |-V_m + \nu_{mv} Q_v + D_m^0|$, the approximate form $\tau_m \dot{V}_m \approx \Delta D_m$ is obtained. Integrating over the duration of the impulse, from t_1 to t_2, yields

$$\Delta V_m = V_m(t_2) - V_m(t_1) \approx \tau_m^{-1} \int_{t_1}^{t_2} \Delta D_m dt. \tag{2.28}$$

Similarly, a δ-function drive ΔD_v to the VLPO will produce a change in V_v of

$$\Delta V_v = V_v(t_2) - V_v(t_1) \approx \tau_v^{-1} \int_{t_1}^{t_2} \Delta D_v dt. \tag{2.29}$$

In combination as $\Delta\mathbf{D}$, the mean cell-body potentials V_m and V_v will change by the amounts given by Eqs (2.28) and (2.29), respectively.

In Fig. 2.7, ΔD_m impulses of varying duration are applied at $D_v = 3\,\mathrm{mV}$ for a constant value of the integral $\int \Delta D_m dt = 180\,\mathrm{mV\,s}$. In the δ-function limit, a change $\Delta V_m = \tau_m^{-1} \int \Delta D_m dt = 18\,\mathrm{mV}$ is produced. As illustrated in Fig.

2.7, as the duration of the impulse increases, so does the trajectory's deviation from the δ-function limit due to the velocity vector field $\dot{\mathbf{V}}$ [Eq. 2.13], which includes the terms neglected in the limit. For the remainder of this chapter we focus on δ-function impulses, which can be represented precisely in terms of the ΔV_v and ΔV_m they produce, using Eqs (2.28) and (2.29). Realistic impulsive stimuli of nonzero duration are perturbed from this limit, but can be compared similarly, through a numerical mapping to the corresponding ΔV_v and ΔV_m they produce. We therefore assert that the trends obtained using δ-function stimuli are qualitatively comparable to those that would be obtained using impulsive stimuli of nonzero duration. Note that in the following, when $\Delta\mathbf{D} \neq \mathbf{0}$, we are careful to distinguish unperturbed drives D_v^0 and D_m^0 from the total drives D_v and D_m where appropriate; although this distinction is not essential when dealing with instantaneous δ-function stimuli.

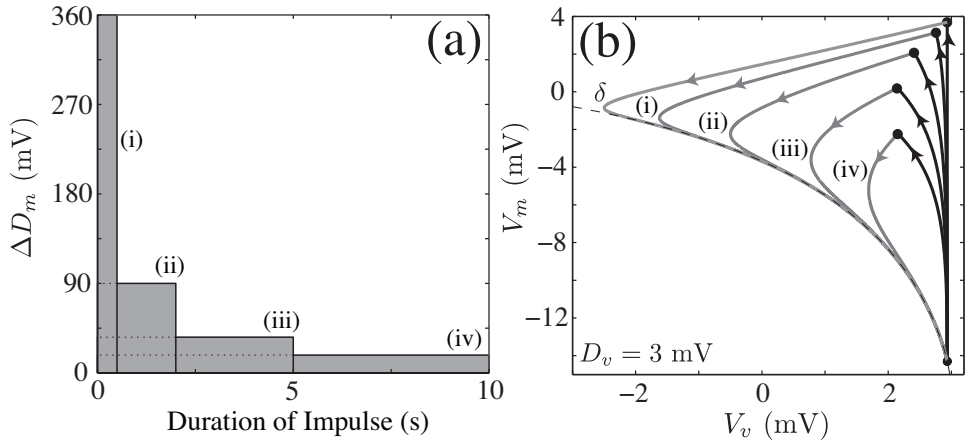

Figure 2.7: *The model's response to discrete ΔD_m drives of different durations. (a) ΔD_m profiles for drives of duration (i) 0.5 s, (ii) 2 s, (iii) 5 s, and (iv) 10 s, with $\int \Delta D_m dt = 180$ mV s, a constant. (b) Corresponding trajectories through the V_v–V_m plane during an impulse (black) and during relaxation (gray), at $D_v = 3$ mV. As the impulse duration increases, the trajectories are increasingly distorted away from the δ-function limit (a vertical line).*

2.4.2 Perturbative Drives ΔD

In the presence of external stimuli, there will be variation in both ΔD_m, due to external sensory stimuli, for example (c.f. Sec. 2.5), and ΔD_v, due to a noisy circadian signal, for example. Whatever the cause of these fluctuations, we model a single impulsive stimulus using a δ-function drive $\Delta\mathbf{D}$, as described above. In V_v–V_m space, impulsive changes to an initial condition at a stable equilibrium (V_v^*, V_m^*) are given by Eqs (2.28) and (2.29), perturbing it to $(V_v^* + \Delta V_v, V_m^* + \Delta V_m)$. We define the *sleep latency* t_{lat} as the time taken for the trajectory to return to a stable wake or sleep node. The threshold used to define a return to equilibrium is $\dot{V} < 5 \times 10^{-3}\,\text{mV}\,\text{s}^{-1}$. This problem of setting a precise threshold for 'sleep' is akin to the clinical rules for defining a sleep state [72], or an 'arousal' [124] from what is essentially a continuous process. Measures of arousal are not always consistent across studies [125] and, as is done here, a reasonable measure is applied consistently. Small changes in the $\dot{V}$ threshold would slightly alter the quantitative t_{lat} values but not the qualitative trends of our analysis. In the following, we investigate the model's response to stimuli at $D_v = 1\,\text{mV}$ (wake), $D_v = 2\,\text{mV}$ (bistable), and $D_v = 3\,\text{mV}$ (sleep) as a representative sample of the model regimes, as shown in Fig. 2.8. We use the final steady state and the latency t_{lat} to characterize the impact of a stimulus and interpret the results in terms of the model dynamics.

In accordance with the linear stability analysis of Sec. 2.3.2, at the cessation of an impulse, trajectories through the V_v–V_m plane attract rapidly onto the W^+ manifold (shown dashed in Fig. 2.8), on which slower dynamics occur. Since t_{lat} is therefore dominated by movement along the W^+ manifold, patterns of almost equivalent t_{lat} can be seen along the fast eigendirections from the shading in Fig. 2.8. Impulses landing on the W^- of a stable node will rapidly attract onto that fixed point, and are seen as black regions ($t_{\text{lat}} \approx 0$). On the other hand, a perturbation whose return trajectory passes through a low $\dot{V}$ region, like those surrounding a saddle point or a ghost, will take much longer to return to

equilibrium, and are seen as light regions ($t_{\rm lat} \gtrsim 6\,{\rm min}$). Example trajectories through V_v–V_m space are shown in Fig. 2.8 to illustrate the dynamics.

The qualitative topological landscape of V_v–V_m space is similar at low and high D_v, where a single stable node equilibrium and a ghost exist, as shown in Figs 2.8(a) and (b) for $D_v^0 = 1\,{\rm mV}$, and Figs 2.8(g) and (h) for $D_v^0 = 3\,{\rm mV}$. Since only one stable equilibrium exists, no transient stimulus can produce a lasting change in state. The latency $t_{\rm lat}$ to return back to the initial equilibrium state is minimumsl for drives that perturb the initial condition to near the W^- manifold of the stable node, and maximumsl for trajectories passing through the near-stable ghost. In the presence of external perturbations $\mathbf{\Delta D}$, brief naps during wake bouts (by lingering in the sleep ghost) and brief awakenings during sleep bouts (by lingering in the wake ghost) can occur. Since the wake ghost extends further from the relevant saddle-node bifurcation than the sleep ghost, as shown in Fig. 2.6(a), brief awakenings during sleep are favored over brief naps during wake. This finding is qualitatively consistent with the occurrence of brief sleep-wake transitions throughout the sleep periods of mammalian species [126]. The presence of arousals during sleep are assumed to maintain the sleeper's association with their surrounding environment, reacting to possible indicators of danger [125]. The role of the wake ghost in stabilizing the waking state during sleep is discussed further throughout Sec. 2.5, in which the slowing of trajectories near it, as a brief awakening, is demonstrated explicitly. Persistent stimuli $\mathbf{\Delta D}$ could act to further stabilize the ghosts, producing longer episodes in them: as prolonged naps during normal waking hours, or extended periods of waking (sleep deprivation) during normal sleeping hours. For now, such effects are simply described qualitatively, as characteristic features of the model dynamics, and will be explored in more detail in future work.

At $D_v^0 = 2\,{\rm mV}$, in the bistable region, we investigate initial conditions at the wake node, shown in Figs 2.8(c) and (d), and at the sleep node, shown in Figs 2.8(e) and (f). A transient stimulus is able to elicit a change of state between sleep and wake if it perturbs the trajectory across the separatrix formed by

the stable invariant manifold W^- of the saddle point (visible in the ΔV_m–ΔV_v and V_v–V_m plots of Fig. 2.8 as a white region and a dot-dashed line, respectively). If the return trajectory passes near the saddle point, it will take much longer to reach the relevant stable node because of the region of low $\dot{V}$ that surrounds it [cf. Fig. 2.6(c)]. On the other hand, a perturbation to near the fast manifold W^- of either stable node will result in rapid attraction onto it. Therefore, to achieve a rapid change in state, an optimum set of drives $\Delta\mathbf{D}$ exist, corresponding to a perturbation onto the W^- of the alternate stable node. In summary, the behavior of the model can be explained in terms of regions of near-stability: ghosts and the low $\dot{V}$ region surrounding the saddle point, which lengthen t_{lat}, and the fast dynamics along the stable invariant manifolds W^- of the stable nodes, which shorten t_{lat}.

2.5 Arousing Stimuli During Sleep

Having characterized the dynamics of the model in response to general impulsive stimuli, we now consider the specific case of external sensory stimuli applied during sleep. This scenario corresponds to clinical sleep fragmentation protocols that use auditory stimuli to fragment sleep [16]. Auditory tones, like other external sensory stimuli, excite MA nuclei [118, 127, 128], perhaps via the orexin group [129, 130] or from ACh [131, 132]. Assuming no *direct* impact on the VLPO (i.e., only indirectly via increased inhibition from MA firing), we model a short, loud auditory tone by an excitatory δ-function drive ΔD_m, leaving $\Delta D_v = 0$. In the bistable region ($1.45\,\text{mV} < D_v < 2.46\,\text{mV}$), the arousing stimulus can cause a transition to the stable wake node, producing a permanent arousal. However, here we consider the range $D_v > 2.46\,\text{mV}$ for which the stable sleep node and the wake ghost are the main dynamical features of the model; i.e., for the topology shown in Figs 2.8(g) and (h). The impulse strength and time-of-night variations in the model's response to such sensory

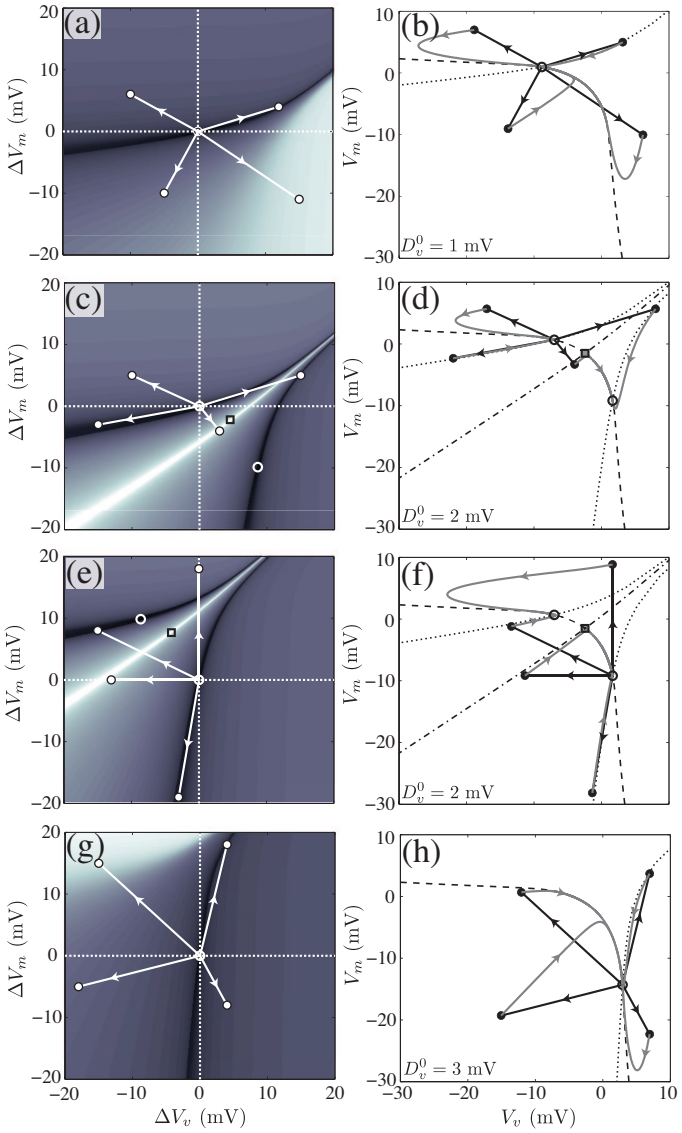

Figure 2.8: *Model responses to δ-function* $\Delta\mathbf{D}$ *stimuli.* ΔV_v–ΔV_m *and* V_v–V_m *plots are shown for (a)-(b)* $D_v^0 = 1\,\mathrm{mV}$ *(initial condition: wake node), (c)-(d)* $D_v^0 = 2\,\mathrm{mV}$ *(initial condition: wake node), (e)-(f)* $D_v^0 = 2\,\mathrm{mV}$ *(initial condition: sleep node), and (g)-(h)* $D_v^0 = 3\,\mathrm{mV}$ *(initial condition: sleep node). In the* ΔV_v–ΔV_m *plots (defined relative to the initial equilibrium), the sleep latency* t_{lat} *is represented using shading, from 0 min (black) to* $> 6\,\mathrm{min}$ *(white). Sample δ-function impulses are shown as white arrows, with the corresponding trajectories through* V_v–V_m *space shown in the adjacent plots for the impulse (black) and during relaxation back to a stable node (gray). Equilibriums (open white circles and black squares) and invariant manifolds (dotted, dashed, and dot-dashed lines) are labeled as per Fig. 2.6. Note that points in the* ΔV_v–ΔV_m *plane should be interpreted in terms of the δ-function drives* (ΔD_v,ΔD_m) *that produce them [cf. Sec. 2.4.1].*

stimuli are explored in Secs 2.5.1 and 2.5.2, respectively. This analysis is then used to simulate a sleep fragmentation study in Sec. 2.5.3.

2.5.1 Impulse Strength Dependence

Figure 2.9(a) shows the monotonic increase of the time to return to sleep t_{lat} with stimulus strength ΔV_m for $D_v = 3\,\text{mV}$. The plot features two regions of steep gradient. The first, at low ΔV_m, is due to the region of low $\dot{V}$ surrounding the sleep node. As illustrated in Fig. 2.9(b), the rapid rise in t_{lat} at a higher stimulus strength corresponds to the return trajectory passing through the low $\dot{V}$ wake ghost. Increasing the intensity of the applied impulse past this point has relatively little effect on t_{lat} because increases in $\dot{V}$ beyond the wake ghost largely counteract the additional stimulus. Hence the time spent in the wake ghost dominates t_{lat}, which saturates at large ΔV_m.

In this model, the point of inflection of the ΔV_m–t_{lat} curve is taken to define a sleep–wake transition. The ΔV_m at this point defines the *arousal threshold* $\mathcal{A}$, which represents the mean increase in MA cell-body potential required to trigger an arousal from sleep. This is a suitable measure because stronger stimuli $\Delta V_m > \mathcal{A}$ produce a prolonged arousal and weaker stimuli $\Delta V_m < \mathcal{A}$ cause a rapid return to sleep, as illustrated in Fig. 2.9. Clinically, the arousal threshold is measured in terms of the magnitude of a given sensory stimulus, in units of auditory intensity or pressure deviation, for example. Our measure of the arousal threshold, $\mathcal{A}$, should therefore be comparable to clinical measures, as explored in Sec. 2.5.2 below. We define the *critical sleep latency* $\mathcal{T}$ as the latency to return to sleep t_{lat} after receiving the critical impulse $\mathcal{A}$, as labeled in Fig. 2.9(a).

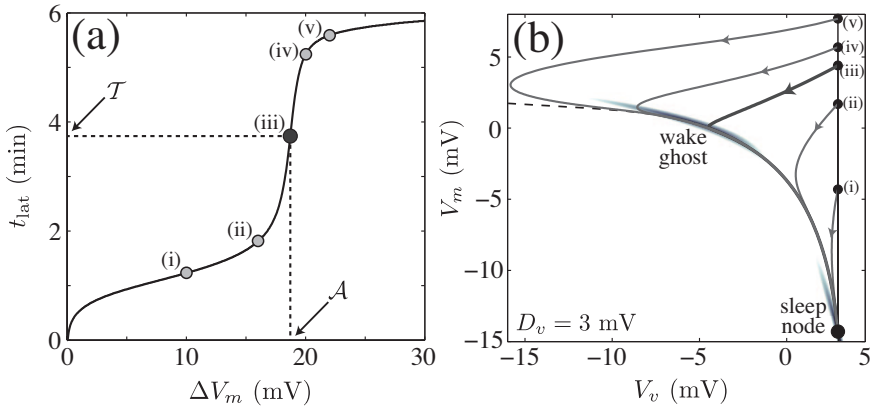

Figure 2.9: *The model's response to excitatory δ-function sensory stimuli ΔD_m of varying magnitude applied during sleep ($D_v = 3\,\mathrm{mV}$). (a) The time to return to sleep t_{lat} following the impulse is plotted as a function of its strength ΔV_m. For the five points marked in (a): ΔV_m = (i) $10\,\mathrm{mV}$, (ii) $16\,\mathrm{mV}$, (iii) $18.7\,\mathrm{mV}$ (the point of inflection), (iv) $20\,\mathrm{mV}$, and (v) $22\,\mathrm{mV}$, corresponding trajectories through V_v–V_m space are shown in (b), where regions of $\dot{V} < 0.1\,\mathrm{mV\,s^{-1}}$ have been shaded. The point of inflection is shown as a larger, filled circle in (a), with the arousal threshold $\mathcal{A}$ taken from the ΔV_m at this point and the critical sleep latency $\mathcal{T}$ taken from the t_{lat} at this point, as labeled.*

2.5.2 Time-of-Night Variation

Rather than explicitly investigating the impact of stimuli as a function of the time since sleep onset, it is more convenient to study them as a function of the sleep drive D_v. Trends in D_v can then be mapped to trends in time using the variation in $D_v(t)$ across a normal night of sleep, shown in Fig. 2.2(e). Since $Q_m \approx 0\,\mathrm{s^{-1}}$ during sleep, Eq. (2.8) becomes $\chi\dot{H} \approx -H$, and H approximates exponential decay. Therefore, during sleep, the drive $D_v(t)$ varies as the weighted sum of sinusoidal $C(t)$ and exponential decay $H(t)$ components, peaking near the middle of the night.

The model's response to $\Delta V_m = 18\,\mathrm{mV}$ stimuli as a function of D_v is shown in Fig. 2.10. The observed behavior can be explained in terms of both the minimum $|\dot{V}|$ in the wake ghost, which decreases with increasing D_v, and the position of the sleep node, which moves to a higher V_v and lower V_m with in-

creasing D_v. At $D_v = 2.5\,\mathrm{mV}$, near the saddle-node bifurcation of the wake node, the return trajectory lingers in the wake ghost for $\sim 10\,\mathrm{min}$ before returning to sleep, as shown in Fig. 2.10(a). At $D_v = 3\,\mathrm{mV}$, as shown in Fig. 2.10(b), the return trajectory passes through a smaller region of the wake ghost, lingering there for only $\sim 1\,\mathrm{min}$. As D_v increases further, the $\Delta V_m = 18\,\mathrm{mV}$ stimuli are no longer strong enough to perturb the system to near the wake ghost. Instead, the trajectories return ever more rapidly to sleep under the influence of the vector field $\dot{\mathbf{V}}$, as demonstrated in Figs 2.10(c) and (d). Thus we find that at low D_v, an impulse has a much greater impact, producing a greater maximum V_m, and taking a longer time to return to sleep than the same impulse applied at high D_v. It follows that as D_v increases, stronger impulses are required to excite the system from the sleep node to the wake ghost – the arousal threshold increases with D_v.

The ΔV_m–t_{lat} curves discussed in Sec. 2.5.1 also depend on D_v, as illustrated in Fig. 2.11(a) using the same D_v values as in Fig. 2.10. Consistent with the trends explained above, the ΔV_m–t_{lat} curves shift to greater $\mathcal{A}$ (higher arousal threshold) and a lower $\mathcal{T}$ (the minimum $\dot{V}$ in the wake ghost is lower) as D_v increases. A plot showing the variation of both $\mathcal{A}$ and $\mathcal{T}$ with D_v is shown in Fig. 2.11(b). We find an approximately linear relationship between $\mathcal{A}$ and D_v [because the sleep branch and the minimum $\dot{V}$ in the wake ghost are approximately linear for $D_v > 2.46\,\mathrm{mV}$, as can be seen in Fig. 2.6(a)]:

$$\mathcal{A} \approx 6.5 D_v - 0.9\,\mathrm{mV}. \tag{2.30}$$

Since the time spent in a ghost decreases as the inverse square root of the difference between the parameter and its bifurcation value [121], the critical sleep latency $\mathcal{T}$ can be approximated by

$$\mathcal{T} \approx \left[111 \left(\frac{D_v}{1\,\mathrm{mV}} - 2.46 \right)^{-1/2} + 74.0 \right] \mathrm{min}, \tag{2.31}$$

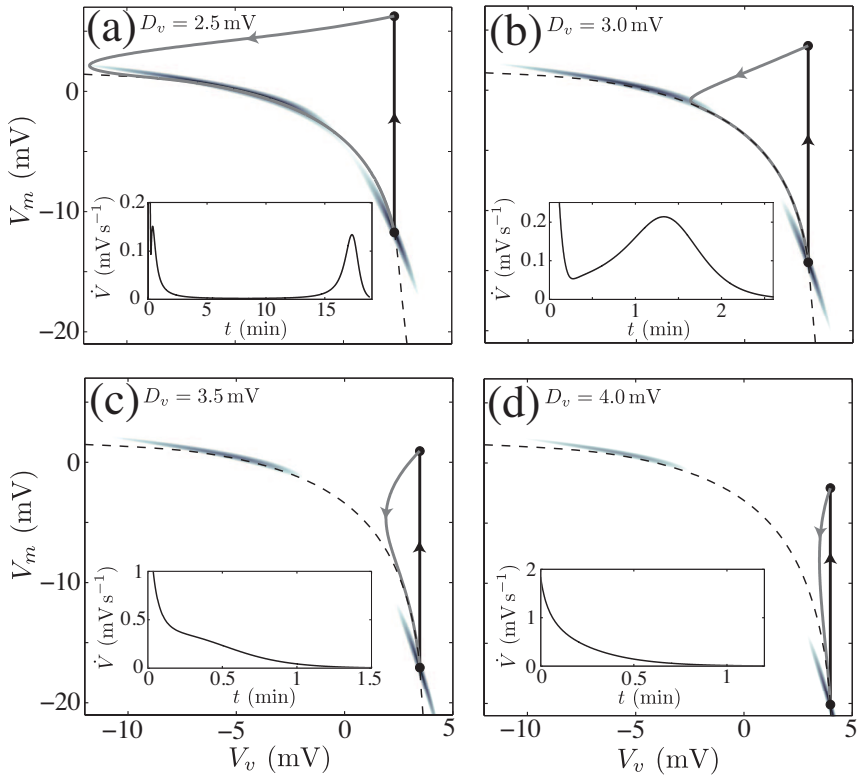

Figure 2.10: *The model's response to* $\Delta V_m = 18\,\mathrm{mV}$ *δ-function impulses at different values of the sleep drive* D_v*. Trajectories through the* V_v*–*V_m *plane are plotted during excitation (black) and relaxation (gray) for* $D_v =$ *(a)* $2.5\,\mathrm{mV}$*, (b)* $3.0\,\mathrm{mV}$*, (c)* $3.5\,\mathrm{mV}$*, and (d)* $4.0\,\mathrm{mV}$*. Regions of* $\dot{V} < 0.1\,\mathrm{mV\,s^{-1}}$ *are shaded and plots of* $\dot{V}$ *as a function of time along each trajectory are shown inset. Note that the vertical scale of the inset figures is chosen to show the main features of the return to equilibrium, which does not always include the initial maximum in* $\dot{V}$*.*

for $D_v > 2.46\,\mathrm{mV}$, which diverges as D_v approaches the bifurcation value $D_v = 2.46\,\mathrm{mV}$. Using the known variation of $D_v(t)$ across a normal sleep night, $\mathcal{A}(D_v)$ and $\mathcal{T}(D_v)$ are transformed to functions of the time since sleep onset, as shown in Figs 2.11(c) and (d). The trend in $\mathcal{T}$ could be measured experimentally using sleep latency tests across the night, but to our knowledge this has not yet been performed. Because the t_{lat} and hence $\mathcal{T}$ values remain uncalibrated (since this depends on the choice of the threshold $\dot{V} < 5 \times 10^{-3}\,\mathrm{mVs}^{-1}$ at which a trajectory is considered 'close' to equilibrium), we seek to validate only the qualitative trends through experiment.

The model predicts that the arousal threshold will peak near the middle of the night, as shown in Fig. 2.11(d). This is qualitatively consistent with some clinical studies [133–137] but is inconsistent with others, that find a steady increase of arousal threshold across the night [17, 138, 139], as measured from the critical intensity I_c (dB) of the auditory stimulus required to cause an arousal. However, a monotonically increasing arousal threshold is likely the result of progressive habituation to the auditory stimulus, which makes it less effective with increased exposure, and which we have not attempted to model here. A study reported by Bonnet *et al.* [134] aroused subjects only five to eight times each night, minimizing the effects of the frequent nocturnal disruptions. It is therefore a suitable study with which to compare the predictions of our model, which assumes that sleep is minimumslly disturbed. The experimental I_c data adapted from the Bonnet *et al.* study is shown alongside our measure $\mathcal{A}$ in Fig. 2.11(d), showing good agreement. The systematic increase of the I_c data relative to $\mathcal{A}$ with time is likely the result of a small habituation effect. A linear fit between the two measures yields

$$I_c \approx \left[2.9\frac{\mathcal{A}}{1\,\mathrm{mV}} - 7.1\right]\,\mathrm{dB}, \tag{2.32}$$

giving a relationship between the intensity of an auditory stimulus I_c and the increase in MA cell-body potential $\mathcal{A}$ required to trigger an awakening from

sleep. Combined with Eq. (2.30), $I_c(t)$ can then be inferred from $D_v(t)$ across *any* sleep period.

2.5.3 Modeling Sleep Fragmentation

The importance of the above calibration between I_c and $\mathcal{A}$ is demonstrated by simulating a sleep fragmentation protocol reported by Lammers *et al.* [136]. In this study, nine male subjects were required to make a microswitch closure in response to a series of 2 s long, 1000 Hz auditory tones applied 4 min after every entry into Stage 2 sleep. Choosing a threshold $\dot{V} < 0.1\,\mathrm{mV\,s^{-1}}$ to define a return to Stage 2 sleep, we simulate this protocol by repeatedly applying discrete 2 s ΔD_m impulses 4 min after this threshold is crossed. The strength of the impulses is chosen to produce a ΔV_m equal to the arousal threshold $\mathcal{A}$, which is calculated from D_v using Eq. (2.30). However, the strength $\Delta V_m = \mathcal{A}$ given by Eq. (2.28) applies to δ-function impulses and needs to be increased to obtain the same ΔV_m for 2 s impulses [c.f., Sec. 2.4.1]; a magnitude $\Delta D_m = 1.1 \times (\mathcal{A}/2)$ achieves this. The resulting fragmented time series for V_m and H are shown in Figs 2.12(a) and (b), respectively. The V_m time series is characterized by recurring increases to waking levels of activity, in contrast to unperturbed sleep in which V_m, and hence the firing rate Q_m, is low throughout the night, producing consolidated sleep. The increase in the average Q_m across the night feeds back onto the sleep cycle via the homeostatic source term μQ_m [cf. Eq. (2.8)] – adenosine production is increased and sleep is less restorative. The progressive increase in H over normal levels is shown in Fig. 2.12(b). Compared to normal sleep, an increased homeostatic component to the sleep drive $D_v = D_v^0 = \nu_{vc}C + \nu_{vh}H$ causes it to peak later in the night and at a higher value. Since $\mathcal{A}$ depends approximately linearly on D_v [Eq. (2.30)] and I_c depends approximately linearly on $\mathcal{A}$ [Eq. (2.32)], the arousal threshold I_c will also peak later in the night and at a higher value, as shown in Fig. 2.13. In this figure, the data from the Lammers *et al.* study

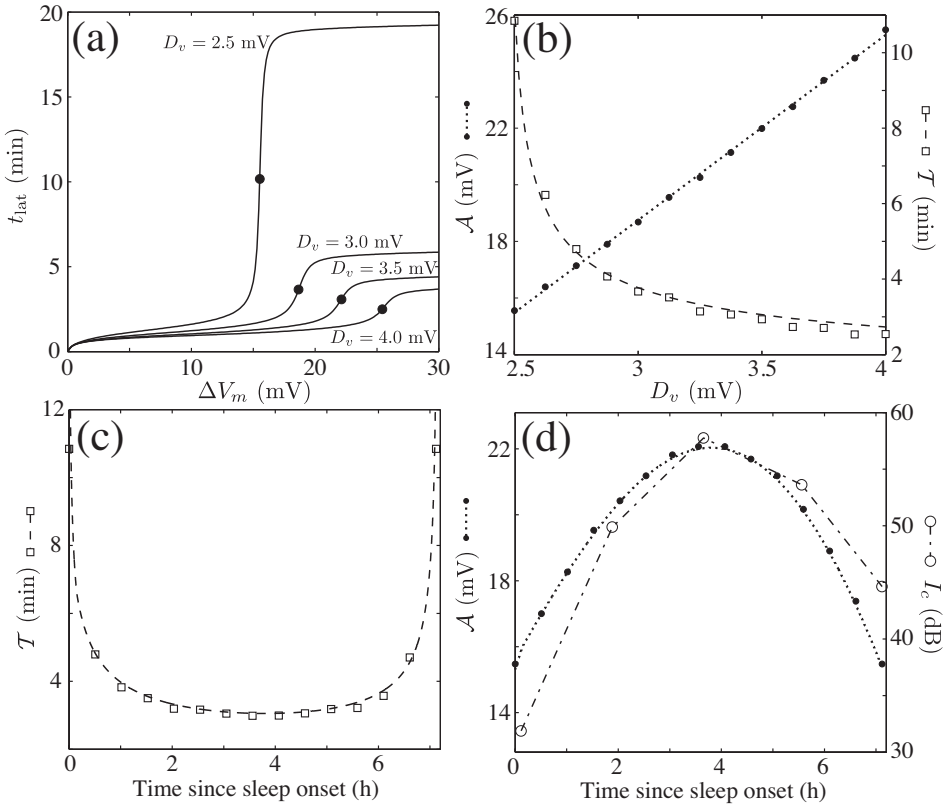

Figure 2.11: *Time-of-night variation in the arousal threshold $\mathcal{A}$ and critical sleep latency $\mathcal{T}$. (a) ΔV_m–$t_{\rm lat}$ curves are plotted for $D_v = 2.5\,{\rm mV}$, $3.0\,{\rm mV}$, $3.5\,{\rm mV}$, and $4.0\,{\rm mV}$. Points of inflection are marked with circles. (b) $\mathcal{A}$ as a function of D_v (circles) with a fitted dotted line [Eq. (2.30)] and $\mathcal{T}$ as a function of D_v (squares) with a fitted dashed line [Eq. (2.31)]. (c) $\mathcal{T}$ and (d) $\mathcal{A}$ across the first $\sim 7\,{\rm h}$ of sleep (the portion for which $D_v > 2.46\,{\rm mV}$), with the fits from (b) shown dashed and dotted, respectively. Clinical auditory arousal threshold I_c data from Bonnet et al. [134] is displayed using open circles and a dot-dashed line in (d).*

[136] is shown alongside our model predictions, revealing a good agreement. However, in order to quantitatively reproduce the auditory arousal threshold I_c values, an additional offset of $+9\,\mathrm{dB}$ relative to the previous calibration [Eq. (2.32)] was required. As well as inter-individual differences in the quantitative values of the auditory arousal threshold due to age and other effects, a large inter-study variation (e.g., from 36 dB to 91 dB in Stage 4 sleep) is also evident, perhaps due to differing amounts of background noise in sleep labs or different clinical definitions of 'arousal' [140]. In this light, the shift of only 9 dB used here seems reasonable.

In addition to the arousal threshold, the Lammers *et al.* study simultaneously recorded body temperature, which is known to exhibit a circadian variation [141]. The authors proposed a negative relationship between body temperature and arousal threshold, implying that $-D_v$ in our model (which includes a circadian component) should reflect the body temperature variation. Indeed it does, allowing us to deduce a linear fit between D_v and body temperature T_{bod}:

$$T_{\mathrm{bod}} \approx \left[-0.241\frac{D_v}{1\,\mathrm{mV}} + 37.9\right]^{\circ}\mathrm{C}. \tag{2.33}$$

The predicted T_{bod} curve, as deduced from $D_v(t)$ using Eq. (2.33), is plotted as a dotted line in Fig. 2.13.

The model's ability to simultaneously reproduce the arousal threshold and body temperature curves during sleep fragmentation is a consequence of its physiological formulation, which allows us to exploit the known impact of sensory stimuli on MA nuclei to model sleep fragmentation. There are two free parameters: the $\dot{V}$ threshold to Stage 2 sleep, which has a sensible value (near the sleep node), and the offset of 9 dB, which does not affect the qualitative trends and is modest compared to inter-study variability [140]. The success of this approach allows the arousal threshold and body temperature curves to be interpreted in terms of the physiological processes that produce them: the homeostatic and circadian components of the drive D_v to the VLPO. Frequent

arousals reduce the clearance rate of H, diminishing the restorative value of sleep and causing D_v and hence I_c and $T_{\rm bod}$ to reach an extremum of greater magnitude later in the night.

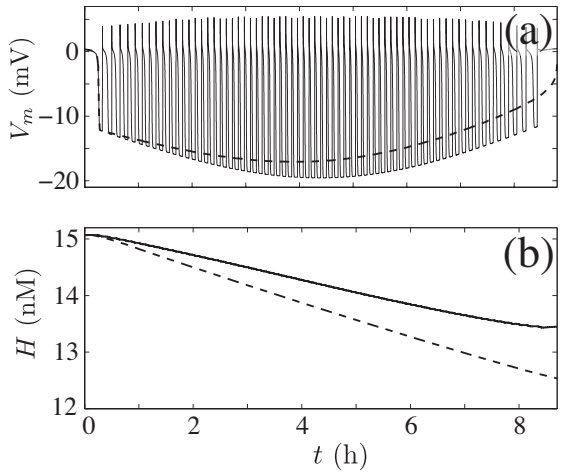

Figure 2.12: *The model's simulation of the sleep fragmentation protocol reported by Lammers et al. [136]. (a) V_m and (b) H as a function of time for fragmented (solid) and normal (dashed) sleep.*

2.6 Summary and Discussion

Within a phyiologically-based mathematical model of the sleep-wake switch, we have used a separation of time scales and linear stability analysis to gain detailed insights into the impact of impulsive stimuli on arousal state. Stimuli acting on the system are represented as $\Delta\mathbf{D}(t)$ vectors, allowing a unified representation of diverse external influences. Through an analysis of the model dynamics, brief naps during wake and brief awakenings during sleep were shown to be a consequence of the model's sleep and wake ghosts. Brief awakenings during sleep are favored over brief naps during wake, a finding qualitatively consistent with experimental observations [126]. The set of drives that pro-

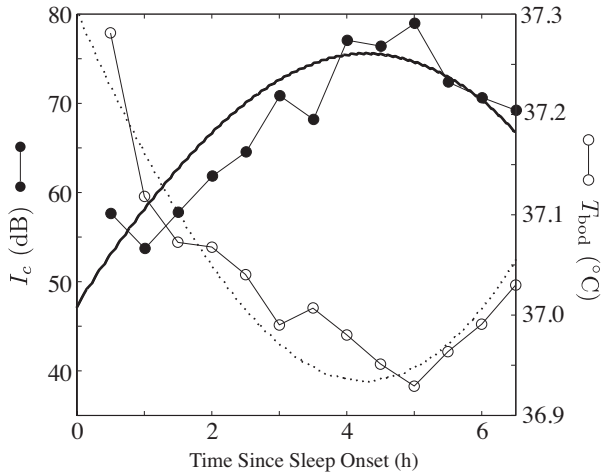

Figure 2.13: *The model's simulation of the sleep fragmentation protocol reported by Lammers et al. [136]. The auditory arousal threshold I_c (solid circles) and body temperature $T_{\rm bod}$ (open circles) data are plotted alongside the model's predictions for I_c [as inferred from $D_v(t)$ using Eqs (2.30) and (2.32)] (solid line) and $T_{\rm bod}$ [as inferred from $D_v(t)$ using Eq. (2.33)] (dotted line). A 9*dB *offset relative to the calibration to the Bonnet et al. data [134] is added to the model's I_c predictions. The model formulation emulates the clinical protocol: 2*s *impulses of strength equal to the arousal threshold $\mathcal{A}$ are applied 4*min *after every entry into Stage 2 sleep (defined as the $\dot{V} < 0.1\,\mathrm{mV\,s^{-1}}$ region surrounding the sleep node).*

duce a change in state between sleep and wake perturb the system across the separatrix in the V_v–V_m plane, with fast and slow transitions characterized by trajectories following the invariant manifold W^- or the low $\dot{V}$ region surrounding the saddle point, respectively. In Sec. 2.5, auditory stimuli applied during sleep were modeled according to their known excitation of MA brainstem populations: by drives $\Delta D_m > 0$. In the δ-function limit, these impulses produce impulsive changes ΔV_m to V_m. The sharp rise in the ΔV_m–$t_{\rm lat}$ curve, due to a lag associated with the wake ghost, allowed us to define the arousal threshold $\Delta V_m = \mathcal{A}$, which was found to depend approximately linearly on D_v. It therefore varies as the weighted sum of sinusoidal C and exponential H components, peaking near the middle of the night. This trend in $\mathcal{A}$ matches the clinical variation of the auditory arousal threshold I_c, against which it was cal-

ibrated. As a result, the time-of-night I_c variation for any arbitrary sleep-wake protocol can be inferred from D_v, as they are approximately linearly related. The significance of this finding was demonstrated by simulating a clinical sleep fragmentation protocol reported by Lammers *et al.* [136]. The observed time-of-night arousal threshold and body temperature curves were quantitatively reproduced, including the skew of the peak of the arousal threshold towards the latter half of the night and its increase in magnitude relative to normal sleep. We propose that an increase in the homeostatic sleep drive due to the frequent awakenings is the cause of this change.

A core idea that stems from the general formulation of stimuli as vectors $\Delta\mathbf{D}(t)$ is that diverse stimuli can be compared in the same space. For example, in addition to the more prevalent studies of auditory arousal thresholds considered in this work, arousal thresholds have also been measured for pain, pressure, temperature, light intensity, and olfactory stimuli [140]. In particular, the respiratory effort (measured in units of pressure) in obstructive sleep apnea-hypopnea syndrome (OSAHS) patients provides another well-studied measure of the arousal threshold, which presumably acts via ΔD_m [142, 143]. Studies measuring the time-of-night arousal threshold of OSAHS patients, like that of Sforza *et al.* [144], show a qualitatively similar trend to our $\mathcal{A}$, but more detailed studies like that of Berry *et al.* [145] show an oscillation on a time scale of $\sim 128\,\mathrm{min}$. This fine oscillatory variation is perhaps the result of ultradian dynamics which, if included in this model, would effectively constitute an oscillatory D_m^0 [50], modulating the arousal threshold accordingly. Within the Phillips-Robinson framework, a simple OSAHS model may consist of a monotonically increasing drive ΔD_m, triggered by a certain vicinity to the sleep node, and increasing until the arousal threshold $\mathcal{A}$, where the obstruction is resolved. Since the apneic drive ΔD_m acts over an extended time scale compared to the impulsive stimuli of the present work, the resulting dynamics will be different. Extending the current framework towards a predictive physiologically-based model of OSAHS is a target for future work.

Although this work focuses on impulsive stimuli, which constitute merely transient disturbances to the sleep-wake cycle, drives acting over extended time scales can also be represented as $\Delta\mathbf{D}$. These persistent drives perturb the position of the equilibrium points themselves, altering the broader arousal state dynamics. Slowly-varying $\Delta\mathbf{D}$ drives could be used to describe gradual changes in temperature, the impact of pharmaceuticals with extended biological half-lives, or neurological pathologies such as narcolepsy, for example. A way of representing such drives will be developed in Sec. 4.4.1.

In Chapter 3, we model enforced waking protocols using a persistent drive that maintains the system in the wake ghost during normal sleep periods. The external drive required to keep the subject awake is small (owing to the small $\dot{V}$ in the wake ghost) and could be provided in the form of an arousing 'effort', as a positive ΔD_m, for example, that may be cortical and/or orexinergic in origin [146–148]. The effort ΔD_m increases with D_v, as the wake ghost moves further from stability; consistent with the increasing difficulty in remaining awake at a high physiological sleep pressure. A simulation of fatigue during sleep deprivation is one application of this approach, and will be explored in detail in Chapter 3.

The properties of the ghost states suggest a qualitative reason why brief arousals during sleep are more prevalent than brief naps during wake (c.f., Sec. 2.4.2). A future task involves extending this approach towards a quantitative model that reproduces the observed scale-invariant trends [126], which may be achieved by adding noisy perturbations $\Delta\mathbf{D}$ to the system.

In summary, we have developed a framework for incorporating external stimuli into a physiologically-based model of the sleep-wake switch. Despite being a comparatively simple model, including only two neuronal populations and averaging over the ultradian rhythm, the orexin group, and cortical-level effects, we are able to gain insights into the basic neural mechanisms affecting arousal responses to impulsive stimuli. This study represents the first detailed exploration of the impact of external stimuli on arousal state, and takes an

approach that is fundamentally different to previous attempts. Where past models framed sets of data into a phenomenological structure, our model is of the known physiology of the sleep-wake switch. Stimuli are modeled by their impact on the neuronal populations that govern arousal state dynamics, and behavioral outcomes are subsequently deduced. The model's predictions are directly testable through comparisons to both physiological and clinical data, as a way of justifying the methodology, or providing evidence against it. The agreement between the model's predictions and the available data, discussed in the latter sections of this chapter, justifies our approach. Applying the above ideas to a broader range of stimuli, including pharmacological agents and other sensory stimuli is expected to guide developments in arousal state modulation and control in the future.

Chapter 3

Physiologically-Based Modeling of Subjective Fatigue During Sleep Deprivation

Abstract

A quantitative physiologically-based model of the sleep-wake switch is used to predict variations in subjective fatigue-related measures during sleep deprivation. The model includes the mutual inhibition of the sleep-active neurons in the hypothalamic ventrolateral preoptic area (VLPO) and the wake-active monoaminergic brainstem populations (MA), as well as circadian and homeostatic drives. In Chapter 2, the *wake ghost*, a near-stable waking state that exists at high values of the model's sleep drive, was identified. To simulate sleep deprivation, *wake-effort* is applied as a drive to the MA to maintain the system in the wake ghost during normal sleep periods. Physiologically, such a drive represents afferents from the cortex or the orexin group of the lateral hypothalamus. Psychologically, the need to exert effort to maintain wakefulness at high homeostatic sleep pressure is proposed to correlate with subjective fatigue. The model's agreement with subjective fatigue-related clinical mea-

sures supports this hypothesis. In two analogous 72 h clinical sleep deprivation protocols [149, 150], subjective fatigue, adrenaline, and, in one case, body temperature time series are reproduced by the model. This work demonstrates the strength of physiologically-based sleep modeling, which is able to infer psychological measures from the underlying physiological interactions that produce them.

3.1 Introduction

Workers in many professions, including medical practitioners, air-traffic controllers, and truck drivers, must undertake the inherently dangerous practice of operating under increasing levels of fatigue. However, humans are biologically ill-equipped to perform throughout the day and night [151], and widespread neglect of sleep is to the detriment of general health and well-being [66, 67]. Although the precise role of sleep is not yet fully understood, it is known that performance, learning ability, and mood suffer from sleep fragmentation [18, 19], sleep restriction [23], and total sleep deprivation [69, 71]. Fundamental to understanding the role of sleep, therefore, is to quantify the physiological and psychological consequences of sleep deprivation. In this work, we focus on the impact of total sleep deprivation using a quantitative physiologically-based model.

The timing of sleep and wake is largely determined by two main drives: the *homeostatic* 'sleep pressure', that builds with time spent awake and is relieved with sleep, and the ~ 24 h periodic *circadian* oscillation, which is entrained to the day-night cycle via photic input. During total sleep deprivation, the typical variations in subjective fatigue-related measures [12, 13, 149, 150, 152] and levels of performance detriment [13, 14, 149, 150, 153–155] include a monotonically increasing component – attributed to the increasing homeostatic sleep pressure – and an ~ 24 h periodic circadian modulation [91]. This combination of approximately linear and periodic components is also noted in a range of other

measures, including body temperature [14, 149, 150, 156, 157], percentage of EEG spent in alpha [15], and iron serum levels [158].

Sleep-wake modeling derives much from Borbély's 'two-process' model [56] that combined the homeostatic and circadian drives into a conceptual framework that was able to explain the timing of sleep and wake. Quantitative implementations of the phenomenological two-process model, beginning with that of Daan *et al.* [57], have since been able to reproduce a wide variety of sleep-wake phenomena [58]. However, with improved knowledge of the physiology responsible for sleep-wake dynamics, models that incorporate neuronal population-level interactions have been developed more recently [1, 62–64]. These physiologically-based sleep models have the advantage over phenomenological models of relating their behavioral predictions to the neurological processes that underpin them. In this work, we use a model of the sleep-wake switch developed by Phillips and Robinson [1].

Previous attempts at modeling fatigue variation during sleep deprivation have been predominantly phenomenological in nature [57, 58, 101, 159, 160]. In the two-process model, for example, a measure of fatigue is derived from the difference between the upper circadian threshold and the homeostatic *Process S* [57] (c.f., Sec. 1.4.2). Although the qualitative trends obtained in this way match those observed clinically, a clear physiological justification is lacking. A main motivation for the present work is to quantitatively relate phenomenological concepts about sleep deprivation to physiological mechanisms.

In this chapter we reproduce the observed trends in subjective fatigue-related measures within the context of a physiologically-based mathematical model of the sleep wake switch. In Sec. 3.2 the physiology of the sleep-wake switch, including the model formulation, is summarized. The output of the model is explained in detail, including the presence of hysteresis as a function of the model's sleep drive, the role of the wake ghost, and the wake effort drive. In Sec. 3.3, our methodology for modeling sleep deprivation is explained in terms of the postulated physiological processes responsible. We show how an

objective definition of *wake-effort* stems from the model, and demonstrate its correspondence with clinical sleep deprivation data. The effects of changes in the circadian and homeostatic components to the model's sleep drive, as well as changes in the initial homeostatic sleep pressure on the wake-effort curves are explored in Sec. 3.4 and a discussion of the main findings is presented in Sec. 3.5. Note that the parameters of the Phillips-Robinson model have been constrained rigorously in previous work [1, 81]. In the main text we describe the model's mathematical structure and dynamics qualitatively, focusing upon the clinical relevance of its predictions. Note that as this chapter is based on a paper aimed at a clinical audience, mathematical details are left for the Appendices and the dynamics are mainly described in the main text without the use of mathematics.

3.2 The Sleep Model

In this section we summarize the relevant sleep-wake physiology, and the formulation and basic output of the sleep model developed by Phillips and Robinson [1].

3.2.1 Formulation and Basic Output

The 'flip-flop' dynamics of sleep and wake, characterized by rapid transitions between the two distinct states, result from the mutual inhibition of wake-active monoaminergic neuronal populations in the brainstem (MA) and sleep-active GABAergic neurons in the ventrolateral preoptic area of the hypothalamus (VLPO) [49, 79]. The MA group includes nuclei that use monoaminergic neurotransmitters: the histaminergic tuberomammillary nucleus (TMN), norepinephrinergic locus coeruleus (LC), serotoninergic dorsal raphé nucleus (DR), and dopaminergic ventral tegmental area (VTA) [31, 107, 108]. Monoaminergic neurotransmitters inhibit the VLPO, and the VLPO inhibits the MA via

GABAergic projections [50, 51, 78]. Hence, the activity of each group suppresses the activity of the other, reducing the subsequent inhibition onto itself, and thereby indirectly reinforcing its own activity. This behavior results in extended periods of either sleep (activated VLPO and suppressed MA) or wake (activated MA and suppressed VLPO), with rapid transitions between the two states – much like a 'flip-flop' circuit [79].

The neuronal population model of the sleep-wake switch developed by Phillips and Robinson [1] quantitatively encapsulates this mutual inhibition between the MA and VLPO neuronal populations and the 'flip-flop' dynamics it produces. Transitions between sleep and wake states are modulated by input from external sources, which we term *drives* to each population. The MA group receives input from brainstem nuclei that express acetylcholine, including the pedunculopontine (PPT) and laterodorsal (LDT) tegmental nuclei in the mesopontine tegmentum [109, 110]. In addition, the orexin population of the lateral hypothalamic area excites MA and acetylcholine-related neuronal populations during wake, thereby acting to stabilize the waking state [111, 112]. In this model, drives to the MA from acetylcholine-related and orexinergic sources are averaged to a constant, intermediate level of input, a simplification that should not alter the qualitative dynamics between sleep and wake [1].

The VLPO receives input from circadian and homeostatic drives. The $\sim$ 24 h periodic circadian signal originates in the suprachiasmatic nucleus (SCN) and entrains the sleep-wake cycle to the light cycle through projections to the VLPO, primarily via the dorsomedial nucleus of the hypothalamus (DMH) [50, 51, 113]. Assuming the circadian drive C is well-entrained to the daily fluctuation in light intensity, we approximate it as a 24 h-periodic sinusoid. Our model of the homeostatic drive H represents the adenosine concentration in the basal forebrain, which builds during waking [107, 114, 115] and is cleared during sleep [115–117]. Adenosine disinhibits the VLPO via projections from basal forebrain neurons [50, 51]. Note that our homeostatic drive H plays the same qualitative role as Process S in the two-process model [56, 57]. The total

drive to the VLPO is termed the *sleep drive* D and is given mathematically by

$$D = \nu_{vh} H + \nu_{vc} C, \tag{3.1}$$

where homeostatic (H) and circadian (C) components are weighted by the constants ν_{vh} and ν_{vc}, respectively, which represent the connection strength of each drive to the VLPO. Note that, compared to Eq. (2.6), the subscript v is dropped throughout this chapter for simplicity. In this notation, developed in previous work [1], the first letter (v) refers to the VLPO and the second letter refers to either the homeostatic (h) or circadian (c) drive. A positive connection strength represents an excitatory input and a negative connection strength represents an inhibitory input. Therefore, ν_{vh} is positive (basal forebrain adenosine disinhibits the VLPO) and ν_{vc} is negative (the circadian signal C inhibits the VLPO). As illustrated in Fig. 3.1, the addition of the homeostatic component of the sleep drive $\nu_{vh}H$ and the circadian component $\nu_{vc}C$ gives the total sleep drive D. During wake, adenosine builds up in the basal forebrain (H increases), whilst during sleep it is cleared faster than it is produced (H decreases). As explained below, the oscillatory variation of D drives the system back and forth between sleep and wake.

The Phillips-Robinson model is represented schematically in Fig. 3.2. The model includes the mutual inhibition of the VLPO and MA populations and the homeostatic and circadian components of the sleep drive D to the VLPO. The mathematical equations governing the model's dynamics have been characterized in detail in Chapter 2 are summarized in Appendix 3.6. Its parameters are constrained from both physiology and behaviour [1, 81] and, despite its parameters being fitted to a small number of experiments, the model is able to predict the results of many protocols. The model predicts the average cell-body potentials relative to resting on the MA and VLPO neuronal populations: V_m and V_v, respectively. The variations of V_m and V_v are plotted in Figs 3.3(a) and (b), respectively. The average firing rates of these two populations, Q_m and Q_v,

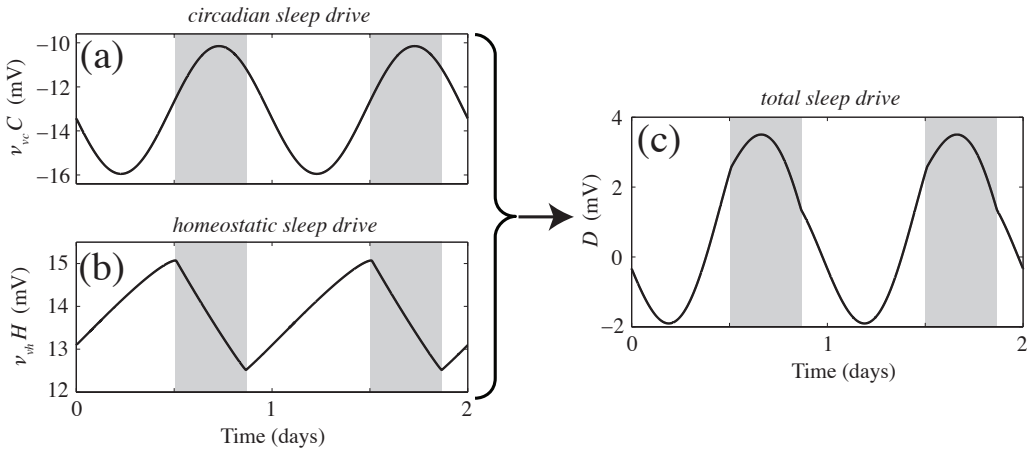

Figure 3.1: *Typical time evolution of (a) the circadian contribution to the sleep drive $\nu_{vc}C$ and (b) the homeostatic contribution $\nu_{vh}H$. These drives both act on the VLPO, giving the total sleep drive $D = \nu_{vh}H + \nu_{vc}C$, plotted in (c). Sleep periods are shaded.*

are given by sigmoidal functions of the potentials [82]. The sigmoidal function is plotted in Fig. 3.3(c), and the firing rates Q_m and Q_v in Figs 3.3(d) and (e), respectively. The model produces 'flip-flop' dynamics, exhibiting extended periods of wake and sleep, with rapid transitions between states. During wake, the MA is activated (V_m and Q_m are high) and the VLPO is suppressed (V_v is low and $Q_v \approx 0$). During sleep, the VLPO is active (V_v and Q_v are high) and the MA is suppressed (V_m is low and $Q_m \approx 0$).

3.2.2 Hysteresis, the Wake Ghost, and Wake-Effort

An important feature of the Phillips-Robinson model is the presence of *hysteresis* in V_m and V_v as a function of the sleep drive D, as shown in Fig. 3.4 for V_m. At low D, the system settles on the stable *wake branch*, and at high D, it settles on the stable *sleep branch*. As the sleep drive D oscillates between its minimum and maximum values [cf. Fig. 3.1(c)], the arousal state alternates

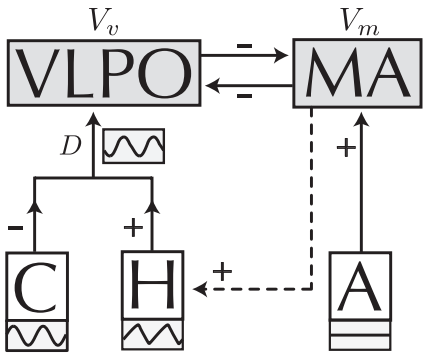

Figure 3.2: *Schematic of the Phillips-Robinson model of the sleep-wake switch [1]. The mutually inhibitory VLPO and MA populations form the core of the model. The circadian (C) and homeostatic (H) drives combine to form the sleep drive D to the VLPO, and the drive A is a constant, time-averaged input to the MA group. Excitatory ($+$) and inhibitory ($-$) interactions are represented by arrows and arousal state feedback from the MA to H is shown dashed. A schematic of the typical time evolution of each drive is displayed in a small rectangle: the 24* h *periodic sinusoidal C, the exponential rise and decay of H, and the constant drive A.*

between wake and sleep, accordingly. The model exhibits hysteresis: the wake to sleep transition (at $D \approx 2.5\,\mathrm{mV}$) occurs at a higher D than the sleep to wake transition (at $D \approx 1.5\,\mathrm{mV}$).

At high D ($> 2.5\,\mathrm{mV}$) when the stable wake branch no longer exists, a near-stable *wake ghost* state exists (this terminology is derived from nonlinear dynamics theory [121]). Ordinarily, as D increases past the normal wake-sleep transition (at $D \approx 2.5\,\mathrm{mV}$), the system drops from the stable wake branch to the stable sleep branch. However, an additional *wake-effort* drive, W, can be applied to instead hold the system in the wake ghost, keeping it awake. The wake ghost is distinguished from other regions at high D by its near-stability, requiring only a small additional drive W to remain in. The physiological origin of such a drive could be from orexinergic or cortical input to the MA group [146–148], and so we therefore model W as afferent to the MA. Interpreted within the hysteresis picture of Fig. 3.4, wakefulness is maintained *not*

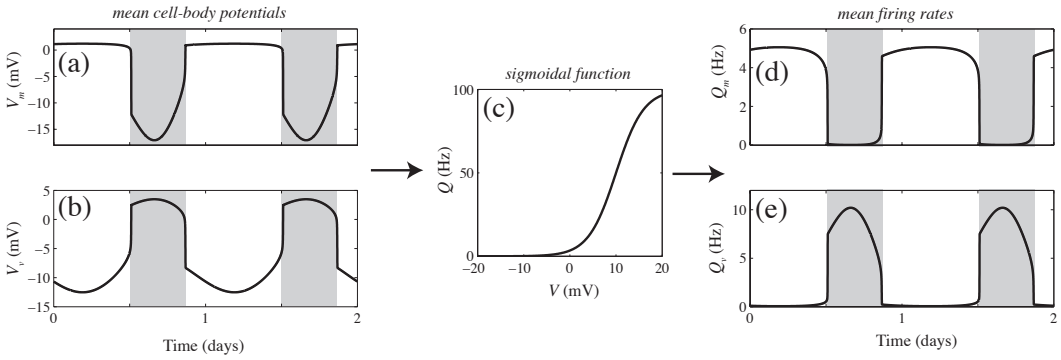

Figure 3.3: *Model output as a time series. Average cell-body potentials as a function of time are plotted for (a) the MA, V_m, and (b) the VLPO, V_v. A sigmoidal function, shown in (c), is used to transform the mean cell-body potentials to mean firing rates for (d) the MA, Q_m, and (e) the VLPO, Q_v. Sleep periods are shaded.*

by directly counteracting the growing 'horizontal' sleep drive D, but by compensating for it through the exertion of 'vertical' wake-effort W. The W drive instead compensates for it by 'pushing upwards' on the system, preventing it from dropping to the stable sleep branch. The amount of wake-effort required to maintain the system in the wake ghost increases with D, as the representative wake-effort arrows in Fig. 3.4 illustrate.

We emphasize that the wake and sleep ghosts are *not* constructions added to the model; they stem directly from the mathematics of the 'flip-flop' structure, the details of which can be found in Chapter 2 of this thesis, and are summarized in Appendix 3.7. The sleep ghost, which is associated with the termination of the sleep branch (i.e., at $D \approx 1\,\mathrm{mV}$) is not shown in Fig. 3.4 because it is much less pronounced than the wake ghost and is not directly relevant to the current work.

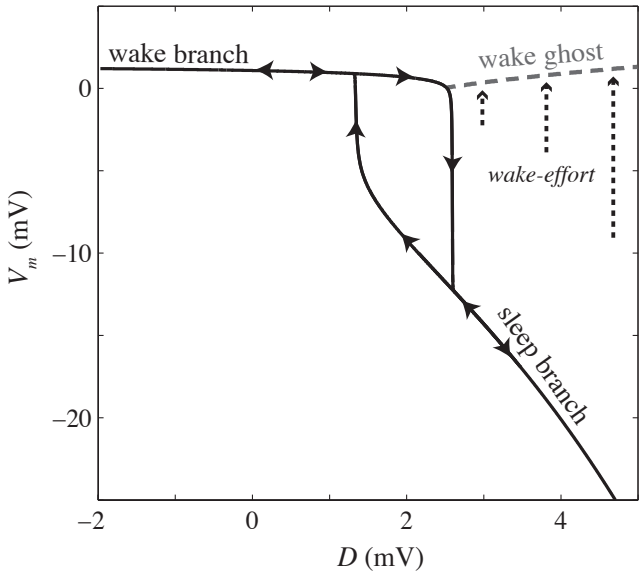

Figure 3.4: *The model's hysteresis loop for V_m as a function of the sleep drive D. It features a wake branch at low D, a sleep branch at high D, and an intermediate region in which both wake and sleep states exist simultaneously. As D oscillates with a* 24 h *period, the arousal state alternates between wake and sleep accordingly (indicated with arrowheads). The wake ghost (dashed line) is a near-stable waking state that persists through to high D. To maintain the system at the wake ghost, an amount of external wake-effort, W, is required, as illustrated using three representative dotted arrows. The length of the arrows indicates the required wake-effort magnitude, which increases with D.*

3.3 Total Sleep Deprivation

In this section we describe a method for simulating total sleep deprivation within the Phillips-Robinson model that involves exerting wake-effort to maintain the system in the wake ghost during normal sleep periods. The sleep deprivation method is introduced in Sec. 3.3.1, and its characteristic output is discussed in Sec. 3.3.2. In Sec. 3.3.3, we demonstrate quantitative agreement between the nominal W variation and an experimental data set containing subjective 'effort' required to maintain arousal (on a scale from "normal" to "considerable") and 'feeling' (on a scale from "very fresh" to "very tired") measures during sleep deprivation. Sensitivities of the W variations to changes in the model's drive parameters are investigated in Sec. 3.3.4.

3.3.1 Methodology and Rationale

We model total sleep deprivation by applying the W drive to the MA to maintain the system in the wake ghost during normal sleep periods. The system remains awake, moving between the stable wake branch at low D where no wake-effort ($W = 0$) is required, to the near-stable wake ghost at high D, where wake-effort must be applied.

We propose that the exertion of this additional wake-effort at high D constitutes a detriment to a subject's normal cognitive function. This may be because the need to apply wake-effort amounts to a persistent distraction that disturbs normal cortical function. Alternatively, assuming that one has some maximum capacity for performance [152], the need to exert W may represent a diminishment of this usual capacity. Whatever the exact mechanism, the above argument suggests that W should correlate with performance detriment, subjective fatigue, and other related measures. We therefore hypothesize a correlation between the model's wake-effort, a quantity with a direct physiological interpretation (an excitatory input to the MA) and psychological quantities that can be measured clinically. Since W increases with D (c.f., the represen-

tative arrows in Fig. 3.4), this hypothesis accords with the intuitive experience of finding it increasingly difficult to remain awake at high sleep pressure. In this scheme, $W = 0$ (i.e., at low D, on the wake branch) corresponds to no additional psychological effort to remain awake, and hence baseline performance. Quantitative correlations to data obtained during sleep deprivation protocols are investigated in the following section.

3.3.2 Characteristic Output

During sleep deprivation, the sleep drive $D = \nu_{vc}C + \nu_{vh}H$ varies with an increasing homeostatic component $\nu_{vh}H$ (H increases because the system is always awake) and an oscillatory circadian component $\nu_{vc}C$, as plotted in Fig. 3.5(a). The wake-effort is zero on the stable wake branch at low sleep drives $D < 2.5\,\mathrm{mV}$, and increases with D thereafter in the wake ghost. The relationship is plotted in Fig. 3.5(b) and allows the W variation to be inferred from that of D.

We note a number of important characteristics of the wake-effort variation plotted in Fig. 3.5(c). After the first night of total sleep deprivation, the W returns to zero as the system returns to the wake branch, as labeled 'B' in Fig. 3.5. Under the hypothesized link between wake-effort and psychological fatigue described above, the model predicts a return to baseline levels of subjective fatigue-related measures after the first night of sleep deprivation. Thereafter, as the homeostatic component of the sleep drive continues to grow, even at the local minima of D, the system does not again return to the wake branch and hence W does not return to zero. The W curve in Fig. 3.5(b) becomes shallower as D increases. Thus at high D, changes in D produce smaller changes in W; i.e., the same oscillation amplitude in D results in smaller wake-effort oscillations. Therefore, since D increases with time, the model predicts a decrease in the W oscillation amplitude with time spent awake. Since H asymptotes to a maximum value with time, the mean value of D will also ap-

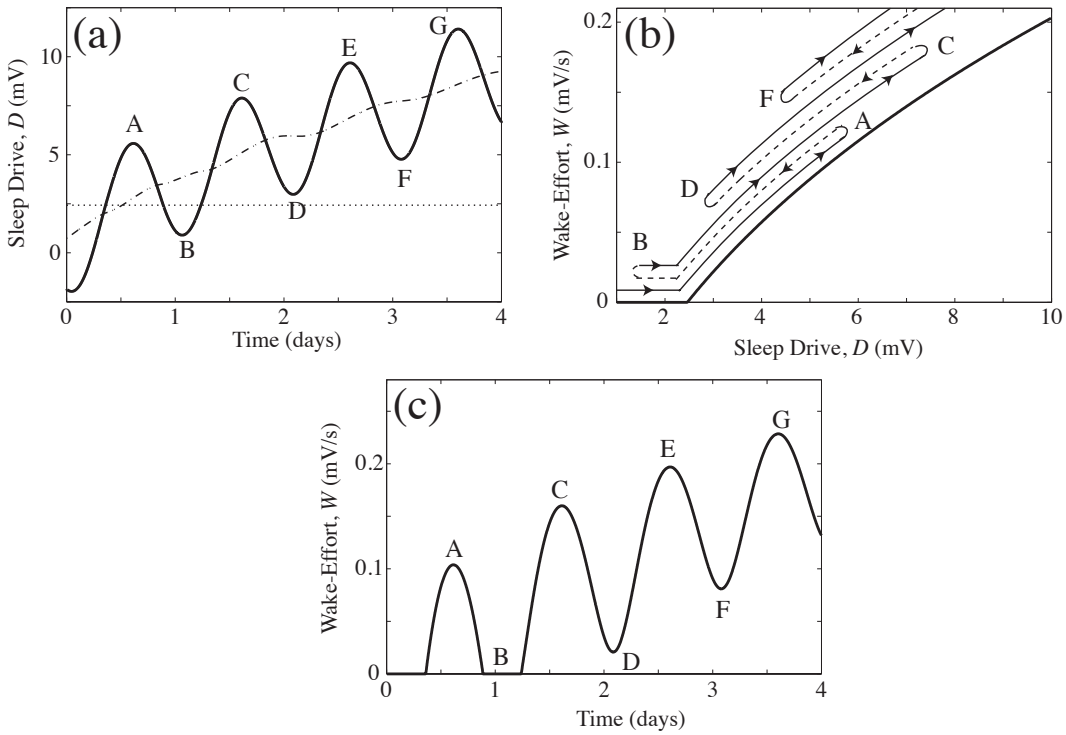

Figure 3.5: *Model dynamics across four days of total sleep deprivation. (a) Sleep drive D (solid line) includes increasing homeostatic (dot-dashed line) and oscillatory circadian components. The line $D = 2.5\,\mathrm{mV}$ (corresponding to the normal wake–sleep transition) is shown dotted: for $D < 2.5\,\mathrm{mV}$ the system is on the wake branch and $W = 0$. (b) Wake-effort, W required to remain awake as a function of the sleep drive D. This is zero for $D < 2.5\,\mathrm{mV}$ and increases approximately quadratically thereafter. The trajectory back and forth along this curve corresponds to the D variation shown in (a), as indicated by arrows. This trajectory indicates the position on the adjacent curve; the vertical shift with each oscillation is for clarity. (c) Wake-effort, W time series. The sleep drive variation in (a) should be considered to control the oscillation back and forth in (b), which gives rise to the W variation in (c). Points A–G are labeled in (a)–(c) to demonstrate the relationship between each of the subplots.*

proach a maximum value. Therefore, the decreasing oscillation amplitude of D will approach a constant value with time.

3.3.3 Connections to Fatigue-Related Measures

As proposed in Sec. 3.3.1, we expect a correlation between the model's W drive and subjective fatigue-related measures. Indeed, the W time series shown in Fig. 3.5(c) qualitatively replicates the clinical variation for a number of subjective measures, including 'fatigue' [149, 150, 153, 154], 'sleepiness' [153, 154], 'mood' [153, 154], 'feeling' [12], and 'alertness' [13]. Data reported by Pasnau *et al.* [12] includes the variation in subjective 'effort' and 'feeling' of four male subjects over approximately seven days of total sleep deprivation. Subjects were required to indicate both subjective 'effort' and 'fatigue' on a 20 cm scale every six hours throughout the study. For 'effort', the phrases "normal" to "a considerable amount of additional effort" required to maintain arousal to a level that would enable them to do "as well as they could" at the given performance task at opposite ends of the scale. For the purposes of measuring 'fatigue', the five guiding phrases: "very tired," "tired," "as usual," "fresh," and "very fresh" were spaced evenly along the scale.

Using our model with nominal parameters, and fixing zero wake-effort to "normal" subjective effort and "fresh" feeling, we have one degree of freedom in the vertical scale factor of the respective Pasnau data sets, and another in adjusting the starting time of the model simulation. As shown in Fig. 3.6, there is good agreement with both data sets up to approximately five days of deprivation. Note that since error bars were unavailable in both sets of data, a rigorous comparison between the model and the data is not possible. However, the data points are joined with a solid line to guide the eye, and in the following we compare the positions of the data points and the trends between them. The 'effort' data matches the model's characteristic return to baseline ("normal") levels of effort after the first night of sleep deprivation. Furthermore, both

data sets exhibit a decreasing oscillation amplitude with time, matching the model's prediction. After ~ 5 days, while the model still predicts the approximate positions of the peaks and troughs of the experimental variation, the data deviate below the model's prediction, due to a "fifth day fatigue turning point" [12], perhaps due to end-of-study anticipation or habituation to high fatigue, effects that we have not attempted to model here. However, as will be elaborated upon in the discussion (Sec. 3.5), end-of-study anticipation would provide a boost in motivation, contributing to W through an orexinergic drive (since the activity of the orexin group is tied to motivational factors [161]) and hence decreasing the cortical contribution to W, decreasing subjective 'effort' and negative 'feeling'.

3.3.4 Dependence on Parameters

The parameters of the Phillips-Robinson model (listed in the Tab. 4.1 in Appendix 3.6) correspond to physiological variables, including the time-decay properties of neuromodulators, the strength of interactions between neuronal populations, and the connection strengths of the circadian and homeostatic drives to the VLPO [1]. By studying the sensitivities of the W time series curves to changes in model parameters, the impact of the corresponding physiological changes can be inferred. In the following, we focus on the drive parameters which control the time evolution of D and hence control the dynamics back and forth around the model's hysteresis loop (shown in Fig. 3.4). In particular, we investigate the effect of changing the initial (i.e., prior to the onset of the sleep deprivation protocol) homeostatic sleep pressure H_{init}, as well as the homeostatic and circadian connections to the VLPO, ν_{vh} and ν_{vc}, respectively. Relative to normal, the initial homeostatic sleep pressure H_{init} could be increased or decreased, due to a previously-accumulated sleep debt or increased restfulness prior to the clinical study, respectively. Changes in ν_{vh} and ν_{vc} may correspond to inter-individual differences in metabolism or

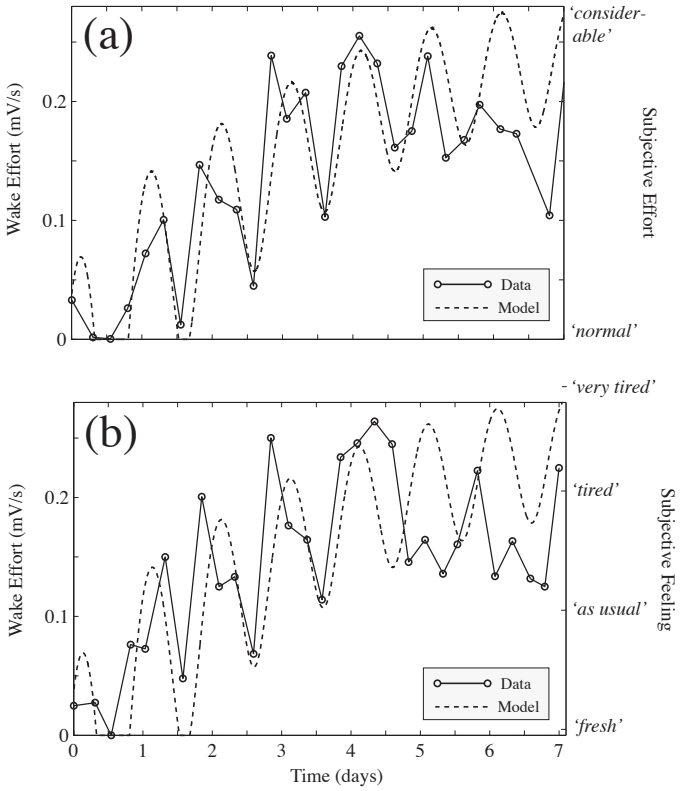

Figure 3.6: *Comparison of the model's W drive with clinical data reported by Pasnau et al. [12]. (a) The variation of subjective 'effort' (on a scale from "normal" to "considerable"). (b) The variation of subjective 'feeling' (on a scale from "very fresh" to "very tired"). In each case, the data are plotted using circles and a solid line and the model's prediction using nominal parameters is plotted using a dashed line.*

circadian amplitude, respectively. Alternatively, they may reflect differences in the neuronal connection strengths themselves. The effect of changing the nominal magnitude of each parameter by $\pm 30\%$ on both the D and W time series are shown in Fig. 3.7. The upper plots [Figs 3.7(a), (c), and (e)] show the sleep drive D time series; the lower plots [Figs 3.7(b), (d), and (f)] show the wake-effort W time series. The relationship between D and W is given by the function plotted in Fig. 3.5(b). Since changes in ν_{vh} and ν_{vc} affect the model's dynamics, D has been offset by a constant in each case to compensate for this parameter change, so as to maintain the model's normal sleep length at its nominal value of 8.5 h.

Changes to H_{init} cause the D time series to differ initially, as shown in Figs 3.7(a) and (b). However, the curves all approach the same nominal variation as H saturates with time. As shown in Fig. 3.7(b), the W variation exhibits the same characteristics. A 30% decrease in H_{init} delays the need for wake-effort until the second deprivation night, whereas a 30% increase eliminates the return to baseline ($W = 0$) entirely.

Changes in ν_{vh} affect the rate at which H, and hence D, increase, as shown in Fig 3.7(c). Decreasing ν_{vh} slows the rate of increase of D and hence that of the W curves, which rise more gradually to lower mean levels, as shown in Fig. 3.7(d). Increasing ν_{vh}, on the other hand, causes the D and W curves to rise more rapidly and to higher mean levels. The curvature of the D–W function plotted in Fig. 3.5(b) implies that the mean wake-effort oscillation amplitude decreases with D. Since ν_{vh} controls the rate of increase of the D and W time series, subjects with a decreased homeostatic sensitivity (i.e., a low ν_{vh}) will exhibit greater wake-effort oscillations at lower mean wake-effort compared to the normal. The opposite applies to subjects with a greater homeostatic connection strength ν_{vh}.

Increasing ν_{vc} increases the oscillation amplitude of the sleep drive D, a change that is also apparent in the W variation, as plotted in Figs 3.7(e) and (f). While the D and W maxima remain approximately unchanged, the minima

are shifted to a higher or lower W relative to normal, for a lower or higher ν_{vc}, respectively.

The results presented in this section relate changes in fatigue variation to changes in underlying physiological processes – the circadian and homeostatic drives. They represent general predictions of the sleep model that await clinical confirmation. In principle, each of the predicted variations could be tested experimentally, by comparing the response of different groups of subjects to sleep deprivation in a clinical trial. The initial homeostatic sleep pressure H_{init} could be distinguished by comparing a group of sleep deprived subjects to controls. The strength of the homeostatic drive ν_{vh} could be inferred from the dynamics of EEG slow-wave activity (SWA) amongst subjects, and the circadian amplitude ν_{vc} could be inferred from the body temperature [4] or catecholamine excretion [162] variation, forming an analytic basis for discriminating between responses to sleep deprivation. A clinical validation of the trends proposed here may help to explain inter-individual differences in fatigue dynamics, and would facilitate direct mapping between clinical results and the model's parameters. The realization of such a goal would enable the model to be calibrated to the sleep patterns of individuals.

3.4 Comparison with Data

In this section, we compare the model's predictions with two 72 h sleep deprivation data sets obtained from (i) 29 male officers and corporals, reported by Fröberg *et al.* [150], and (ii) 15 female subjects from a voluntary military association, reported by Åkerstedt *et al.* [149]. The latter study aimed to replicate the former except using female subjects. We seek linear relationships between the model's variables and clinical measures, as a means of quantifying possible correlations. The numerical values for the linear fits in this section are given in Appendix 3.8.

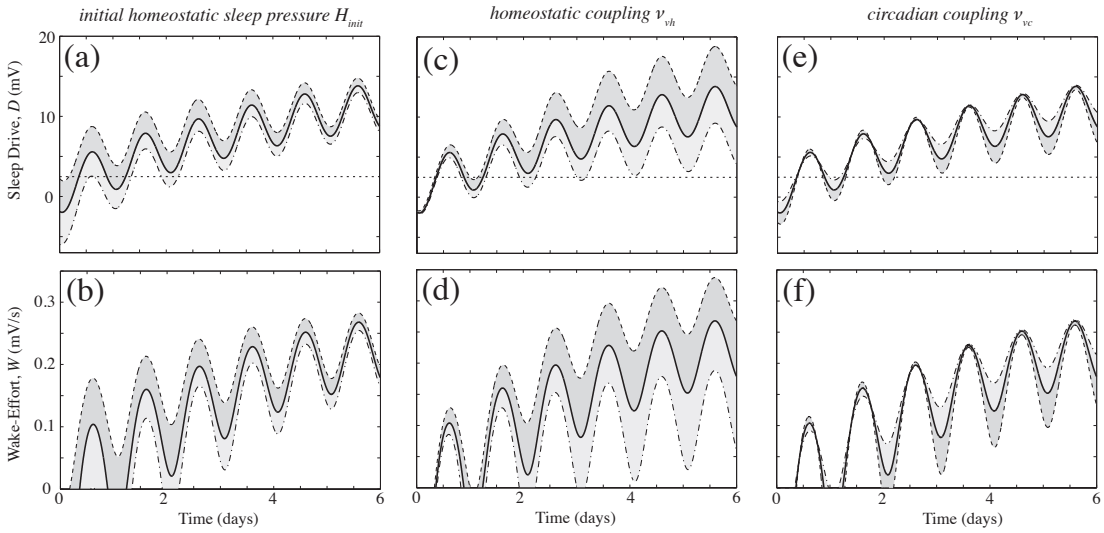

Figure 3.7: *Sensitivities of the model's sleep drive D and wake-effort W curves to parameter changes. The nominal curve (solid line) is compared to a case with a 30% increase in magnitude of the relevant parameter (dashed line and dark shading) and one with a 30% decrease in magnitude of the relevant parameter (dot-dashed line and light shading). Time series for D are plotted in the upper plots (a), (c), and (e), and for W in the lower plots (b), (d), and (f); for: (a), (b) the initial homeostatic sleep pressure $H_{\rm init}$, (c), (d) the connection strength of the homeostatic drive to the VLPO, $|\nu_{vh}|$, and (e), (f) the connection strength of the circadian drive to the VLPO, $|\nu_{vc}|$. The transformation between the D and W curves is plotted in Fig. 3.5(b). The drive corresponding to the end of the wake branch ($D \approx 2.5\,\mathrm{mV}$) is indicated with a dotted line in the upper plots – below this threshold the system is on the wake branch and $W = 0$.*

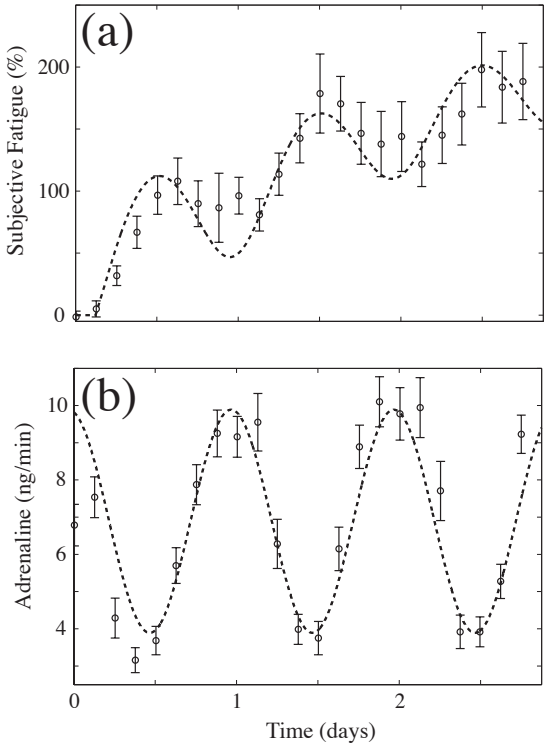

Figure 3.8: *The model's simulation of data adapted from a* 72 h *sleep deprivation study of female subjects, as reported by Fröberg et al. [150]. The data (circles and solid line) and the model prediction (dashed line) are shown for: (a) Percentage increase in subjective fatigue relative to baseline (0%) and (b) Adrenaline production. The subjective fatigue data set is reproduced by the model's W drive using a decreased circadian connection strength $|\nu_{vc}|$ and an increased H_{init}, and the adrenaline data set has been fitted to the model's circadian drive C.*

The sleep deprivation study using male subjects [150] found a variation in subjective fatigue qualitatively similar to the W variation of our model and an approximately sinusoidal variation in adrenaline secretion. We fit our circadian drive C to the adrenaline data and the W drive to the subjective fatigue data. Although there may be a phase shift between the circadian signal C and the circadian variation of adrenaline secretion, we are able to achieve a good fit to the data without using an additional phase shift, thereby reducing the number of fitting parameters by one. As shown in Fig. 3.8, the fit to the adrenaline excretion exhibits good agreement with the sinusoidal C. Qualitatively, the W data shown in Fig. 3.8(a) exhibit a variation similar to the effect of increasing H_{init}, as shown in Fig. 3.7(a), but with a significantly smaller circadian oscillation. We achieve a good fit to the data by increasing H_{init} by 10% and decreasing $|\nu_{vc}|$ by 35% relative to their nominal values, as shown with a dashed line in Fig. 3.8(a). Baseline fatigue is fixed to zero wake-effort, the simulation starting time is constrained to that used for the adrenaline data, and we have a single degree of freedom in adjusting the vertical scale.

The sleep deprivation study using female subjects [149] measured subjective fatigue, adrenaline excretion, and body temperature. The three data sets are plotted in Figs 3.9(a), (b), and (c), respectively. In contrast to the male subjects, the rate of increase of fatigue is markedly lower for the female subjects in this data set, returning to near baseline levels every 24 h. As explained in Sec. 3.3.4, this suggests a decreased homeostatic component to the sleep drive; a decrease in ν_{vh}. To simulate the fatigue data, we increase H_{init} by 10% as for the above fitting, and decrease ν_{vh} by 30% relative to its nominal value. The model's predicted W variation for these parameters, using the same vertical scaling as for the Fröberg study, is shown in Fig. 3.9(a). In Sec. 2.5.3, we reported good linear agreement between body temperature and our sleep drive D for a simulation of the arousal threshold in a sleep fragmentation study, in which the two quantities were found to correlate negatively. Linear fits of C

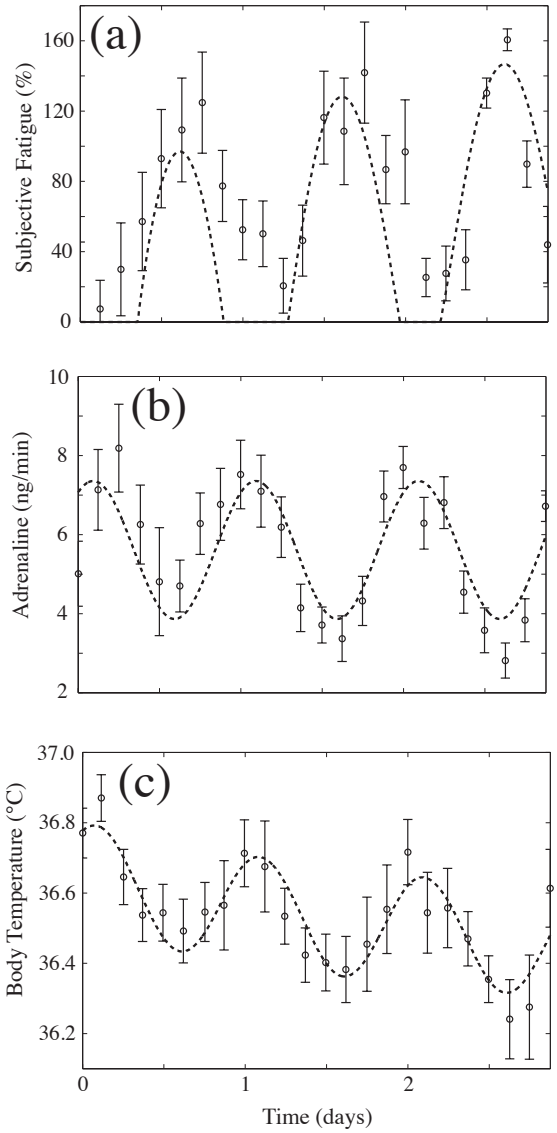

Figure 3.9: *The model's simulation of data adapted from a* 72 h *sleep deprivation study of male subjects, as reported by Åkerstedt et al. [149]. The data (circles and solid line) and the model prediction (dashed line) are shown for: (a) Subjective fatigue relative to baseline (%), (b) adrenaline production* (ng/min)*, and (c) body temperature* (°C)*. The model's W drive correlates positively with fatigue, the circadian drive C correlates positively with adrenaline, and the sleep drive D correlates negatively with body temperature. A reduction in the nominal value of ν_{vh} and an increase in H_{init} have been used to reproduce the data.*

with adrenaline and D with body temperature show good agreement with the clinical data, as plotted in Figs 3.9(b) and (c), respectively. Therefore, the model is able to simultaneously predict the variation in subjective fatigue (inferred from W), adrenaline excretion (inferred from C), and body temperature (inferred from D).

3.5 Summary and Discussion

3.5.1 Summary

In this chapter, we have elucidated a link between clinically-measurable psychological quantities and those from a physiologically-based model of the sleep-wake switch. The model exhibits hysteresis between sleep and wake and, crucial to this work, a near-stable waking state: the wake ghost, at high values of the model's sleep drive D. Physiologically, cortical or orexinergic input to the MA is expected to maintain wakefulness during sleep deprivation [146–148]. We correspondingly applied compensatory wake-effort W as a drive to the MA to maintain the system in the wake ghost during normal sleep periods. Sleep deprivation was simulated by holding the system in a waking state – on the wake branch at low D and in the wake ghost at high D. The W variation correlated with subjective 'effort' required to maintain arousal for performance in a given task, and similar quantities including 'feeling' and 'fatigue'. By investigating the dependence of the W time series on the model's drive parameters, changes in their topology were related to their underlying causes. Such parameter changes may account for differences in self-ratings of fatigue between the male and female subjects during 72 h of sleep deprivation. In addition to fatigue-related measures inferred from the model's W quantity, the model can simultaneously reproduce the circadian variation of adrenaline excretion and body temperature, as inferred from the model's circadian drive C and sleep drive D, respectively.

3.5.2 Towards a Unification of Clinical Measures

A key idea that stems from the current formulation is the two-dimensional nature of drives to the system, as interpreted within the hysteresis representation of the model. In the first dimension, the sleep drive D combines the circadian and homeostatic components as a total drive to the VLPO, controlling the 'horizontal' movement back and forth along the hysteresis loop. Rather than compensating for the sleep drive D by directly opposing it, the 'vertical' W drive is instead applied to the MA groups to maintain wakefulness. The existence of this second independent compensatory drive is consistent with Eysenck's two postulated types of arousal [163]: a primary arousal system affected by sleep deprivation and circadian oscillations (much like our sleep drive D) and a second compensatory system that allocates additional effort and resources whenever the first arousal system is lowered (much like our wake-effort drive W).

The concept of subjects applying compensatory 'effort' to maintain performance standards is an intuitive one and has been reported previously in numerous clinical analyses [12, 14, 71, 164–166]. A major advance achieved in this chapter has been the theoretical framing of the concept, which has been linked to a drive to the MA: the W drive. The model clearly delineates the contribution of the homeostatic and circadian components to the model's sleep drive D and the corresponding amount of wake-effort required to maintain arousal. We emphasize that the wake ghost, that can be made stable with the W drive, is not artificially introduced into the model, but is a direct consequence of the existence of two mutually inhibitory populations: the MA and VLPO (c.f., Chapter 2). The W variation has been quantitatively linked to both subjective 'effort' [c.f., Fig. 3.6(a)] and subjective fatigue [c.f., Figs 3.6(b), 3.8, and 3.9] in this chapter. The same variation is present in a diverse number of measures including 'attention', 'feeling', 'alertness', and 'sleepiness'. The model framework proposed here represents a significant step toward unify-

ing a vast range of existing clinical descriptors onto a single, quantitative scale: in terms of our model's sleep drive D and wake-effort W quantities.

3.5.3 Towards a Performance Model

In this section we propose a system for interpreting objective performance within our model. During sleep deprivation, we have demonstrated how wake-effort is needed to maintain arousal at or above some minimum, baseline level required to perform a given task. Contributions to the W drive come from both cortical and orexinergic projections. We propose that the cortical component of this drive detracts from to performance standards, as it diverts cortical effort from being applied to a given task to the role of simply maintaining arousal. The orexinergic contribution is enhanced by motivational input [100], which increases the excitatory drive to the MA, decreasing that which must be applied cortically, and hence raising performance levels. Differences between tasks stem from their differing interest to the subject, and hence different orexinergic contributions to the MA. When a sleep deprivation subject's motivation is high, the additional cortical drive required to meet the required arousal level is reduced, due to the increased orexinergic input. Catastrophic lapses occur when subjects do not apply the necessary effort, causing the system to fall rapidly toward the sleep branch, dropping to low arousal or triggering a microsleep.

Evidently W will give an indication of the performance detriment, however, the relationship is both nonlinear and task-specific. For example, a very simple task such as remembering a single numerical digit, would yield positive results except when the subject has a microsleep or indeed falls asleep – a clearly non-linear relationship. The next step in this line of modeling is to quantitatively model tasks of differing complexity and compare the wake-effort and the performance detriment to clinical performance data. The ability to quantitatively predict the occurrence of performance lapses (i.e., drops toward the stable sleep branch) would facilitate future applications to shift work protocols, for exam-

ple, with significant implications for both safety and performance efficiency. This may be done in the future by introducing noise into the model.

That a subject's motivation to perform a task proficiently is linked to their ability to apply effort and maintain sufficient arousal and that differences in motivation imply differences in performance variation under sleep deprivation are established clinical notions [71]. In the performance model described above, we have quantitatively related these concepts to their postulated physiological causes. For example, O'Hanlon [166] describes subjects that "must exert effort to maintain [their] arousal setpoint at the task-optimal level." Harrison and Horne [71] note that subjects are more likely to apply effort to complex tasks that evoke increased interest, but require motivational incentives to apply the same effort to monotonous tasks. Furthermore, May and Kline [167] proposed that "when arousal dips below some critical level for a particular cognitive function, a catastrophic failure in the performance of that function occurs. Different functions require specific amounts of attention [i.e., W] and hence would be affected by varying degrees of de-arousal." Finally, Mikulincer *et al.* [152] refer to the "amount of available 'resources' subjects can apply to a task" and propose the existence of a common underlying resource-limiting factor that affects each of the resulting subjective measures during sleep deprivation. They propose that "the increase in sleepiness, negative mood, cognitive difficulties, and waking dreams, and the decrease of motivation and positive mood [...] are all manifestations of a decline in resource-limiting factors [i.e., the cortical contribution to W] during sleep deprivation." All of these clinical conclusions fit with our postulated performance model.

3.5.4 Clinical and Modeling Implications

Our finding that the circadian oscillation amplitude in the W variation decreases with increasing D (i.e., with continuing sleep deprivation), is apparently contrary to certain clinical studies that instead note an increase in subjective

fatigue-related measures [152, 168, 169]. Mikulincer *et al.* [152], for example, observed that "the rhythmic component has a more marked effect on the subjective measures as sleep loss increases", the opposite to our general finding. In one clinical study [152], the circadian amplitude on the second day was increased relative to the first, but was similar between the second and third days for most measures. That the circadian variation remained steady on the third day (rather than increasing) was attributed to an end-of-study anticipation effect, increasing subjects' motivation. Our analysis suggests an alternative explanation: the return to the wake branch after the first night of sleep deprivation suppresses the full circadian variation of W. Hence the W oscillation amplitude (and that of associated fatigue-related measures) can appear to increase on the second night relative to the first [c.f., Fig. 3.5(c)]. After the second night, the model predicts a steady decrease in the oscillation amplitude. Although the subjective measures reported in these studies do not return to near-baseline levels after the first night, instead continuing to increase, we argue that this is due to additional psychological effects of prolonged adherence to the experimental protocol, which would presumably be monotonic. Thus, our model predicts that obtaining circadian information from sleep deprivation studies of three days or less can be misleading due to the return to near baseline ($W = 0$) after the first night of total sleep deprivation.

The combination of increasing and oscillating components that characterize the qualitative variation of subjective fatigue-related measures has previously been reproduced using the 'two-process' model, in which the difference between Process S and the upper circadian threshold was taken to indicate fatigue [57]. However, as the two-process model is phenomenological in nature, it can offer only a qualitative interpretation of this mechanism: the more the homeostatic sleep pressure increases above the maximum circadian limit, the greater the fatigue a subject can be expected to experience. It also offers no explanation of how or why the system is allowed to exceed the upper circadian threshold, where it usually falls asleep. Within a physiologically-based model, however,

a possible source of the fatigue is elucidated – a necessary drive to the MA that 'diverts' cortical effort from being exerted on general performance. The predictions of the current model differ from those of the two-process model in the precise shape of the fatigue curves themselves, the nominal return to baseline after one full night of sleep deprivation, and the decreasing oscillation amplitude with time thereafter.

3.5.5 Sex-Related Differences

The simulation of two sleep deprivation studies using male and female subjects performed in Sec. 3.4 used a reduction in the circadian connection strength $|\nu_{vc}|$ to reproduce the male data set, and a reduction in the homeostatic connection strength $|\nu_{vh}|$ for the female data set. Taken at face value, the analysis therefore suggests a significant sex-related difference in the circadian and homeostatic control of sleep. In particular, the amplitude of the circadian signal may be lower for male subjects than for females and the homeostatic impact of sleep deprivation may dominate the male response, being less significant for females. Sex hormones are known to influence the SCN [170, 171], giving rise to modest sex-related differences in circadian rhythms. Circadian rhythms also depend on the phase of the female menstrual cycle [172] (an effect addressed in the female sleep deprivation study [149] by using subjects with an even distribution of menstrual phases). The homeostatic sleep drive, as inferred from SWA in the human EEG, is also similar between the sexes [173]. Since the homeostatic and circadian drives appear to be similar between the sexes, there are a number of interpretations that may justify our use of changes in ν_{vh} and ν_{vc} to simulate the differences between the male and female data sets. First, we note that the circadian signal from the SCN is measured indirectly, from secondary quantities such as variation in body temperature or catecholamine excretion [162]. One study found no difference in temperature rhythms between the sexes, but differences in the sleep-wake properties [174], suggesting that the connectivities

ν_{vc} and ν_{vh} may differ between the sexes. Alternatively, since the data are of subjective measures, the parameter changes may instead reflect sex-related psychological differences in the self-rating of fatigue, with the two sexes displaying different self-assessed reactions to the underlying circadian and homeostatic dynamics. However, due to the inherent degree of uncertainty associated with subjective measures, it is likely that the study conditions dominate the differences between the two data sets, with sex-related differences making only a minor contribution. In addition, we have focused here only on the drive parameters of the model – sex-related differences in other physiological properties and hence other model parameters would also affect the W and subjective fatigue time series. It is therefore impossible to extract definitive conclusions from the results of this analysis – further experimentation is required to provide evidence for or against the above hypotheses.

3.5.6 Future Work and Conclusions

The framework developed here has the potential to incorporate specific external stimuli that may aid in the maintenance of wakefulness. External sensory stimuli, for example, drive the MA populations [118, 127, 128], perhaps via the orexin group [129, 130] or from acetylcholine-related inputs [131, 132]. They are therefore identified as a 'vertical' drive in the hysteresis picture, acting to increase V_m. By quantifying the relationship between various external stimuli and their effect on the MA, as was done in Sec. 2.5 for auditory stimuli, the corresponding 'vertical' drive can be determined. This can then be used to infer the subsequent decrease in the necessary wake-effort, thus boosting performance and decreasing subjective fatigue. Caffeine, for example, is an antagonist of adenosine receptors [105, 114, 175, 176], which are present in both the VLPO and acetylcholine-related nuclei [105, 119]. As a performance-enhancing pharmaceutical, therefore, it may act as both a 'horizontal' drive, counteracting D directly (through a decrease in the effective H), and as a

'vertical' drive, compensating for the high D (from increased acetylcholine-related and hence MA activity). Through physiologically-based modeling, a diverse range of stimuli, including sensory and pharmaceutical influences can be understood on a common scale and, in the context of the present work, can be compared for their effectiveness in reducing fatigue during sleep deprivation. In future work, it is hoped that the W time series, as modulated by various external stimuli, can be compared for the purpose of maximizing safety and productivity of shift workers, for example.

Sleep deprivation has previously been simulated using the model by holding V_m at a constant waking value [81]. However, the dynamic analysis of Chapter 2 suggests that the wake ghost represents the waking state at high D. The current method also allows the W variation to be deduced, a feature that will be crucial for simulating fatigue with the model. The previous study of sleep deprivation using the Phillips-Robinson model [81] did not consider the variation of wake-effort or fatigue during the sleep-deprivation period, but instead focused on the sleep deprivation recovery process, predicting optimum recovery schedules and reproducing experimental sleep latencies resulting from such protocols. In future work, we will use the W drive to quantify the performance and mood detriment during recovery from sleep deprivation.

The main advantage of our approach is the use of mathematical language to quantitatively relate neuronal interactions to measurable behavioral and psychological quantities. The underlying framework of the model is based on physiology, so physiological studies can be used to provide evidence for or against the model's predictions. This quality is distinct from phenomenological models which fit the data but provide only limited insights into the underlying physiological dynamics that give rise to the observed patterns. Although arousal-state dynamics are controlled by a complicated set of neuronal interactions throughout the brain, we have simplified the dynamics by averaging over dynamic inputs from orexin, acetylcholine-related neuronal populations, and the cortex, facilitating an intuitive understanding of the dynamics while including enough

of the relevant physiology to simulate clinical data. Dynamic versions of the drives listed above would modulate the arousal state within sleep and wake, and will be explored in a future version of the model. Indeed, the success of the simple physiologically-based model used in this chapter demonstrates the potential of neuronal population modeling to aid the understanding of sleep-wake dynamics and guide clinical studies.

3.6 Appendix A: The Phillips-Robinson Model

The Phillips-Robinson neuronal population model of the sleep-wake switch has been described in detail elsewhere [1, 81]; here we summarize its governing equations. Each population $j = m, v$, where m represents the MA and v represents the VLPO, has a mean cell-body potential $V_j(t)$ relative to resting and a mean firing rate $Q_j(t)$, which is approximated as a sigmoidal function of V_j:

$$Q_j = S(V_j) = \frac{Q_{\max}}{1 + \exp[-(V_j - \theta)/\sigma']}, \tag{3.2}$$

where $Q_{\max}$ is the maximum possible firing rate, θ is the mean firing threshold relative to resting, and $\sigma'\pi/\sqrt{3}$ is its standard deviation [84]. Neuronal dynamics are represented by

$$\tau_v \dot{V}_v + V_v = \nu_{vm} Q_m + D_v, \tag{3.3}$$

$$\tau_m \dot{V}_m + V_m = \nu_{mv} Q_v + D_m, \tag{3.4}$$

where the ν_{jk} weight the input from population k to j, τ_j is the decay time for the neuromodulator expressed by group j, and D_j represents the external drive to population j.

For normal dynamics, the drive $D_m = A$ is averaged to a constant. Throughout this chapter, nominal input to the VLPO, D_v, is referred to as the 'sleep

drive' and is written simply as D:

$$D = \nu_{vh} H + \nu_{vc} C, \tag{3.5}$$

which includes homeostatic H and circadian C components. The circadian drive is a 24 h periodic sinusoidal function of time

$$C(t) = \sin\left[\omega(t - \alpha)\right] + c_0, \tag{3.6}$$

where $\omega = (2\pi/24)\,\mathrm{h}^{-1}$, c_0 is a constant offset, and α is the initial phase angle. The parameter α effectively sets the starting time of the model simulation, which varies between different sleep deprivation protocols. The homeostatic sleep drive is represented by the adenosine concentration H, which is governed by

$$\chi \dot{H} + H = \mu \frac{Q_m^2}{\eta_h + Q_m^2}, \tag{3.7}$$

where χ is the characteristic time for somnogen clearance, and μ and η_h are constants. The saturating form of the source term on the RHS of Eq. (3.7) differs from previous versions of the model that approximated metabolism as a linear function of Q_m. The saturating form is necessary to decrease the unrealistically high production at high Q_m, as occurs during sleep deprivation (in the wake ghost at high D). The results presented in this chapter are not sensitive to the precise value of η_h, since for normal dynamics, intermediate Q_m are encountered only in transitions between sleep and wake: as long as the source term saturates at high Q_m, μ can be chosen to reproduce the normal sleep length, whence this new form Eq. (3.7) will yield quantitatively similar results. The original Phillips-Robinson model [1, 81], which is sensitive only to the waking and sleeping values of the source term, is also unaffected by the change to the new form of Eq. (3.7). Other model parameters have been constrained by both dynamics and physiology to produce realistic sleep-wake

Table 3.1: *Nominal model parameter values obtained from [81], except for the new saturation parameter η_h and source magnitude μ.*

Parameter	Value	Parameter	Value	Parameter	Value
$Q_{\max}$	$100\,\mathrm{s}^{-1}$	ν_{vm}	$-2.1\,\mathrm{mV\,s}$	c_0	4.5
θ	$10\,\mathrm{mV}$	ν_{mv}	$-1.8\,\mathrm{mV\,s}$	χ	$45\,\mathrm{h}$
σ'	$3\,\mathrm{mV}$	ν_{vh}	$1\,\mathrm{mV\,nM}^{-1}$	μ	$28.4\,\mathrm{nM}$
A	$1.3\,\mathrm{mV}$	ν_{vc}	$-2.9\,\mathrm{mV}$	η_h	7.9
τ_v	$10\,\mathrm{s}$	τ_m	$10\,\mathrm{s}$		

behavior in Refs [1, 81].

3.7 Appendix B: Sleep Deprivation Algorithm

As described in Sec. 2.3.4, the wake ghost is a remnant of the saddle-node bifurcation at which the stable wake node is annihilated. It is evident in the V_v–V_m plane as a region of low velocity $\dot{V} = (\dot{V}_v^2 + \dot{V}_m^2)^{1/2}$, causing trajectories to linger in it, forming a bottleneck [121]. In this chapter, we take the V_v and V_m values at the minimum $\dot{V}$ to represent the wake ghost state. However, since $\dot{V}_v \approx 0$ (an assumption used in the hysteresis picture), we can approximate $\dot{V} \approx \dot{V}_m$, and thus the local minimum of $\dot{V}_m$ approximates the position of the wake ghost. Since, in the absence of state changes, $\dot{V}_v \approx 0$, the $W(t)$ drive maintains the system as close as possible to the local minimum in $\dot{V}_m$. Ordinarily, $D_m = A$ is a constant, but during sleep deprivation, the wake-effort W enters as an additional time-dependent drive term to the MA. We can write

$$\dot{V}_m = \dot{V}_m^0 + W, \tag{3.8}$$

where the additional wake effort drive has been written out explicitly: $\dot{V}_m^0$ is given from Eq. (3.4) with $D_m = A$. The wake effort drive W is given the form

$$W = -\dot{V}_m^0 + \epsilon, \tag{3.9}$$

where ϵ is a variable. Thus W counteracts $\dot{V}_m^0$ so that $\dot{V}_m = \epsilon$. To determine $W(t)$ required to maintain the system in the wake ghost (and therefore using the *minimum* amount of effort), our algorithm uses

$$\frac{d}{dV_m}\dot{V}_m = -1 + \nu_{mv}\nu_{vm}S'\left[\nu_{vm}S(V_m) + D_v\right]S'(V_m), \tag{3.10}$$

which is zero near the wake ghost (when $V_m = \widetilde{V}_m$, say). Locally, this function is negative for $V_m < \widetilde{V}_m$ and positive for $V_m > \widetilde{V}_m$. Therefore, as long as ϵ is chosen to be the opposite sign of $d\dot{V}_m/dV_m$ [given by Eq. (3.10)], this algorithm keeps the system close to the wake ghost, yielding $\dot{V}_m = |\epsilon|$ when the system is below the wake ghost and $\dot{V}_m = -|\epsilon|$ when the system is above it. For the numerical implementation of the above algorithm used for simulations presented in this chapter, $|\epsilon| = 2 \times 10^{-4}\,\mathrm{mV\,s^{-1}}$.

3.8 Appendix C: Linear Fitting

In this appendix, we report the linear fits of the model to clinical data from the Fröberg *et al.* [150] and Åkerstedt *et al.* [149] studies described in Sec. 3.4. Measures of subjective fatigue in both studies adhere to a proportionality:

$$\text{Relative Fatigue} = 9.2 \times \frac{W}{1\,\mathrm{mV}}. \tag{3.11}$$

The Fröberg adrenaline excretion (males) obeys

$$\text{Adrenaline Excretion} = (3.0C - 13)\,\mathrm{ng/min}. \tag{3.12}$$

The Åkerstedt adrenaline excretion (females) obeys

$$\text{Adrenaline Excretion} = (1.7C + 0.3)\,\mathrm{ng/min}. \tag{3.13}$$

The Åkerstedt body temperature data obeys

$$\text{Body Temperature} = \left(-0.053\frac{D}{1\,\mathrm{mV}} + 36.73\right)^{\circ}\mathrm{C}. \tag{3.14}$$

Chapter 4

A Quantitative Physiologically-Based Model of the Sleep-Wake Switch Including the Orexin Group

Abstract

A quantitative, physiologically-based model of sleep-wake and arousal-state dynamics is developed which includes the wake-active monoaminergic brainstem nuclei (MA), the sleep-active ventrolateral preoptic nucleus (VLPO), the orexinergic neurons (Orx) in the lateral hypothalamic area, and the homeostatic and circadian drives. Reducing the Orx input to the MA is found to yield changes to the model's structure that correspond to the symptoms of (orexin-deficient) narcoleptic patients. The presence of Orx in the model slows the sleep-wake transition without affecting the wake-sleep transition, suggesting a possible role in sleep inertia. Sensitivities of the model's predicted arousal level variation to homeostatic and circadian inputs to Orx are investigated. The ubiquitous postlunch dip in arousal is postulated to result from a net in-

hibitory circadian connection to Orx. Furthermore, combining both circadian and adenosine-mediated homeostatic inputs to Orx produces a variation in waking arousal levels that exhibits quantitative agreement with existing clinical performance data. This is the first physiologically-based model to predict the dynamics of daytime vigilance and performance, which has been treated phenomenologically in the past.

4.1 Introduction

Since the simultaneous discovery of the orexin A and orexin B neurotransmitters (also termed hypocretin 1 and 2) by Sakurai *et al.* [92] and de Lecea *et al.* [93] in 1998, the orexinergic neurons (Orx) in the lateral hypothalamic area (LHA) have been implicated in a large variety of neurological processes, including a key role in the regulation of sleep and wakefulness [51, 94]. Loss of orexin neurons characterizes the neurodegenerative disorder narcolepsy [177], as was originally identified in mice [95], and later in humans [96, 97]. In narcoleptic patients, who make up approximately 0.05% of the population [178], the sleep-wake distinction is weak [95, 98, 99, 179], resulting in disturbed sleep, drowsiness, unintentional napping, and difficulty in waking from sleep [100]. The orexins have also been implicated in feeding [92, 180, 181], breathing [182], emotion, reward function, and motivation [111, 146, 161, 183]. Since the discovery of the orexins, numerous physiological studies have been crucial in determining the neurological pathways through which they act [52, 99, 112, 129, 130].

Phenomenological models of sleep-wake dynamics, building on the qualitative framework of Borbély's two-process model [56], have been successful in predicting a range of sleep-wake behaviors [58]. However, incorporating the discovery and subsequent physiological characterization of the orexin group into such models poses a particular challenge because a solid physiological framework is lacking. In contrast, physiologically-based sleep models, like that developed by Phillips and Robinson [1], model the relevant neuronal interac-

tions explicitly. As such, it is relatively straightforward to incorporate new physiological information. In this chapter the Phillips-Robinson model, which includes the mutually inhibitory VLPO and MA neuronal populations and the homeostatic and circadian drives, is extended to incorporate the orexin group. Physiological information about neuromodulatory interactions [52, 111, 112] and the circadian [184] and homeostatic [185] inputs to Orx is included. The dynamics of the orexin group were effectively averaged over in the original Phillips-Robinson sleep model, contributing a constant drive to the MA group [1]. Hence, including Orx as a neuronal population in the model effectively introduces a dynamic drive to the MA, the consequences of which are the focus of this work.

In this chapter, we explore dynamical and clinical implications of adding the orexin group to the Phillips-Robinson model. The extended model is introduced in Sec. 4.2 and is analyzed rigorously in Sec. 4.3. The *drive space* equilibrium representation of the model introduced in Sec. 4.4 allows us to compare the original Phillips-Robinson model, in which the input to the MA was approximated as a constant, to the present one in which it varies with time, and to demonstrate the qualitative occurrence of narcolepsy from reduced MA inputs. In the remaining sections, we explain the numerical output of the model in terms of the dynamical analysis of the preceding sections and discuss the clinical significance of the results. In Sec. 4.5, the drive to the orexin group is held constant for simplicity, to compare the dynamics in the first instance to those of the original Phillips-Robinson model, in the absence of the complicating time-dependence. Homeostatic and circadian inputs to the Orx are introduced sequentially in Sec. 4.6, and we demonstrate that the characteristic arousal variation predicted by the model, including the postlunch dip, stems from these inputs. Reducing the orexinergic input to the MA is shown to induce changes to the model's structure that are qualitatively consistent with the symptoms of narcolepsy. The main findings are summarized in Sec. 4.7.

4.2 Sleep Model

In this section we introduce the physiologically-based sleep model, an extension of the Phillips-Robinson model used in Chapters 2 and 3 that includes Orx. A summary of the physiology is given in Sec. 4.2.1, followed by an introduction to the neuronal population modeling approach in Sec. 4.2.2. The interactions between neuronal populations are explained and incorporated into the model in Sec. 4.2.3 and the parameter constraints are briefly summarized in Sec. 4.2.4.

4.2.1 Physiology

Sleep-wake dynamics are thought to be governed by the *circadian* and *homeostatic* drives. The 24 h periodic circadian signal originates in the suprachiasmatic nucleus (SCN) and maintains the entrainment of the sleep-wake cycle to the light cycle [51]. The homeostatic drive increases with time spent awake, which is believed to be due to a net build up of the somnogenic metabolic byproduct adenosine in the basal forebrain [107, 114, 115]. During sleep, metabolic rates are low and adenosine is cleared faster than it is produced [115–117].

The overall arousal state of the brain is controlled by a series of wake-active brainstem nuclei, collectively termed the ascending arousal system (AAS), which diffusely project neuromodulators to the cerebrum [50, 106, 107]. Based on common effects and temporal patterns of activity, AAS nuclei can be broadly classified as monoaminergic (MA), acetylcholine-related (ACh), or orexinergic (Orx). The MA group includes nuclei that use monoaminergic neurotransmitters: the histaminergic tuberomammillary nucleus (TMN), norepinephrinergic locus coeruleus (LC), serotoninergic dorsal raphé nucleus (DR), and dopaminergic ventral tegmental area (VTA) [31, 107, 108]. The ACh group includes nuclei that express acetylcholine, including the pedunculopontine (PPT) and laterodorsal (LDT) tegmental nuclei in the mesopontine tegmentum [109, 110]. Orx refers the orexinergic neurons of the LHA. While the MA and Orx groups

are active during wake and suppressed during sleep, the neurons of the ventrolateral preoptic area (VLPO) of the hypothalamus are active during sleep and are suppressed during wake. In Sec. 4.2.3, the interactions between the above nuclei, including the impact of the circadian and homeostatic drives, are explained.

4.2.2 Modeling Approach

The sleep model proposed in this chapter is an extension of the neuronal population model of Phillips and Robinson [1], used in Chapters 2 and 3. The model considers the average properties of large populations of neurons and their interactions, and is based on previous approaches to modeling the corticothalamic system [82–84]. The original model contained two neuronal populations: the MA and VLPO; here it is extended to include the Orx. Each neuronal population $j = v, m, x$, where v represents the VLPO, m represents the MA, and x represents the Orx, is characterised by its mean cell-body potential $V_j(t)$ relative to resting. The mean firing rate $Q_j(t)$ is approximated as a sigmoidal function of $V_j(t)$ [82]:

$$Q_j = S(V_j) = \frac{Q_{\max}}{1 + \exp[-(V_j - \theta)/\sigma']}, \tag{4.1}$$

where $Q_{\max}$ is the maximum possible firing rate, θ is the mean firing threshold relative to resting, and $\sigma'\pi/\sqrt{3}$ is its standard deviation [84]. Due to the small spatial extent of the relevant nuclei, we assume spatial homogeneity of each population and neglect propagation delays between neurons. This is a reasonable assumption because interactions within the relevant neuronal populations occur on time scales of milliseconds, whereas the current model is concerned with the dynamics of sleep and wake, which (even transitions between states) occur on time scales of seconds or longer.

Interactions between neuronal populations are assumed to be proportional to the firing rate Q_i of the relevant input population; the constants ν_{ij} weight

the input from population $j = v, m, x$ to population $i = v, m, x$. The time constants τ_i determine the rate at which the V_i dynamics evolve, due to the decay rate of the neuromodulator expressed by group i, for example. The equations governing the dynamics between three populations: v, m, and x can be represented in the following general form:

$$\begin{pmatrix} \tau_v & 0 & 0 \\ 0 & \tau_m & 0 \\ 0 & 0 & \tau_x \end{pmatrix} \begin{pmatrix} \dot{V}_v \\ \dot{V}_m \\ \dot{V}_x \end{pmatrix} = \begin{pmatrix} -1 & \nu_{vm}S & \nu_{vx}S \\ \nu_{mv}S & -1 & \nu_{mx}S \\ \nu_{xv}S & \nu_{xm}S & -1 \end{pmatrix} \begin{pmatrix} V_v \\ V_m \\ V_x \end{pmatrix} + \begin{pmatrix} D_v \\ D_m \\ D_x \end{pmatrix}, \quad (4.2)$$

where S is the sigmoid operator: $S\,V_i \equiv S(V_i)$ and the ν_{ij} weight the input from neuronal population j to i. The external drives

$$\begin{pmatrix} D_v \\ D_m \\ D_x \end{pmatrix} = \begin{pmatrix} \nu_{vc} & \nu_{vh} \\ \nu_{mc} & \nu_{mh} \\ \nu_{xc} & \nu_{xh} \end{pmatrix} \begin{pmatrix} C \\ H \end{pmatrix} + \begin{pmatrix} A_v \\ A_m \\ A_x \end{pmatrix} + \begin{pmatrix} \Delta D_v \\ \Delta D_m \\ \Delta D_x \end{pmatrix}, \quad (4.3)$$

consist of linear combinations of the circadian (C) and homeostatic (H) drives, constant offsets $\mathbf{A} = (A_v, A_m, A_x)$ due to other nuclei not explicitly modeled, and external perturbations $\Delta\mathbf{D}(t) = (\Delta D_v, \Delta D_m, \Delta D_x)$ due to sensory or pharmaceutical effects, for example.

The 24 h periodic circadian drive is taken to be well entrained to the daily fluctuation in light intensity and is approximated as a sinusoidal function of time

$$C(t) = \sin \omega t, \quad (4.4)$$

where $\omega = (2\pi/24)\,\mathrm{h}^{-1}$ and an oscillation amplitude of unity is used without loss of generality because the actual amplitude is absorbed into the relevant connectivity parameter ν_{ic}. Note that the constant offset c_0 used in previous work [1, 81] and in Chapters 2 and 3 of this thesis was appropriate because the circadian drive was an input to the VLPO only ($\nu_{vc}c_0$ contributed a constant drive to the VLPO). In this chapter, however, a more consistent notation is

used: constant external drives are encapsulated in **A**. The homeostatic sleep drive is modeled by the somnogen level H, which represents the concentration of extracellular adenosine in the basal forebrain. The somnogen clearance rate is assumed to be proportional to its concentration, with production approximated as a linear function of Q_m because MA activity is well correlated with arousal [118] and, presumably, metabolism [116]. Assuming that $Q_m = 0\,\mathrm{s}^{-1}$ results in negligible net production yields

$$\chi\dot{H} + H = \mu Q_m, \tag{4.5}$$

where χ is the characteristic somnogen clearance time and μ is a constant. The value of H grows during wake to a maximum at sleep onset, and decreases during sleep to a minimum at the end of a sleep period. Note that, in contrast to the saturating form used in Chapter 3 [Eq. (3.7)], the current form uses the simpler linear approximation justified in Chapter 2, as the high D_v (sleep deprivation) regime is not encountered in this chapter, and time spent in transitions is minimal [1].

4.2.3 Neuronal Interactions

The interactions known from physiology place constraints on the connection parameters ν_{ij} of the general set of Eqs (4.2) and (4.3). Since the VLPO and MA are mutually inhibitory [49, 79], we set $\nu_{mv}, \nu_{vm} < 0$. The Orx excites the MA [99], including the DR [186], the LC [187], the TMN [188], implying that $\nu_{mx} > 0$. The MA inhibits Orx through projections from serotonin and norepinephrine [183, 189], yielding $\nu_{xm} < 0$. The inhibition from the VLPO to Orx [52] implies that $\nu_{xv} < 0$, but there is no evidence for a significant projection back from Orx onto the VLPO [190], giving $\nu_{vx} = 0$. The firing rate of the MA group Q_m reflects the overall arousal level [118], which feeds back as a significant excitatory drive to Orx [112, 130]. This effect is not explicitly incorporated here but, if included, would take the form of a modulatory ΔD_x,

which would also encapsulate input from the limbic system, for example [111, 112].

Adenosine inhibits the orexin group [185, 191] and disinhibits the VLPO [50, 51] and hence $\nu_{xh} < 0$ and $\nu_{vh} > 0$. The VLPO receives an inhibitory projection from the DMH, which itself receives an excitatory circadian projection from molecular-level oscillations in the SCN [50, 51, 113], so that $\nu_{vc} < 0$. The orexin group also receives a strong projection from neurons containing glutamate and thyrotropin-releasing hormone in the DMH [53]. As a result, orexin concentrations have been observed to exhibit pronounced circadian fluctuations [148, 184, 192]. This projection has previously been assumed to be excitatory ($\nu_{xc} > 0$); however, we shall investigate the behavioral predictions of the model for both $\nu_{xc} > 0$ and $\nu_{xc} < 0$ in Sec. 4.6.2. There is no evidence for a direct connection of either drive to the MA, so we set both couplings to zero: $\nu_{mc} = \nu_{mh} = 0$. As a first approximation, and as a means of focusing on the orexinergic contribution to the MA, we neglect other inputs to the MA, from ACh and cortical projections, for example, by setting $A_m = 0$. This simplification allows us to focus on an entirely orexinergic MA drive. Given further constraints, a nonzero A_m could be included in the future, which would effectively average some of the orexinergic dynamics to a constant level.

The model resulting from the above interconnections is depicted schematically in Fig. 4.1. The mutual inhibition between the VLPO and MA is central to the model, with the homeostatic and circadian drives afferent to the VLPO and Orx. External sensory stimuli impact the MA group directly [118], while the limbic system projects to the orexin group [111]. Ignoring external pertur-

bations ($\Delta\mathbf{D} = 0$), we obtain the following set of equations

$$\begin{pmatrix} \tau_v & 0 & 0 \\ 0 & \tau_m & 0 \\ 0 & 0 & \tau_x \end{pmatrix} \begin{pmatrix} \dot{V}_v \\ \dot{V}_m \\ \dot{V}_x \end{pmatrix} = \begin{pmatrix} -1 & \nu_{vm}S & 0 \\ \nu_{mv}S & -1 & \nu_{mx}S \\ \nu_{xv}S & \nu_{xm}S & -1 \end{pmatrix} \begin{pmatrix} V_v \\ V_m \\ V_x \end{pmatrix} + \begin{pmatrix} \nu_{vc} & \nu_{vh} \\ 0 & 0 \\ \nu_{xc} & \nu_{xh} \end{pmatrix} \begin{pmatrix} C \\ H \end{pmatrix} + \begin{pmatrix} A_v \\ 0 \\ A_x \end{pmatrix}, \tag{4.6}$$

which govern the dynamics of the current model. For comparison, the original Phillips-Robinson model can be represented in the following form:

$$\begin{pmatrix} \tau_v & 0 \\ 0 & \tau_m \end{pmatrix} \begin{pmatrix} \dot{V}_v \\ \dot{V}_m \end{pmatrix} = \begin{pmatrix} -1 & \nu_{vm}S \\ \nu_{mv}S & -1 \end{pmatrix} \begin{pmatrix} V_v \\ V_m \end{pmatrix} + \begin{pmatrix} \nu_{vc} & \nu_{vh} \\ 0 & 0 \end{pmatrix} \begin{pmatrix} C \\ H \end{pmatrix} + \begin{pmatrix} A_v \\ A_m \end{pmatrix}. \tag{4.7}$$

In the limit $\tau_x \to \infty$, orexinergic dynamics can be time-averaged to a constant. We then identify the time average of $\nu_{mx}Q_x$ with A_m. In this limit, Eq. (4.6) reduces to Eq. (4.7) for the original Phillips-Robinson model. The remainder of this chapter therefore focuses on a characterization of the new dynamics resulting from making this input to the MA vary with time according to the physiological processes known to influence Orx.

4.2.4 Parameter Constraints

Compared to the original Phillips-Robinson model, the current model includes seven new parameters: τ_x, ν_{mx}, ν_{xm}, ν_{xv}, ν_{xc}, ν_{xh}, and A_x. The original parameters of the Phillips-Robinson model have been well-constrained by physiology previously [1, 81] and so (excepting the replacement of A_m by $\nu_{mx}Q_x$) we leave them unchanged. The signs of the neuronal connectivities ν_{mx}, ν_{xm}, and ν_{xv} are constrained by physiology and, along with the constant drive A_x, have been chosen to maintain the model's sleep length at 8.5 h, the hysteresis loop width

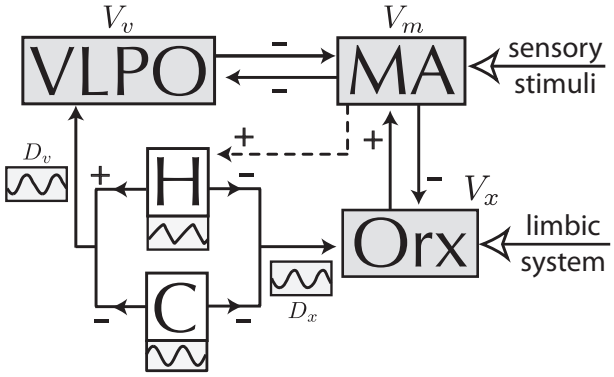

Figure 4.1: *Schematic of the sleep model introduced in this paper. The sleep-active VLPO, and wake-active MA and Orx neuronal populations are shown. Arrows indicate interactions between the groups, which are either excitatory (+) or inhibitory (−). The homeostatic (H) and circadian (C) drives combine to form the resultant drives D_v and D_x to the VLPO and Orx groups, respectively. Additional inputs are demonstrated using large labeled arrows: external sensory stimuli affect the MA and the Orx receives input from the limbic system. Arousal state feedback from the MA onto H is shown dashed.*

at $\approx 1\,\mathrm{mV}$, and the firing rate Q_m near $0\,\mathrm{s}^{-1}$ during sleep and near $5\,\mathrm{s}^{-1}$ during wake, as per the original Phillips-Robinson sleep model [1, 81]. In addition, the firing rate Q_x has been constrained to approximately 4–$8\,\mathrm{s}^{-1}$ during waking and $< 1\,\mathrm{s}^{-1}$ during sleep from physiological data [129, 130]. The other parameters: τ_x, ν_{xh}, ν_{xc} are constrained on behavioral grounds in Secs 4.5.3, 4.6.1, and 4.6.2, respectively. The resulting parameters used in this chapter are listed in Table 4.1.

Table 4.1: *Nominal model parameter values.*

Param.	Value	Param.	Value	Param.	Value
ν_{vm}	$-2.1\,\mathrm{mV\,s}$	ν_{mv}	$-1.8\,\mathrm{mV\,s}$	ν_{vh}	$1.0\,\mathrm{mV\,nM^{-1}}$
ν_{mx}	$0.2\,\mathrm{mV\,s}$	ν_{xm}	$-0.1\,\mathrm{mV\,s}$	ν_{xh}	$-1.0\,\mathrm{mV\,nM^{-1}}$
ν_{xv}	$-1.0\,\mathrm{mV\,s}$	ν_{vc}	$-2.9\,\mathrm{mV}$	ν_{xc}	$-1.0\,\mathrm{mV}$
A_x	$9.5\,\mathrm{mV}$	A_v	$-13\,\mathrm{mV}$	μ	$4.4\,\mathrm{nM\,s}$
$Q_{\max}$	$100\,\mathrm{s}^{-1}$	θ	$10\,\mathrm{mV}$	σ'	$3\,\mathrm{mV}$
τ_m	$10\,\mathrm{s}$	τ_v	$10\,\mathrm{s}$	τ_x	$30\,\mathrm{min}$
χ	$45\,\mathrm{h}$				

4.3 Mathematical Analysis

In this section we analyze the model's equations and develop a representation of the model that aids a formal understanding of its dynamics. We take a similar approach to that reported for the original Phillips-Robinson model in Sec. 2.3, in which the model was characterized in V_v–V_m space using equilibrium and linear stability analyses.

4.3.1 Equilibrium Analysis

The governing equations of the model, given in Eq. (4.6), can be written more compactly as

$$\begin{pmatrix} \tau_v \dot{V}_v \\ \tau_m \dot{V}_m \\ \tau_x \dot{V}_x \end{pmatrix} = \begin{pmatrix} -1 & \nu_{vm} S & 0 \\ \nu_{mv} S & -1 & \nu_{mx} S \\ \nu_{xv} S & \nu_{xm} S & -1 \end{pmatrix} \begin{pmatrix} V_v \\ V_m \\ V_x \end{pmatrix} + \begin{pmatrix} D_v \\ D_m \\ D_x \end{pmatrix}, \tag{4.8}$$

where the drives have been combined into the column vector $\mathbf{D}(t) = (D_v, D_m, D_x)$. In $\mathbf{V}$-space (i.e., the space spanned by V_v, V_m, and V_x), the dynamics can be interpreted in terms of the null conditions $\dot{V}_v = 0$:

$$V_v = \nu_{vm} S(V_m) + D_v, \tag{4.9}$$

$\dot{V}_m = 0$:

$$V_m = \nu_{mv} S(V_v) + \nu_{mx} S(V_x) + D_m, \tag{4.10}$$

and $\dot{V}_x = 0$:

$$V_x = \nu_{xv} S(V_v) + \nu_{xm} S(V_m) + D_x, \tag{4.11}$$

which represent surfaces in $\mathbf{V}$-space, as shown in Fig. 4.2. Fixed points $\mathbf{V}^* = (V_v^*, V_m^*, V_x^*)$ are given by the intersection of the three surfaces, and are plotted using circles in Fig. 4.2. Each drive D_i translates the $\dot{V}_i = 0$ surface in the V_i direction.

In this model, we take $\tau_x \gg \tau_v, \tau_m$, as will be justified in Sec. 4.5.3 on behavioral grounds. Hence the dynamics in the V_v and V_m directions are much more rapid than those in the V_x direction. As justified in Chapter 2, if the drives D_i are slowly varying on the time scale τ_x, they can be treated as control parameters for the system. In this limit, we find that $\dot{V}_v \approx \dot{V}_m \approx 0$ on time scales much longer than τ_v and τ_m. The system can be considered to have converged onto the intersection of the $\dot{V}_v = 0$ and $\dot{V}_m = 0$ surfaces, whence the model can be appropriately represented as a projection onto either of the V_x–V_m or V_x–V_v subspaces. Since $\nu_{vx} = 0$, the V_x–V_m projection is more tractable analytically, and will be characterized in Sec. 4.3.3.

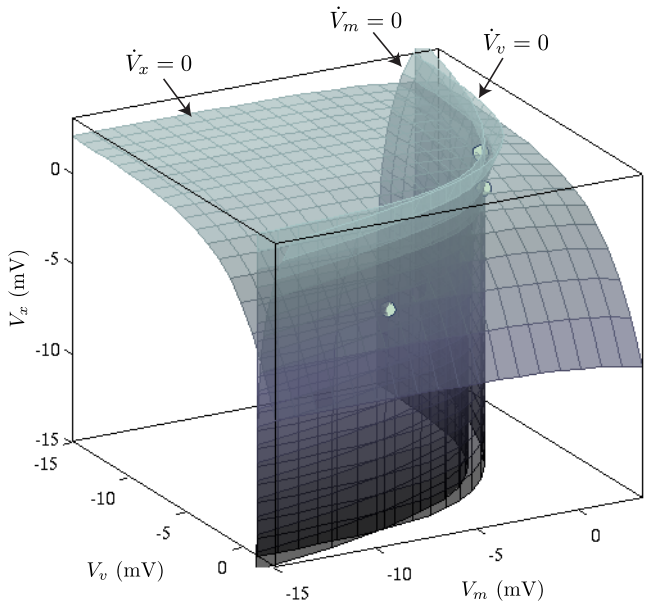

Figure 4.2: *The $\dot{V}_v = 0$, $\dot{V}_m = 0$, and $\dot{V}_x = 0$ surfaces in V_v–V_m–V_x space for $D_v = 1.5\,\mathrm{mV}$, $D_m = 0\,\mathrm{mV}$, $D_x = 2\,\mathrm{mV}$ (in the bistable region – c.f., Sec. 4.4.2). Fixed points, $\dot{V}_v = \dot{V}_m = \dot{V}_x = 0$, are given by the intersection of the three surfaces, and are plotted using circles. For this set of drives, there are three equilibriums: the intermediate equilibrium is a saddle point and the other two are stable nodes.*

4.3.2 Linear Stability Analysis

The linear stability of a fixed point $\mathbf{V}^*$ can be determined from the Jacobian matrix [121]

$$\begin{aligned}\mathbf{J} &= \left.\begin{pmatrix} \partial\dot{V}_v/\partial V_v & \partial\dot{V}_v/\partial V_m & \partial\dot{V}_v/\partial V_x \\ \partial\dot{V}_m/\partial V_v & \partial\dot{V}_m/\partial V_m & \partial\dot{V}_m/\partial V_x \\ \partial\dot{V}_x/\partial V_v & \partial\dot{V}_x/\partial V_m & \partial\dot{V}_x/\partial V_x \end{pmatrix}\right|_{(V_v^*,V_m^*,V_x^*)}, \\ &= \begin{pmatrix} -\tau_v^{-1} & \tau_v^{-1}\nu_{vm}S'(V_m^*) & 0 \\ \tau_m^{-1}\nu_{mv}S'(V_v^*) & -\tau_m^{-1} & \tau_m^{-1}\nu_{mx}S'(V_x^*) \\ \tau_x^{-1}\nu_{xv}S'(V_v^*) & \tau_x^{-1}\nu_{xm}S'(V_m^*) & -\tau_x^{-1} \end{pmatrix}, \end{aligned} \tag{4.12}$$

where

$$S'(x) = \frac{d}{dx}S(x) = \frac{\exp\left(-\frac{x-\theta}{\sigma'}\right)}{Q_{\max}}S^2(x). \tag{4.13}$$

For each equilibrium, the eigenvalues λ_1, λ_2, and λ_3 of $\mathbf{J}$ satisfy $\det(\mathbf{J}-\lambda\mathbf{I}) = 0$, where $\mathbf{I}$ is the 3×3 identity matrix, and determine the local stability of the system in the vicinity of the fixed point $\mathbf{V}^*$.

The eigenvalues $\lambda_1, \lambda_2, \lambda_3$ of the $\mathbf{J}$ [Eq. (4.12)] are given by the roots of the characteristic equation

$$-\lambda^3 + \lambda^2\,\mathrm{Tr}(\mathbf{J}) + \frac{\lambda}{2}\left[\mathrm{Tr}(\mathbf{J}^2) - \mathrm{Tr}(\mathbf{J})\right] + \det(\mathbf{J}). \tag{4.14}$$

The sum of the roots $\lambda_1 + \lambda_2 + \lambda_3 = \mathrm{Tr}(\mathbf{J}) = -(\tau_v^{-1} + \tau_m^{-1} + \tau_x^{-1}) < 0$ and hence the eigenvalues cannot all be positive – i.e., there are no unstable nodes [121]. For $D_x = 2\,\mathrm{mV}$ and as a function of D_v, the eigenvalues are plotted in Fig. 4.3. For the nominal parameters in this model, as given in Tab. 4.1, we find only stable nodes ($\lambda_1, \lambda_2, \lambda_3 < 0$) and unstable saddle points ($\lambda_1, \lambda_2 < 0$, $\lambda_3 > 0$). One eigenvalue, corresponding to the characteristic rate of attraction onto a fixed point along the $\dot{V}_v = \dot{V}_m = 0$ nullcline, is much smaller than the others, and corresponds to the rapid dynamics onto the $\dot{V}_v = \dot{V}_m = 0$ nullcline. These rapid dynamics occur in a way similar to the original model

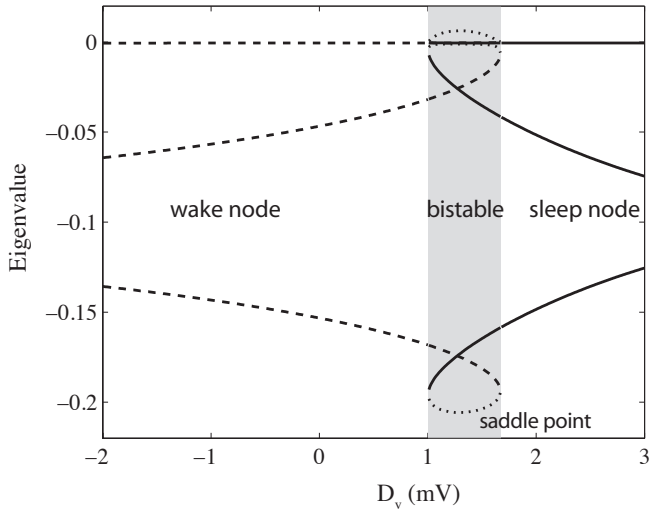

Figure 4.3: *The eigenvalues of the model as a function of D_v, with $D_x = 2\,\mathrm{mV}$. There is a stable wake node (dashed line) at low D_v with $\lambda_1, \lambda_2, \lambda_3 < 0$, a stable sleep node (solid line) at high D_v with $\lambda_1, \lambda_2, \lambda_3 < 0$, and an intermediate bistable region in which both stable nodes exist simultaneously along with an unstable saddle point (dotted line) with $\lambda_1, \lambda_2 < 0$ and $\lambda_3 > 0$. One eigenvalue, corresponding to the slower dynamics (along the $\dot{V}_v = \dot{V}_m = 0$ nullcline) is much smaller in magnitude than the others, which characterize to the rapid attraction onto the $\dot{V}_v = \dot{V}_m = 0$ nullcline.*

(c.f., Fig. 2.5), with faster attraction in one eigendirection relative to the other. The main equilibrium structure of the model is therefore similar to that of the original model – being altered only slightly by the slow dynamics (on a time scale $\sim \tau_x$) in an additional dimension. Note that, in the limit $\tau_x \to \infty$, the additional eigenvalues vanish, and the dynamics of the model reduces to that of the original Phillips-Robinson model, characterized in Sec. 2.3.

4.3.3 Reduction to the V_x–V_m plane

Under the assumption that $\dot{V}_v \approx 0$, V_v can be eliminated from the model equations, whence the system's dynamics in the V_x–V_m plane can be understood in terms of two nullclines, given by $\dot{V}_m = \dot{V}_v = 0$ and $\dot{V}_m = \dot{V}_x = 0$, respectively.

The $\dot{V}_m = \dot{V}_v = 0$ nullcline

$$V_m = \nu_{mv} S[\nu_{vm} S(V_m) + D_v] + \nu_{mx} S(V_x) + D_m, \tag{4.15}$$

can be rearranged to give

$$V_x = S^{-1}\left\{ \frac{V_m - \nu_{mv} S[\nu_{vm} S(V_m) + D_v] - D_m}{\nu_{mx}} \right\}, \tag{4.16}$$

for V_x as a function of V_m, where the inverse sigmoid $S^{-1}(x)$ is defined over $0 < x < Q_{\max}$ by $S^{-1}(x) = -\sigma \ln(Q_{\max}/x - 1) + \theta$. The $\dot{V}_x = \dot{V}_v = 0$ nullcline is given by

$$V_x = \nu_{xv} S[\nu_{vm} S(V_m) + D_v] + \nu_{xm} S(V_m) + D_x. \tag{4.17}$$

Since $\tau_x \gg \tau_m, \tau_v$, the system will be close to the $\dot{V}_m = \dot{V}_v = 0$ nullcline on time scales much longer than τ_v and τ_m. Trajectories through the V_x–V_m plane will therefore attract rapidly onto the $\dot{V}_m = \dot{V}_v = 0$ nullcline (on a time scale $\sim \tau_m, \tau_v$) and will remain close to this nullcline as it attracts more gradually (on a time scale $\sim \tau_x$) onto the fixed point defined by the intersection of Eqs (4.16) and (4.17), and given by the solution of

$$\begin{aligned} 0 = &- V_m + \nu_{mv} S[\nu_{vm} S(V_m) + D_v] \\ &+ \nu_{mx} S\left\{\nu_{xv} S[\nu_{vm} S(V_m) + D_v] + \nu_{xm} S(V_m) + D_x\right\} + D_m. \end{aligned} \tag{4.18}$$

From the solution V_m^* of Eq. (4.18), the equilibrium V_v^* and V_x^* values can subsequently be determined from Eqs (4.9) and (4.17), respectively.

To understand the model's dynamics in the V_x–V_m plane, it is useful to consider the system's *velocity* through it. This idea was used in Sec. 2.3 for the original Phillips-Robinson model in V_v–V_m space, revealing the system's wake and sleep ghosts. In $\mathbf{V}$-space, the velocity is given by $\dot{\mathbf{V}} = (\dot{V}_v, \dot{V}_m, \dot{V}_x)$, which has magnitude $\dot{V} = (\dot{V}_v^2 + \dot{V}_m^2 + \dot{V}_x^2)^{1/2}$. However, on time scales $\gg \tau_m, \tau_v$ (an assumption implicit in the V_x–V_m representation), $\dot{V}_v \approx \dot{V}_m \approx 0$. The

velocity $\dot{V}$ is then proportional to the gradient of the $\dot{V}_m = \dot{V}_v = 0$ nullcline, on which the system is confined. However, excepting transitions between sleep and wake, the $\dot{V}_m = \dot{V}_v = 0$ nullcline is approximately in the V_x direction and hence $\dot{V} \approx \dot{V}_x$. Regions of low $\dot{V}$ in the V_x–V_m plane are therefore concentrated around the $\dot{V}_v = \dot{V}_m = 0$ nullcline.

The V_x–V_m plane representation of the model is depicted in Figs 4.6(b)–(e) for different values of the drives D_v and D_x. As mentioned above, since $\tau_x \gg \tau_m, \tau_v$, the system remains close to the $\dot{V}_v = \dot{V}_m = 0$ nullcline (plotted as a solid line in the figures), on which the adiabatic dynamics occur. At low D_v and high D_x, the nullclines intersect at high V_m and V_x, yielding a stable wake node. At high D_v and low D_x, the nullclines intersect at low V_m and V_x, yielding a stable sleep node. At intermediate D_v and D_x, the nullclines have three points of intersection: the stable wake and sleep nodes and the unstable saddle point. Due to the curvature of the nullclines, the wake ghost (c.f., Sec. 2.3.4) is a more distinct region of near-stability than the sleep ghost. This effect is important for understanding the asymmetrical transition dynamics in Sec. 4.5.3. These features of the model are consistent with the original Phillips-Robinson model and its representation in V_v–V_m space, as characterized in Sec. 2.3. The V_x–V_m plane representation is a two-dimensional projection that illustrates the equilibrium state of the model and its dynamics, including the regions of low stability and the characteristic adiabatic dynamics along the $\dot{V}_v = \dot{V}_m = 0$ nullcline. It therefore captures the relevant dynamical features of the present model, and is used to explain the results obtained throughout this chapter.

4.3.4 Bifurcation Analysis

At equilibrium, $\dot{V}_m$ can be expressed as a function of V_m only [c.f. Eq. (4.18)]:

$$\begin{aligned}\tau_m \dot{V}_m = &- V_m + \nu_{mv} S[\nu_{vm} S(V_m) + D_v] \\ &+ \nu_{mx} S\left\{\nu_{xv} S[\nu_{vm} S(V_m) + D_v] + \nu_{xm} S(V_m) + D_x\right\} = 0. \end{aligned} \tag{4.19}$$

At a bifurcation point, the equilibrium condition (4.18) is satisfied, and its derivative with respect to V_m vanishes, giving

$$\begin{aligned}\tau_m \frac{d\dot{V}_m}{dV_m} = &- 1 + \nu_{mv}\nu_{vm} S'(V_m) S'\left[\nu_{vm} S(V_m) + D_v\right] \\ &+ \nu_{mx} S'(V_m)\left\{\nu_{xm} + \nu_{xv}\nu_{vm} S'\left[\nu_{vm} S(V_m) + D_v\right]\right\} \\ &\quad S'\left\{\nu_{xm} S(V_m) + \nu_{xv} S\left[\nu_{vm} S(V_m) + D_v\right] + D_x\right\} \\ &= 0. \end{aligned} \tag{4.20}$$

Eliminating the common expression $\nu_{xv} S[\nu_{vm} S(V_m) + D_v] + \nu_{xm} S(V_m) + D_x$ from Eqs (4.19) and (4.20) yields the bifurcation condition

$$\begin{aligned}-1 + \nu_{mv}\nu_{vm} S'(V_m) S'\left[\nu_{vm} S(V_m) + D_v\right] + \left\{\nu_{xm} + \nu_{xv}\nu_{vm} S'\left[\nu_{vm} S(V_m) + D_v\right]\right\} \\ \nu_{mx} S'(V_m) S'\left\{S^{-1}\left[\frac{V_m - \nu_{mv} S(\nu_{vm} S(V_m) + D_v)}{\nu_{mx}}\right]\right\} = 0, \end{aligned} \tag{4.21}$$

which can be solved for V_m for a given D_v. Given this solution, the other quantities: V_v, V_x, and D_x are uniquely determined from the above equilibrium equations. The bifurcation condition Eq. (4.21) can be used to determine the bistable structure of the model as a function of the dynamic drives D_v and D_x. It will be used to define the bifurcation boundary in the D_v–D_x plane, as plotted in Fig. 4.6 and described in Sec. 4.4.2.

4.4 Drive Space

In this section we introduce an equilibrium representation of the model, in a two-dimensional *drive space*. The problem of understanding the impact of external stimuli on the system was treated in the 'impulsive' limit in Sec. 2.4, on time scales much slower than that of the drives D_i. Now, in the opposite limit, if the drives D_i are slowly varying compared to the neuronal dynamics governed by τ_i, they can be treated as control parameters for the system. The system can then be considered to be close to equilibrium on time scales $\gg \tau_j$. We exploit this approximation in developing the drive space representation, which will also allow us to compare the dynamics of the original Phillips-Robinson model (in which $D_m = A_m$ was a constant) to that of the current model, in which input to the MA is proportional to the firing rate Q_x of the Orx. In Sec. 4.4.1, we introduce the D_v–D_m drive space in which orexinergic input is not explicitly included. The qualitative features of narcolepsy are shown to result from reducing the mean input drive to the MA in a preliminary simulation of the sleep disorder, that is revisited in Sec. 4.6.4. Then, in Sec. 4.4.2, we consider the current model and its representation in D_v–D_x space.

4.4.1 Dynamics in the D_v–D_m Plane

In this section the dynamics of the orexin group are ignored (i.e., we set $\nu_{mx} = 0$) and we consider general external drives to the VLPO and MA in the context of the original Phillips-Robinson model. Following the above rationale, on time scales $\gg \tau_m, \tau_v$, the slowly varying drives D_v and D_m can be treated as control parameters, allowing the system to be represented by its equilibrium state in a two-dimensional *drive space* spanned by D_v and D_m. Sources afferent from other nuclei or acting via indirect pathways will eventually be felt at the level of the central mutually inhibitory MA and VLPO nuclei and can thus be represented in the D_v–D_m plane. For example, using the notation introduced in Chapter 2, the drives $D_v = D_v^0 + \Delta D_v$ and $D_m = D_m^0 + \Delta D_m$ incorporate

slowly-varying inputs from other neuronal populations not explicitly modeled, such as ACh and Orx, the influence of pharmaceuticals, and slowly-varying sensory stimuli, for example, via $(\Delta D_v, \Delta D_m)$.

In Fig. 4.4(a), the equilibrium firing rate Q_m [obtained from Eq. (2.12), which is identical to Eq. (4.18) with $\nu_{xm} = 0$] is plotted in the D_v–D_m plane. The bistable region (upper-right in the figure) is separated by the saddle-node bifurcation boundary, which is given by Eq. (2.26):

$$S' \left[S^{-1} \left(\frac{V_m - D_m}{\nu_{mv}} \right) \right] S'(V_m) - \nu_{mv}^{-1} \nu_{vm}^{-1} = 0. \tag{4.22}$$

Inside the bistable region, two stable nodes and one saddle point exist; outside the bistable region, a single stable node exists. The left-most boundary represents a transition from sleep to wake and the right-most boundary represents a transition from wake to sleep. Thus, a trajectory entering the bistable region from the lower boundary remains a sleep state and one entering from the upper boundary remains a wake state. To elicit a change in state, an external drive $(\Delta D_v, \Delta D_m)$ must perturb the system to the bifurcation boundary furthest from its initial condition.

In the previous form of the model, D_m was averaged to a constant $D_m = A_m = 1.3\,\mathrm{mV}$ [1]. Movement through the D_v–D_m plane, and hence the time evolution of arousal state, resulted from the 24 h periodic oscillation of D_v. This path is plotted with a solid white line in Fig. 4.4(a) and exhibits hysteresis, transitioning from wake to sleep at the right-most bifurcation boundary and from sleep to wake at the left-most boundary. The familiar sleep-wake flip-flop [79] results, with either the VLPO or the MA dominating over the other during prolonged periods of sleep at high D_v, and wake at low D_v. Consistent with flip-flop dynamics, the two states are distinct and transitions between them are rapid.

In the two-dimensional V_v–V_m nullcline representation of the original model introduced in Sec. 2.3, the drive D_v translates the $\dot{V}_v = 0$ nullcline horizontally

and D_m translates the $\dot{V}_m = 0$ nullcline vertically. Every point in the D_v–D_m plane therefore corresponds to a unique orientation of the two nullclines relative to one other and hence a unique equilibrium or set of equilibriums. Four representative points in the D_v–D_m plane are plotted with circles in Fig. 4.4(a) and correspond to the V_v–V_m plane representations plotted in Figs 4.4(b)–(e). In contrast to the model's normal dynamics, there exist drives for which neither population dominates over the other, whence the labels 'sleep' and 'wake' become ambiguous. For example, the stable node equilibrium at $D_v = -1\,\mathrm{mV}$, $D_m = -1\,\mathrm{mV}$ [labeled 'X' in Fig. 4.4(a), and shown in Fig. 4.4(d)] has $Q_m = 1.5\,\mathrm{s}^{-1}$ and $Q_v = 2.5\,\mathrm{s}^{-1}$. Neither the MA nor the VLPO dominates over the other, but rather, both fire moderately. In a recent paper, Fuller *et al.* [193] described the sleep state as being "readily distinguishable from other states of 'altered consciousness,' such as coma and anesthesia, in that it is easily reversible and self-regulating". Interpreted within the present framework, the lower left region of the D_v–D_m plane, in which neither population dominates, may represent some form of coma or anesthetized state, for example. Relative to normal, persistent perturbative external drives $(\Delta D_v, \Delta D_m)$, which may have a pharmacological origin or be the result of altered neuronal circuitry, are required to maintain the system in these states. Note that changes in the model's parameters would alter the model's equilibriums, and may stabilize such states. A systematic study of this dependence for each of the model's parameters might yield insights into how specific abnormalities in physiological signaling give rise to such states. However such a treatment is beyond the scope of the current work.

As mentioned earlier, the mechanistic neurological pathway of external stimuli will eventually affect the fundamental MA–VLPO system, and can thus be represented as a perturbation vector $(\Delta D_v, \Delta D_m)$. In the short-duration impulsive limit considered in Sec. 2.4, stimuli do not affect the fundamental equilibrium structure of the model, and represent only transient disturbances

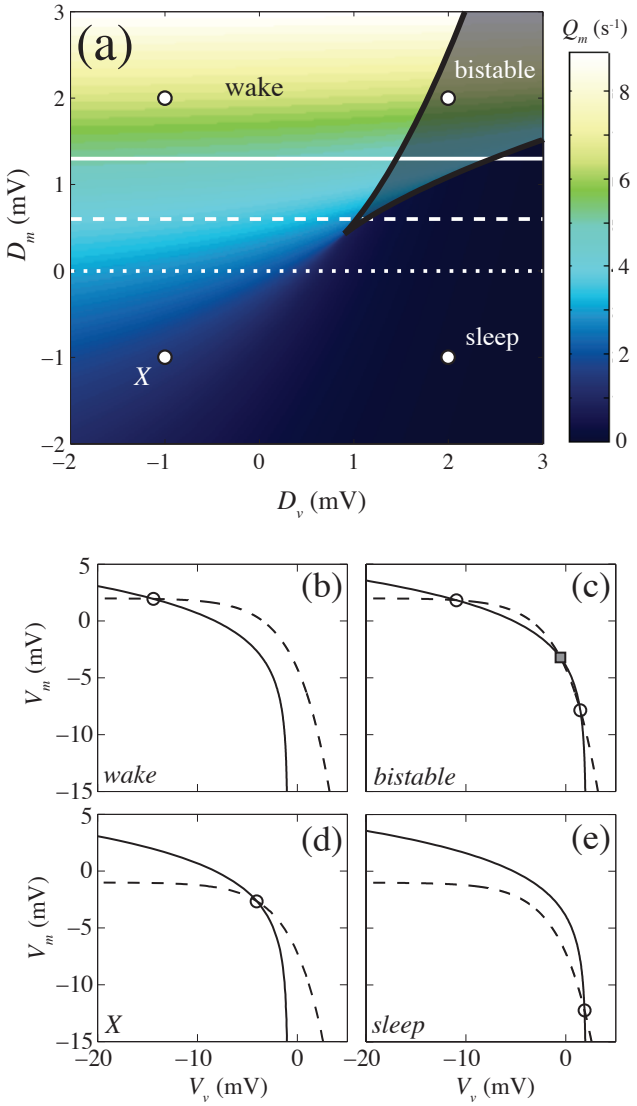

Figure 4.4: *(a) D_v–D_m drive space illustrating the waking firing rate Q_m, with white representing high Q_m (high arousal), and black representing low Q_m (sleep). The model is also represented in the V_v–V_m plane, showing the $\dot{V}_v = 0$ (solid) and $\dot{V}_m = 0$ (dashed) nullclines for the four points shown in (a), i.e., for (b) $D_v = -1\,\mathrm{mV}$, $D_m = 2\,\mathrm{mV}$, (c) $D_v = 2\,\mathrm{mV}$, $D_m = 2\,\mathrm{mV}$, (d) $D_v = -1\,\mathrm{mV}$, $D_m = -1\,\mathrm{mV}$, and (e) $D_v = 2\,\mathrm{mV}$, $D_m = -1\,\mathrm{mV}$. Stable node and saddle point equilibriums are labeled using circles and squares, respectively.*

to the system, which then relaxes back to equilibrium. However, slowly-varying disturbances alter the model's equilibrium structure and can be represented using the drive-space picture shown in Fig. 4.4(a). In future work, this picture is expected to aid an understanding of the impact of pharmaceuticals, which can be plotted as trajectories through the ΔD_v–ΔD_m plane, giving a unified representation for all external stimuli. The specific arousal-state impact of a stimulus can be determined by superimposing the $[\Delta D_v(t), \Delta D_m(t)]$ trajectory onto the normal model trajectory $[D_v^0(t), D_m^0(t)]$ in the D_v–D_m plane. In this way, the arousal-state impact of a range of external influences can be determined systematically and compared on the same scale.

A major aim of the present work is to determine the impact of the orexin group and, in particular, the occurrence of narcolepsy due to a deficiency of orexin neurons. Since orexinergic activity has an excitatory influence on the MA group, we now investigate the impact of reducing the mean input to the MA, as a preliminary exploration of the model's response. A more complete treatment, decreasing the orexinergic contribution to the MA drive within the new model, will be considered in Sec. 4.6.4. Lines of constant $A_m = 1.3\,\mathrm{mV}$, $0.6\,\mathrm{mV}$, and $0\,\mathrm{mV}$ are plotted in Fig. 4.4. Decreasing A_m decreases waking levels of arousal and reduces the width of the D_v–V_m hysteresis loop (i.e., the difference in D_v between the two bifurcation points). For $A_m \lesssim 0.4\,\mathrm{mV}$, the flip-flop hysteresis dynamics no longer occur; the system instead moves smoothly from low levels of arousal at low D_v to sleep at high D_v. The D_v–V_m hysteresis loops corresponding to the three trajectories plotted in Fig. 4.4(a) are shown in Fig. 4.5.

It has been demonstrated that narcoleptic patients have normal sleep homeostasis and circadian control [177, 194] and are characterized simply by "behavioral state instability, with apparently low thresholds to transition between states" [177]. This description is consistent with the effect of decreasing A_m in the Phillips-Robinson model, which decreases the extent of the bistable portion of the model's trajectory so that perturbative drives $(\Delta D_v, \Delta D_m)$ can induce

transitions between wake and sleep with a reduced threshold. In addition, the excessive daytime sleepiness of narcoleptic patients [48] is consistent with the reduced waking Q_m predicted by the model. A previous simulation of narcolepsy using the original Phillips-Robinson model postulated that orexin may alter the connections ν_{vm} and ν_{mv}, producing the same qualitative effect on the hysteresis loop [1]. However, the current method of decreasing A_m has a greater physiological justification, as a reduction in the orexinergic drive to the MA.

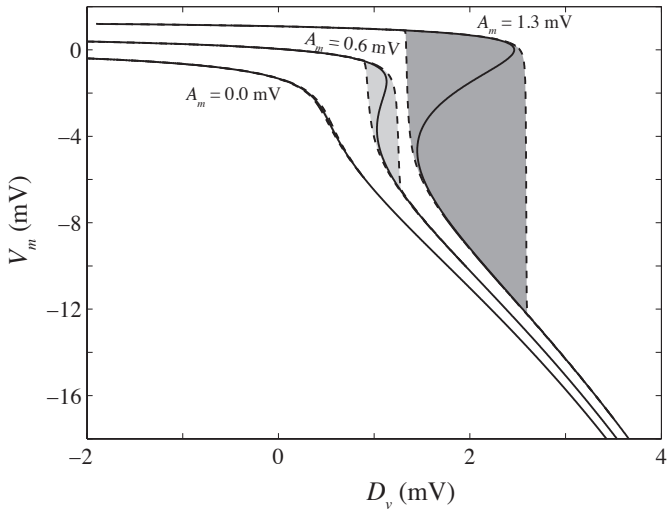

Figure 4.5: *The effect of reducing A_m on the D_v–V_m hysteresis loops of the original Phillips-Robinson model. The D_v–V_m hysteresis bifurcation diagrams (solid line) and corresponding model runs (dashed line) are plotted for $A_m =$ 1.3 mV (dark shading), $A_m = 0.6$ mV (light shading), and $A_m = 0.0$ mV. As A_m decreases, the waking arousal level decreases, the distinction between wake and sleep weakens, and the hysteresis loop width decreases.*

4.4.2 Dynamics in the D_v–D_x Plane

In the current model, D_v and D_x are the two dynamic drives, with $D_m = 0$. It is therefore appropriate to represent the model in the D_v–D_x plane. Since D_m in Sec. 4.4.1 represented the total drive to the MA, in the current model, this is

replaced by the orexinergic drive $\nu_{mx}Q_x > 0$. Since Q_x increases monotonically and nonlinearly with D_x, the Orx drive to the MA does also. Changing the vertical axis from D_m to D_x therefore constitutes a nonlinear transformation of this axis. In Fig. 4.6(a), the stable equilibrium firing rate Q_m is plotted in the D_v–D_x plane. As in the D_v–D_m plane representation shown in Fig. 4.4(a), a waking region exists at low D_v with an arousal level Q_m that increases with D_x, a bistable region exists at high D_v and D_x in which stable sleep and wake states exist simultaneously, and a sleep region exists at high D_v. In contrast to the original Phillips-Robinson model in which $\tau_m = \tau_v = 10\,\mathrm{s}$, in the current model $\tau_x = 30\,\mathrm{min} \gg \tau_m, \tau_v = 10\,\mathrm{s}$. Thus, the system lags further behind the equilibrium states shown in Fig. 4.6 than an equivalent trajectory in the D_v–D_m plane, due to the rate-limiting dynamics along the $\dot{V}_v = \dot{V}_m = 0$ nullcline. However, it is still a useful representation to analyze, as it clearly demonstrates some of the key qualitative characteristics of the current model.

In a way that qualitatively matches the trend of decreasing A_m, as analyzed above, lowering the mean drive A_x lowers the waking arousal level and decreases the width of the hysteresis loop. For $D_x \lesssim -1\,\mathrm{mV}$, the dynamics no longer exhibit bistability or hysteresis. As shown in Fig. 4.6(a), the sleep-wake distinction is weakened, but a transition point (at $D_v \approx 0.6\,\mathrm{mV}$) still exists, in contrast to the smooth transition encountered at low D_m – the presence of orexin in the system, even at low D_x, plays a role in maintaining the integrity of the sleep and wake states. We note that reducing D_x gives qualitatively similar dynamics to reducing D_m in the model; i.e., yielding dynamics qualitatively similar to those of narcolepsy. Since D_x contains a motivation/emotion-related component, we speculate that subjects with reduced emotional signaling or a lower mean motivation, may exhibit symptoms analogous to that of narcolepsy, albeit a less severe version. For example, a mean decrease in motivational input to Orx would lower D_x, decreasing waking arousal levels and weakening the bistable buffer between sleep and wake. We thus speculate a possible link

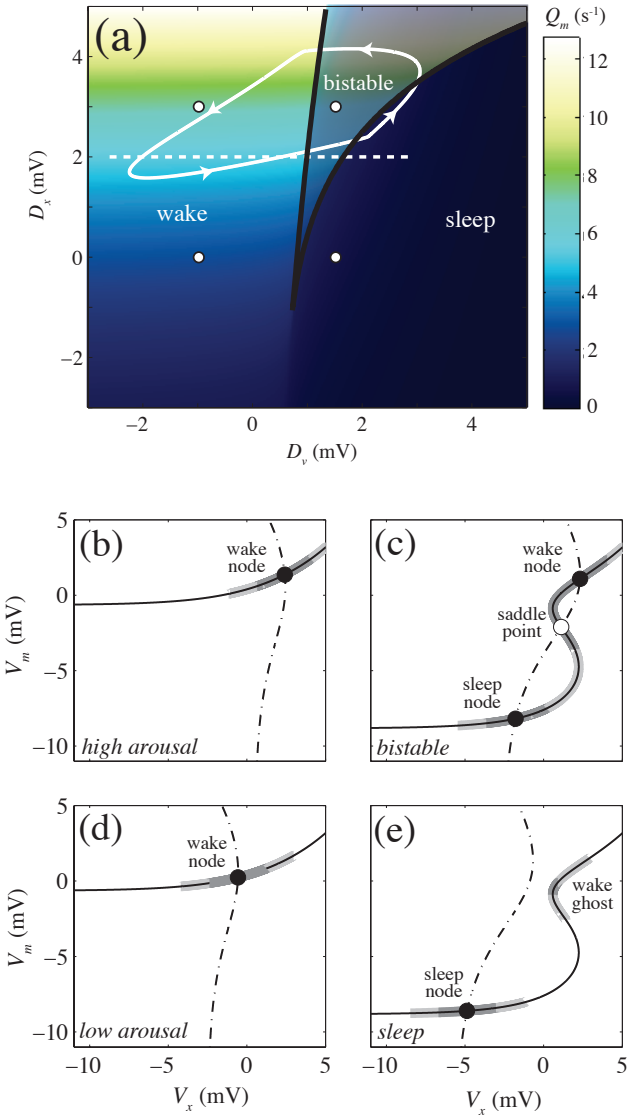

Figure 4.6: *(a) The equilibrium Q_m as a function of the two drives D_v and D_x. Approximate 'wake', 'sleep', and 'bistable' regions are labeled, with the bistable region bounded by the saddle-node bifurcation curve [c.f., Eq. (4.21)]. Trajectories through this space are plotted: for a constant $D_x = 2\,\mathrm{mV}$, as treated in Sec. 4.5 (dashed white line), and for a dynamic $D_x = \nu_{xc}C + \nu_{xh}H + A_x$, as treated in Sec. 4.6 (solid white line). (b)–(e) V_x–V_m nullcline plots (c.f., Sec. 4.3.3) at each of the four points plotted in (a). In each subplot, the $\dot{V}_v = \dot{V}_m = 0$ nullcline [Eq. (4.15)] (solid) and $\dot{V}_v = \dot{V}_x = 0$ nullcline [Eq. (4.17)] (dot-dashed) intersect to give equilibriums of the model [i.e, solutions of Eq. (4.18)]: stable nodes (solid circles) or saddle points (open circles). Regions on the $\dot{V}_m = \dot{V}_v = 0$ nullcline for which $\dot{V} \approx \dot{V}_x < 0.001\,\mathrm{mV\,s^{-1}}$ are shaded dark gray, and $\dot{V}_x < 0.002\,\mathrm{mV\,s^{-1}}$ are shaded light gray.*

between psychological factors such as depression and sleep disorders and the sleep-wake cycle, which will be investigated in more detail in future work.

In Fig. 4.6(a), two trajectories are plotted that correspond to the two regimes considered in this paper: the dynamics of the system in response to a constant drive $D_x = 2\,\mathrm{mV}$ are studied in Sec. 4.5 [plotted as a dashed white line in Fig. 4.6(a)], and the dynamic circadian and homeostatic inputs to Orx, with $D_x = \nu_{xc}C + \nu_{xh}H + A_x$, are added in Sec. 4.6 [plotted as a solid white line in Fig. 4.6(a)].

4.5 Model Dynamics for a constant D_x

In this section, we average the time-dependent circadian and homeostatic inputs to Orx to a constant, intermediate level $D_x = 2\,\mathrm{mV}$, as was done in the original Phillips-Robinson model for D_m [1]. In this simplified regime, the basic features of the model can be more readily understood and compared to that of the original model. The next order of realism would involve setting $D_x = 0$ at night, due to an absence of behavioral or emotional stimuli. However, because Q_x is low during sleep due to inhibition from the VLPO, we leave D_x constant, resulting in qualitatively similar dynamics and aiding analysis in terms of the nullclines in the V_x–V_m plane.

4.5.1 Basic Dynamics

The model's outputs, including the firing rates Q_v, Q_m, and Q_x, the D_v–V_m plane projection, the drives D_v and D_x, and the V_x–V_m plane projection are shown in Figs 4.7(a)–(d), respectively. The model predicts periods of wake in which the MA and Orx are active and the VLPO is suppressed, and periods sleep in which the VLPO is active and the MA and Orx are suppressed. Instead of the constant drive A_m used in the original model, the drive to the MA is proportional to Q_x in the new model. The firing rate Q_x, and hence the

drive to the MA increases gradually from $\approx 0.2\,\mathrm{s}^{-1}$ to its waking level of $\approx 5.5\,\mathrm{s}^{-1}$ at the end of a sleep period and therefore exhibits a slower rate of onset compared to the constant drive of the original model. Thus the extended model predicts a slower transition from sleep to wake, a phenomenon well-known in the sleep literature as *sleep inertia* [59, 88, 102, 195, 196]. Sleep inertia describes how "immediately after awakening from sleep, alertness is low" [59] and its connection to the model's dynamics is elaborated upon in Sec. 4.5.3. As in the original Phillips-Robinson model, the D_v–V_m projection exhibits hysteresis and flip-flop dynamics, alternation between wake at low D_v and sleep at high D_v, but with a more gradual return to waking levels of arousal. The D_v variation is almost identical to that of the previous model (differing only because of slight changes in H dynamics).

4.5.2 The V_x–V_m plots

The nullclines $\dot{V}_v = \dot{V}_m = 0$ [Eq. (4.16)] and $\dot{V}_v = \dot{V}_x = 0$ [Eq. (4.17)] are plotted in Fig. 4.8(b)–(d), as a means of comparing the V_x–V_m representation of the model to the familiar D_v–D_m hysteresis loop representation developed in previous work [1]. At low D_v there is a single high-V_m 'wake' equilibrium [Fig. 4.8(b)], at high D_v there is a single sleep equilibrium [Fig. 4.8(d)], and at intermediate D_v two stable nodes and a saddle point exist [Fig. 4.8(c)]. This is the same qualitative behavior as that of in the original Phillips-Robinson model characterized in Chapter 2. However, as explained in Sec. 4.3.3, since $\tau_x \gg \tau_m, \tau_v$, the adiabatic dynamics occur along the $\dot{V}_m = \dot{V}_v = 0$ nullcline. The model therefore lags further behind the equilibrium prediction, as shown for the hysteresis loop plotted in Fig. 4.8(a). Crosses plotted in Fig. 4.8(b)–(d) represent the state of the system at each D_v, emphasizing this effect.

Focusing on regions of low $\dot{V} \approx \dot{V}_x$ plotted in Figs 4.8(b) and (d), we find that the wake ghost is preferentially stabilized over the sleep ghost, as a distinct

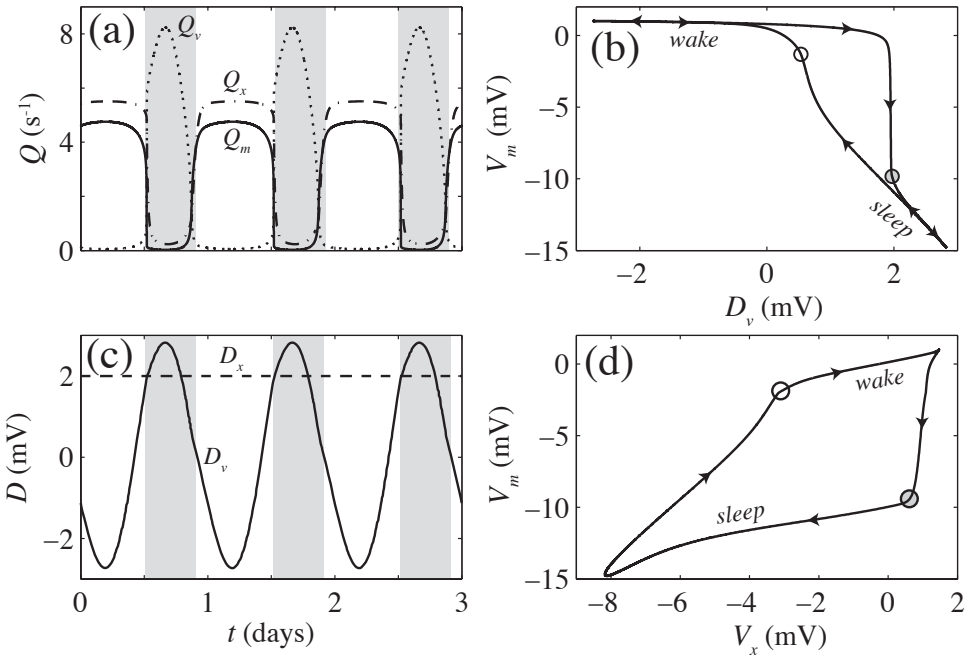

Figure 4.7: *Output of the model using a constant drive: $D_x = 2\,\mathrm{mV}$. (a) The firing rates Q_v (dotted), Q_m (solid), and Q_x (dot-dashed). (b) The hysteresis loop in the D_v–V_m projection. (c) The drives D_v (solid) and D_x (dashed). (d) The hysteresis loop in the V_x–V_m plane. In the time series plots (a) and (c), sleep periods are shaded. 'Wake' and 'sleep' are labeled in (b) and (d) and circles indicate the same point in both subplots, to demonstrate the correspondence between the two representations.*

region of near-stability at high D_v. Due to the curvature of the nullclines, the near-stable wake ghost region is separated from that surrounding the sleep node. Thus, the wake-sleep transition – when the system falls from the wake ghost to the sleep node – is rapid. In contrast, the sleep-wake transition is a continuous and gradual one, with the region of low $\dot{V}$ persisting throughout the change. It is this asymmetry that gives rise to the gradual sleep-wake transition (i.e., sleep inertia) in contrast to the abrupt wake-sleep transition (i.e., minimal 'wake inertia').

The nullcline representations shown in Figs 4.8(b)–(d), are akin to snap shots of the model at different drives D_v and D_x. Throughout this chapter, we

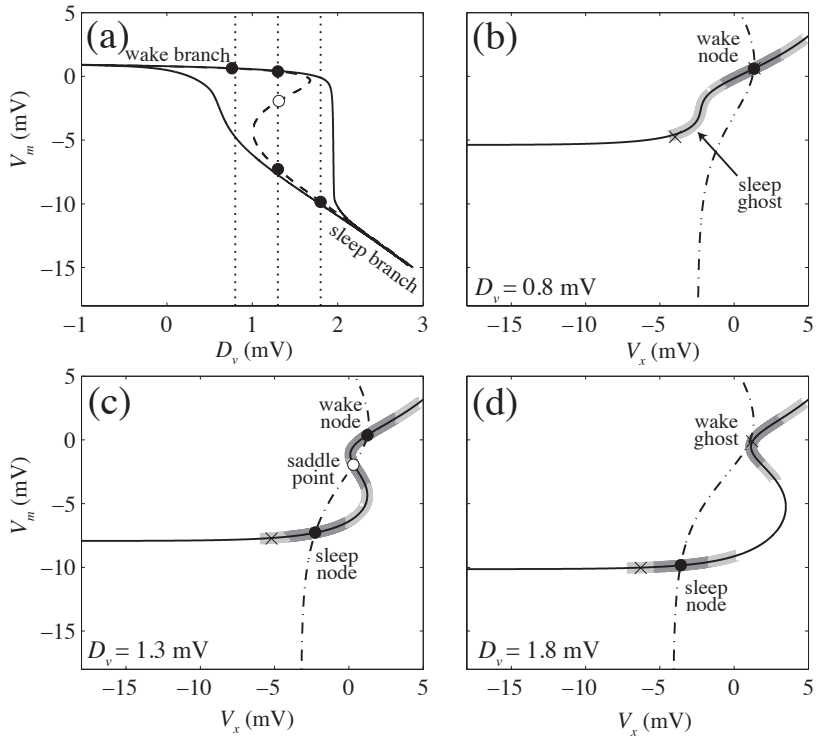

Figure 4.8: *Correspondence between the D_v–V_m hysteresis representation of the model and the projection onto the V_x–V_m plane for a constant orexinergic drive $D_x = 2\,\mathrm{mV}$. (a) The D_v–V_m hysteresis loop. The equilibrium curve is plotted with a dashed line and a model run using nominal parameters is plotted with a solid line. Lines of constant $D_v = 0.8\,\mathrm{mV}$, $1.3\,\mathrm{mV}$, and $1.8\,\mathrm{mV}$ [as in (b), (c), and (d), respectively] are plotted and the equilibriums are also shown: stable nodes (solid circles) and a saddle point (open circle). The remaining V_x–V_m plots include the $\dot{V}_v = \dot{V}_m = 0$ nullcline [Eq. (4.15)] (solid) and $\dot{V}_v = \dot{V}_x = 0$ nullcline [Eq. (4.17)] (dot-dashed), which intersect to give equilibriums, as labeled. At each drive, points corresponding to the model's output (which takes into account the nonzero time constants τ_i) are shown with crosses. Since $\tau_x \gg \tau_m, \tau_v$, the system remains close to the $\dot{V}_m = \dot{V}_v = 0$ nullcline, but not necessarily near the fixed points. Regions (on the $\dot{V}_v = \dot{V}_m = 0$ nullcline for which $\dot{V} \approx \dot{V}_x < 0.001\,\mathrm{mV\,s^{-1}}$ are shaded dark gray, and $\dot{V}_x < 0.002\,\mathrm{mV\,s^{-1}}$ light gray.*

will plot projections of the model's full output onto the V_x–V_m plane, as in Fig. 4.7(d), which exhibits hysteresis. At the wake-sleep transition, V_m decreases abruptly, with the decrease in V_x lagging behind it. However, both populations increase together during the sleep-wake transition because of the regions of low $\dot{V}$ in the V_x–V_m plane, as explained below.

4.5.3 Sleep Inertia

The time constant τ_x controls the characteristic time scale of the V_x dynamics and is therefore linked to the response time of the orexin group to relevant stimuli. In this section the impact of varying τ_x on the model's dynamics is explored. Since the dynamics of Orx mainly consist of alternating between a waking value ($Q_x \approx 5.5\,\mathrm{s}^{-1}$) and a sleeping value ($Q_x \approx 0.2\,\mathrm{s}^{-1}$), increasing τ_x slows the transitions between these two values. This is equivalent to introducing some 'lag' to the rate at which inputs to the orexin group are received. We speculate that this may be due to slower dynamics of the limbic system, for example, following extended rest. This correspondence allows us to interpret changes in τ_x in terms of the rate at which orexinergic inputs vary, rather than the neuromodulatory orexinergic dynamics themselves.

The wake-sleep transition is minimally affected by changes in τ_x because of the curvature of the nullclines plotted in Fig. 4.8(b)–(d), as explained above. The sleep-wake transition corresponds to decreasing D_v beyond the bifurcation point corresponding to the termination of the stable sleep branch. The $\dot{V}_v = \dot{V}_m = 0$ nullcline slowly straightens out, remaining close to the $\dot{V}_v = \dot{V}_x = 0$ nullcline and $\dot{V}$ remains small throughout the change. Hence decreasing τ_x decreases the rate of movement along the $\dot{V}_v = \dot{V}_m = 0$ nullcline, producing a more gradual sleep-wake transition. The wake-sleep transition remains rapid because the region of high $\dot{V}$ separating the wake ghost and the sleep node is robust to changes in τ_x; the system drops rapidly from the wake ghost to the sleep node.

The model's outputs for $\tau_x = 10\,\text{min}$, $30\,\text{min}$, and $120\,\text{min}$ are plotted in Fig. 4.9. In Fig. 4.9(c), the lag in Orx dynamics is demonstrated explicitly. However, the wake-sleep transitions in Q_m are largely unaffected by changes in τ_x whereas the sleep-wake transitions are highly sensitive to such changes. The sleep-wake transition is gradual, and its duration increases with τ_x. This effect can be seen in Fig. 4.9(a) from the time scale over which Q_m increases after a sleep period and in Fig. 4.9(b) from the shape of the sleep branch. Thus, increasing τ_x selectively tunes the time scale over which the sleep-wake transition occurs and hence the 'amount' of sleep inertia in the model. The model's equilibriums, the waking and sleeping arousal levels, and the wake-sleep transition rate, remain mostly unaltered. Hence τ_x can be constrained on behavioral grounds by the effect of sleep inertia, which rarely lasts more than $30\,\text{min}$ [195]. We reproduce this approximate time scale by choosing $\tau_x = 30\,\text{min}$.

Trajectories in the V_x–V_m plane, shown in Fig. 4.9(d), aid a dynamical interpretation of the nullcline pictures and will be used throughout this Chapter. Note that as τ_x decreases, the assumption that the system will be close to the $\dot{V}_v = \dot{V}_m = 0$ nullcline breaks down, and transitions between equilibriums are more rapid, being limited by a smaller τ_x, and occur along a more direct trajectory. However, as τ_x increases, the system's dynamics in V_x become even slower, and the system is given even more time to attract onto the $\dot{V}_v = \dot{V}_m = 0$ nullcline.

Previous sleep models, including the phenomenological 'three-process' model [6], included an additional empirical sleep inertia variable, as well as the homeostatic and circadian components of the 'two-process' model [56, 57]. Various implementations of the three-process model have been successful at predicting performance variation for a variety of protocols [58–60]. However, in contrast to the empirically-motivated inertia variable, sleep inertia has not been artificially imposed in our model, but results entirely from the model's physiologically-

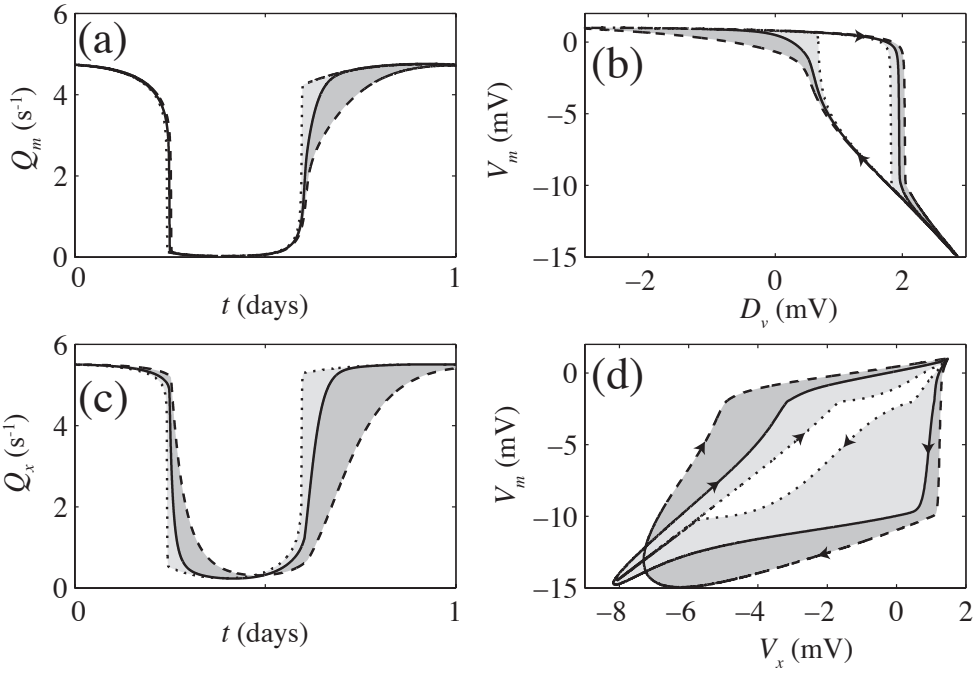

Figure 4.9: *Model dynamics as a function of the orexin time constant* $\tau_x = 10\,\text{min}$ *(dotted), nominal* $\tau_x = 30\,\text{min}$ *(solid), and* $\tau_x = 120\,\text{min}$ *(dashed). (a)* Q_m *time series. The wake-sleep transition is always rapid, but the sleep-wake transition slows with increased* τ_x*. (b)* D_v*–*V_m *hysteresis loops. (c)* Q_x *time series. (d)* V_x*–*V_m *hysteresis loops.*

justified formulation.

4.6 Dynamic Orexin Input

In the previous section, the key dynamical characteristics of the new model were demonstrated using a constant $D_x = 2\,\text{mV}$. In this section, the physiological effects of adenosine and the circadian signal are included as contributions to a dynamic orexinergic input $D_x = \nu_{xc}C + \nu_{xh}H + A_x$. In order to understand the impact of each of the dynamic drives, they are introduced individually: homeostatic input in Sec. 4.6.1, and circadian input in Sec. 4.6.2. The full model governed by Eq. (4.6), as justified in Sec. 4.2.3 and depicted schematically in Fig. 4.1, includes both homeostatic and circadian inputs, and is studied in Sec.

4.6.3. Since $Q_x \approx 0\,\mathrm{s}^{-1}$ during sleep, the dynamic D_x affects the waking firing rates Q_x and therefore modulates waking arousal levels, as inferred from Q_m.

4.6.1 Homeostatic Input

Adenosine inhibits the activity of Orx [185, 191], which we model using $D_x = \nu_{xh}H + A_x$ with $\nu_{xh} < 0$. The effect of changing the connection strength ν_{xh} is illustrated in Fig. 4.10, in which A_x has been adjusted in each case to retain the model's normal sleep length at 8.5 h. Since the homeostatic drive H is minimal at wake onset and maximal at sleep onset, the inhibitory drive $\nu_{xh}H$ to Orx skews the arousal curve towards high arousal in the morning and low arousal in the evening, as shown in Fig. 4.10(a). As the magnitude of the homeostatic input strength $|\nu_{xh}|$ increases, the arousal curve $Q_m(t)$ is increasingly skewed relative to normal.

The D_v–V_m hysteresis loop, shown in Fig. 4.10(c), distorts to a higher V_m at wake onset and to a lower V_m at sleep onset, decreasing the width of the hysteresis loop. This can be understood with reference to the D_v–D_x plane representation shown in Fig. 4.6(a). For dynamic drives D_x, the theoretical equilibrium D_v–V_m hysteresis loop width is the difference between the wake-sleep and sleep-wake D_v bifurcation values. Due to the shape of the bifurcation boundaries, increasing D_x near the sleep-wake transition (the left-most boundary) increases the lower D_v bifurcation value, and decreasing D_x near the wake-sleep transition (the right-most boundary) decreases the model's upper D_v bifurcation value. Hence the incorporation of an inhibitory drive $\nu_{xh}H$ to Orx decreases the extent of the bistable portion of the model's trajectory through D_v–D_x space, and hence the D_v–V_m hysteresis loop width.

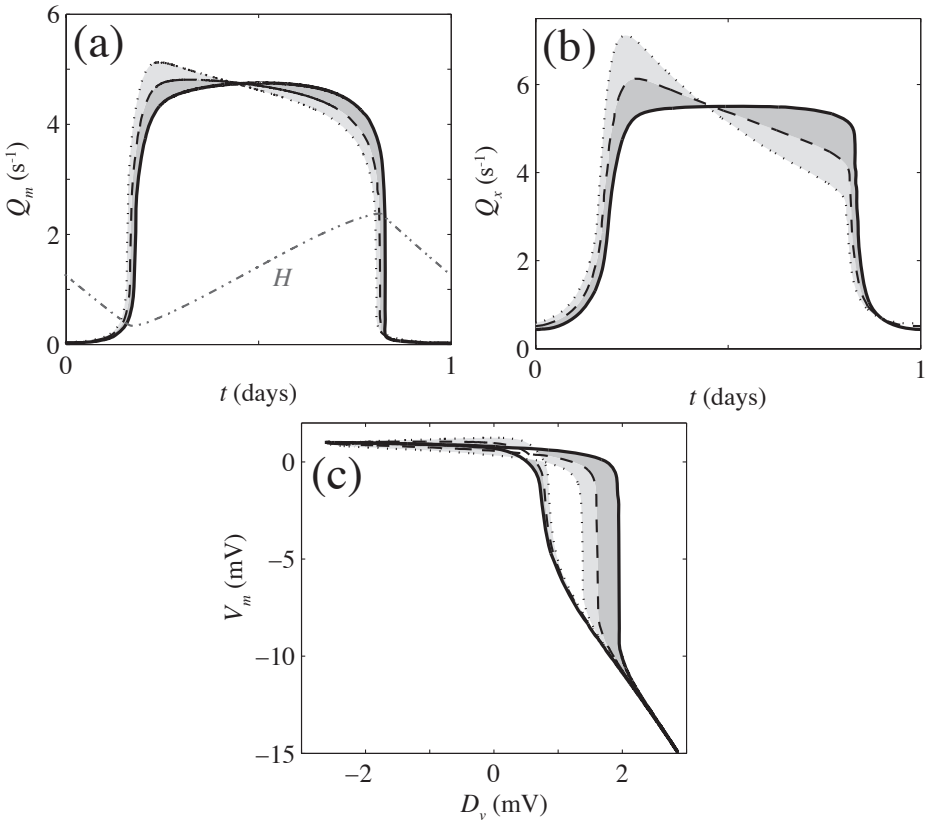

Figure 4.10: *Variation of the homeostatic coupling strength to the orexin group ν_{xh}. (a) Q_m time series. (b) Q_x time series. (c) The D_v–V_m hysteresis loop. In each subplot, the model output is shown for $\nu_{xh} = 0\,\mathrm{mV\,nM^{-1}}$, $A_x = 2\,\mathrm{mV}$ (solid line), $\nu_{xh} = -0.5\,\mathrm{mV\,nM^{-1}}$, $A_x = 8.5\,\mathrm{mV}$ (dashed line), and $\nu_{xh} = -1.0\,\mathrm{mV\,nM^{-1}}$, $A_x = 15\,\mathrm{mV}$ (dotted line). Changes in A_x have been chosen to retain the model's nominal sleep length at $8.5\,h$. Shading is used to emphasize the differences between the dynamics for each parameter set. The representative time course of the homeostatic drive H is plotted in (a) using an arbitrary vertical scale.*

4.6.2 Circadian Input

The orexin group receives input from the DMH, which itself receives a strong circadian projection from the SCN [53]. In this section we model the circadian input to the orexin group in isolation, using $D_x = \nu_{xc}C + A_x$. The connection ν_{xc} has previously been assumed to be excitatory [51, 53], implying that $\nu_{xc} > 0$. However, we investigate the behavioral impact of both excitatory ($\nu_{xc} > 0$) and inhibitory ($\nu_{xc} < 0$) projections.

In Fig. 4.11 the model's dynamics for $\nu_{xc} = +1.0\,\mathrm{mV}$ (excitatory) and $\nu_{xc} = -1.0\,\mathrm{mV}$ (inhibitory), and $\nu_{xc} = 0$ (no input) are compared. The arousal curve $Q_m(t)$ plotted in Fig. 4.11(a) shows that an excitatory connection $\nu_{xc} > 0$ increases the waking arousal level near the middle of the day when C is a maximum. The arousal level is reduced relative to normal predominantly during the morning, but also near sleep onset. On the other hand, an inhibitory connection $\nu_{xc} < 0$ increases relative arousal levels in the morning and evening, and yields a so-called 'postlunch dip' in performance, a well-known clinical phenomenon [4, 5, 103, 197]. The afternoon siesta constitutes a fundamental aspect of many cultures around the world [198]. Our modeling suggests that this is no coincidence: the physiological circadian connection ν_{xc} to the Orx (which relays to the MA) lowers arousal at this time, making it the most appropriate time for rest. That the postlunch dip is indeed an intrinsic behavioral feature, and not merely the result of food intake, is supported experimentally by studies showing that it persists even in the absence of a meal [197]. Since the post-lunch dip is produced in the model by a negative connection $\nu_{xc} < 0$, we use $\nu_{xc} = -1.0\,\mathrm{mV}$ for the remainder of this chapter.

The trends in the hysteresis loop width in Fig. 4.11(c) can be understood in terms of the drive space picture shown in Fig. 4.6(a). The sleep-wake transition occurs at the left-most bifurcation boundary in D_v–D_x space, which has a steep gradient and therefore is only relatively weakly dependent on D_x. The wake-sleep transition, on the other hand, given by the right-most bifurcation

boundary, has a shallower gradient and is therefore more sensitive to changes in D_x. In this case, increasing D_x near the morning and evening (i.e., with $\nu_{xm} < 0$) increases both D_v bifurcation values, but the increase in the wake-sleep value is greater. Similarly, decreasing D_x near the morning and evening (i.e., with $\nu_{xm} < 0$) decreases both D_v bifurcation values, but the wake-sleep bifurcation value decreases more markedly. These trends give rise to the behavior plotted in Fig. 4.11.

4.6.3 Circadian and Homeostatic Input

In this section we consider both circadian and homeostatic inputs together: $D_x = \nu_{xc}C + \nu_{xh}H + A_x$. The model's outputs, including the firing rates Q_v, Q_m, and Q_x, the D_v–V_m plane projection, the drives D_v and D_x, and the V_x–V_m plane projection are shown in Figs 4.12(a)–(d), respectively. The firing rates Q_v, Q_m, and Q_x shown in Fig. 4.12(a) are qualitatively similar to those obtained in Sec. 4.5 using a constant input $D_x = 2\,\mathrm{mV}$, exhibiting alternating periods of sleep and wake. However, Q_m and Q_x now vary during waking. The arousal-related variation $Q_m(t)$ combines aspects of both the homeostatic and circadian effects investigated separately above. Waking arousal rises gradually to an early-morning maximum, and decreases thereafter, with a postlunch dip in the mid-afternoon. It then levels off slightly, decreases toward the evening and then drops to sleep. The model's projection onto the D_v–V_m plane, as shown in Fig. 4.12(b), represents a modulation of the original Phillips-Robinson hysteresis loop, exhibiting a similar extent ($1\,\mathrm{mV} \lesssim D_v \lesssim 2\,\mathrm{mV}$) and topology, but with a dynamic waking V_m. The time series for D_v and D_x are shown in Fig. 4.12(c). Plotting the two drives against each other gives rise to the trajectory plotted in D_v–D_x space in Fig. 4.6(a). Finally, the shape of the V_x–V_m hysteresis curve plotted in Fig. 4.12(d) is similar to that obtained using a constant D_x plotted in Fig. 4.7(d), including the rapid wake-sleep transition

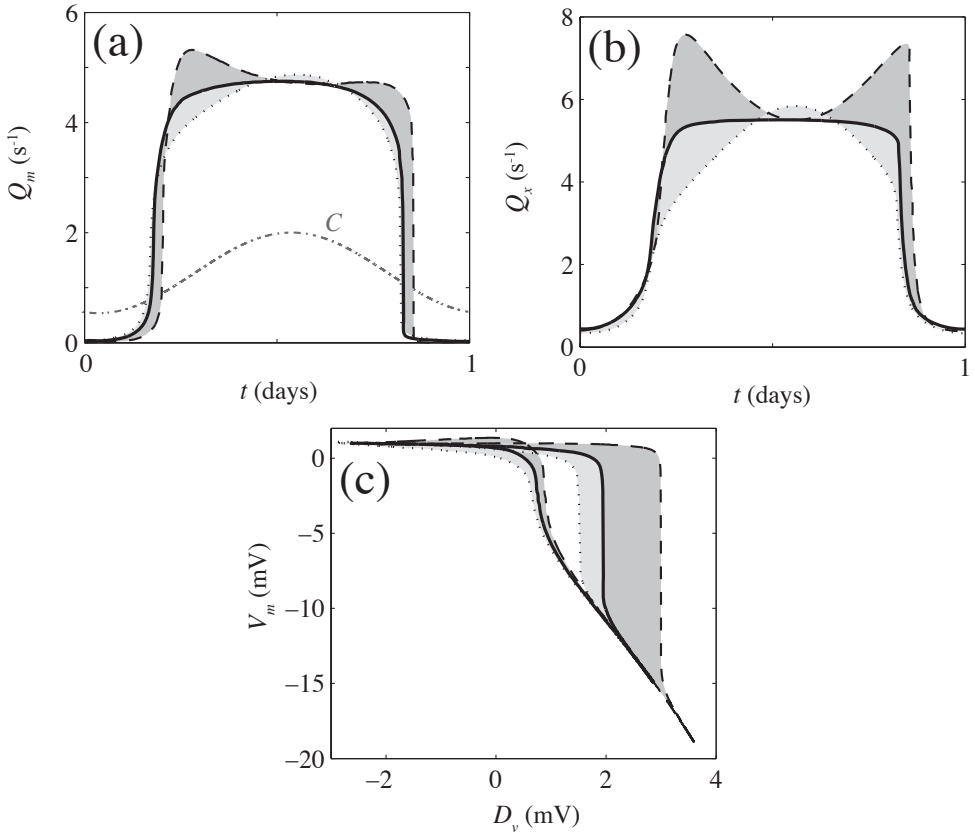

Figure 4.11: *The effect of adding circadian input to the orexin group via* $D_x = \nu_{xc}C + A_x$*. (a)* Q_m *time series. (b)* Q_x *time series. (c)* D_v*–*V_m *hysteresis loops. In each subplot, the model output is for* $\nu_{xc} = 0\,\mathrm{mV}$*,* $A_x = 2.0\,\mathrm{mV}$ *(solid line),* $\nu_{xc} = -1.0\,\mathrm{mV}$*,* $A_x = 3.0\,\mathrm{mV}$ *(dashed line and dark shading relative to* $\nu_{xc} = 0$*), and* $\nu_{xc} = +1.0\,\mathrm{mV}$*,* $A_x = 1.2\,\mathrm{mV}$ *(dotted line and light shading relative to* $\nu_{xc} = 0$*). The representative time course of the circadian drive* C *is plotted in (a) using an arbitrary vertical scale.*

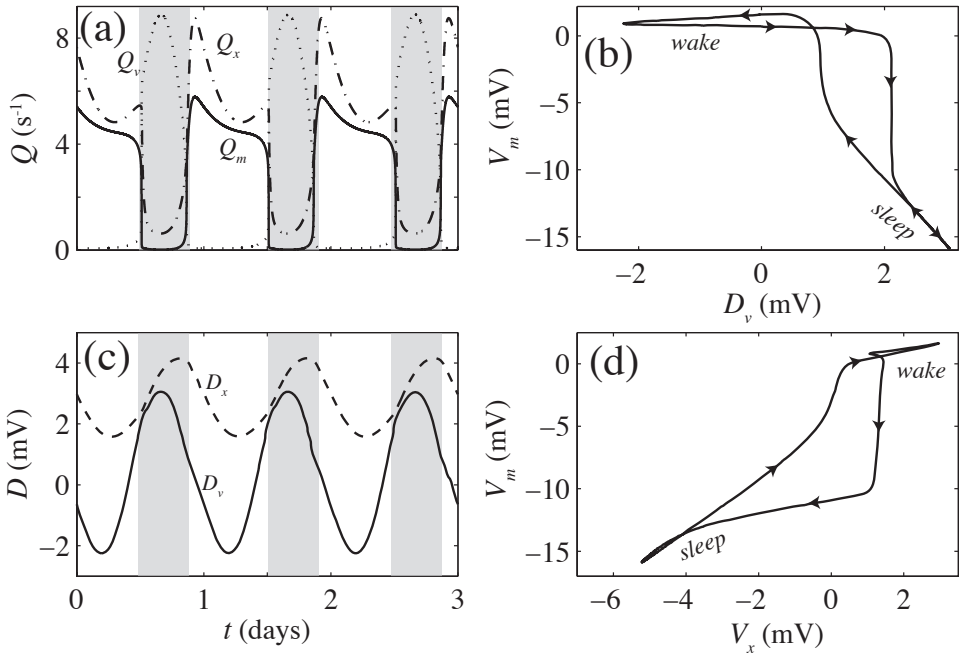

Figure 4.12: *Model output using a dynamic drive to the orexin group* $D_x = \nu_{xc}C + \nu_{xh}H + A_x$. *Nominal parameters are listed in Tab. 4.1. (a) The firing rates* Q_v *(dotted),* Q_m *(solid), and* Q_x *(dot-dashed),. (b) The* D_v*–*V_m *hysteresis loop. (c) Time series for the drives* D_v *(solid) and* D_x *(dashed). (d) The* V_x*–*V_m *hysteresis loop. Sleep periods are shaded in (a) and (c); 'wake' and 'sleep' are labeled in (b) and (d).*

and the more gradual sleep-wake transition.

The waking arousal variation $Q_m(t)$ shown in Fig. 4.12(a) matches performance curves obtained clinically. In his seminal book *Sleep and Wakefulness*, Kleitman described the prevalence of a morning rise and an afternoon decrease in performance variation data [104], a pattern that has since been observed clinically for alertness [5, 199], the multiple sleep latency test (MSLT) [197], and obtained from real-world data, including data on fatigue-related accidents [200]. Kleitman presented experimental performance variations for a range of tests: speed of card dealing, speed of card sorting, speed and accuracy of mirror drawing, speed and accuracy of code transcription, and speed and accuracy of multiplication [104]. The speed and accuracy results are plotted separately

in Figs 4.13(a) and (b), respectively. All the curves exhibit the same qualitative shape: increasing to a maximum in the early morning and then decreasing thereafter – identical to the qualitative trend of $Q_m(t)$ in our model. Since each task exhibits a different quantitative set of performance values (perhaps due to differences in their intrinsic interest, c.f., the performance model proposed in Chapter 3), the speed data (% relative to baseline) have been averaged at each time point across all of the tasks, and the same has been done for the accuracy data. Both the original curves and the averaged data set are plotted in Fig. 4.13. The Q_m variation over the same time interval has been scaled linearly to the data, and is plotted with a dashed line in Figs 4.13(a) and (b). Since the peak of performance speed occurs later than that of performance accuracy, the former data have been simulated by the model using an increased $\tau_x = 60\,\text{min}$. This delays the arousal peak, and produces a closer fit to the experimental data. As demonstrated in Sec. 4.5.3, τ_x selectively controls the amount of sleep inertia in the model. Thus we deduce that performance speed is more affected by sleep inertia than performance accuracy.

4.6.4 Narcolepsy

In this section, we model the sleep disorder narcolepsy, which is characterized by a neurodegenerative reduction in the number of orexinergic neurons relative to normal [177]. Since the firing rate Q_x of the orexin group appears in the model equations as a drive to the MA (via the term $\nu_{mx}Q_x$), the effective orexinergic output can be modified by changing ν_{mx}. The strength of the orexinergic drive, as determined by ν_{mx}, can thus be considered as a proxy for the number of orexinergic neurons in the LHA. When $\nu_{mx} = 0$, Orx dynamics do not affect the rest of the model.

The effect of reducing ν_{mx} is illustrated in Fig. 4.14, for $\nu_{mx} = 0.2\,\text{mV s}$ (nominal), $\nu_{mx} = 0.1\,\text{mV s}$ (a 50% reduction), and $\nu_{mx} = 0\,\text{mV s}$ (no orexinergic input whatever). As shown in Fig. 4.14(a), reducing ν_{mx} decreases waking

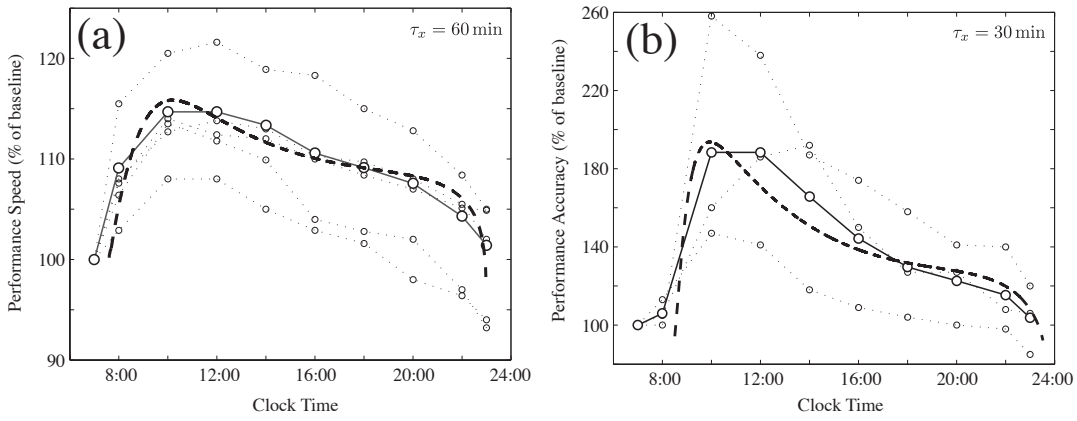

Figure 4.13: *Comparison of the model's output with clinical data sets reported by Kleitman [104]. In each plot, the original data sets are plotted with small open circles and a dotted line and the average of all the data sets with large open circles and a solid line, for (a) performance speed, and (b) performance accuracy in a range of tasks (see main text for descriptions). The model's output for Q_m (dashed line) is fitted linearly to the average data set using nominal model parameters. However, to simulate the performance speed data in subplot (a), a greater $\tau_x = 60\,\text{min}$ rather than the nominal $\tau_x = 30\,\text{min}$ has been used (i.e., performance speed is more affected by sleep inertia).*

arousal levels and decreases the depth of sleep (i.e., Q_m is higher during sleep). The D_v–V_m hysteresis loop, plotted in Fig. 4.14(b), exhibits the same qualitative changes in response to decreasing ν_{mx} as for decreasing A_m in the original Phillips-Robinson sleep model (c.f., Sec. 4.4.1) – waking arousal decreases and the hysteresis loop extent decreases until the flip-flop sleep-wake dynamics are reduced to continuous evolution. Since the characteristic Q_m variation (increasing to an early-morning peak and decreasing thereafter) is due to orexinergic projections, this also becomes less pronounced for lower ν_{mx}. Thus, in response to reducing ν_{mx}, the model's qualitative dynamics change in a way that is consistent with the two main characteristics of narcolepsy: reduced waking arousal and a decreased threshold for transitions between sleep and wake [48] (c.f., the discussion at the end of Sec. 4.4.1). Projections of the model's output onto the V_x–V_m plane are plotted in Fig. 4.14(d). The curves retain their basic shape,

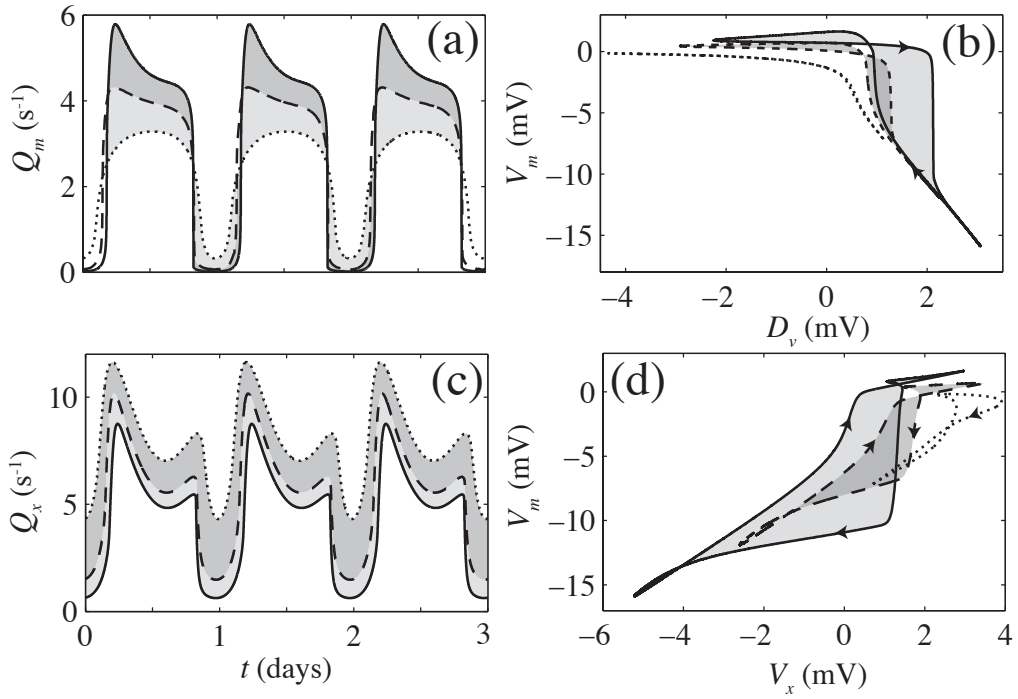

Figure 4.14: *The model's sensitivity to orexinergic input $\nu_{mx}Q_x$ to the MA. Each plot shows the model's output as a function of the connection ν_{mx}: for its nominal value $\nu_{mx} = 0.2\,\mathrm{mV\,s}$ (solid), a 50% reduction $\nu_{mx} = 0.1\,\mathrm{mV\,s}$ (dashed), and for no connection whatever $\nu_{mx} = 0\,\mathrm{mV\,s}$ (dotted). (a) Q_m time series. (b) D_v–V_m hysteresis loops. (c) Q_x time series. (d) V_x–V_m hysteresis loops. Shading is used to highlight the differences between the plots.*

but become smaller and shift to higher V_x and lower V_m.

Interestingly, as $|\nu_{mx}|$ decreases, the Orx firing rate Q_x increases, as shown in Fig. 4.14(c). This is because the waking Q_m decreases with decreasing ν_{mx}, decreasing the Orx inhibition from the MA. This suggests an allostatic mechanism (i.e., a process of achieving stability in response to some external change) that partially compensates for small losses of orexinergic neurons in the LHA. Due to this feedback mechanism, the model predicts a nonlinear relationship between narcoleptic symptoms and loss of orexinergic neurons. This could be quantified in future work to determine the exact relationship (e.g., initially slow, due to allostatic compensation, but then more rapid), yielding insights into the critical level of loss that triggers the onset of significant narcoleptic symptoms.

The model does not reproduce the increased sleep-wake transition frequency that is characteristic of narcoleptic patients. However we propose that, because of the reduced bistable extent, the addition of random perturbations into the system via noisy drives $\boldsymbol{\Delta D}$ should reproduce this effect. Such drives correspond to noisy external stimuli. However, the addition of noise into the system is beyond the scope of the current work, and will be investigated in the future. For now, we simply note the qualitative agreement of the changes to the model due to a reduction in orexinergic input via ν_{mx}.

4.7 Summary and Discussion

We have developed a quantitative, physiologically-based approach to modeling arousal state dynamics which includes the orexinergic neurons of the LHA. Using the same modeling approach as the Phillips-Robinson model, the Orx population was introduced, as well as established neuronal interactions and circadian and homeostatic inputs. The succinct representation of the system in matrix notation facilitated a linear stability analysis and a separation of model time scales, allowing us to develop a representation of the model in the reduced

V_x–V_m subspace in terms of the $\dot{V}_v = \dot{V}_m = 0$ and $\dot{V}_v = \dot{V}_x = 0$ nullclines. Assuming that the drives are slowly-varying and can thus be treated as control parameters, the system can be considered to be close to equilibrium on time scales $\gg \max(\tau_i)$. Using this approximation, an equilibrium representation of the original Phillips-Robinson model in D_v–D_m space was first developed and used to explain both the impact of arbitrary external perturbations (ΔD_v, ΔD_m) and, in particular, the result of introducing a dynamic drive D_m to the model, as is done here for the orexinergic drive $\nu_{mx} Q_x$ to the MA. The model's structure changes in a way that is qualitatively consistent with narcoleptic symptoms when the mean orexinergic drive to the MA is reduced, including a decreased threshold for transitions between wake and sleep and lower waking arousal levels. A representation of the extended model in the D_v–D_x plane was then used to demonstrate the main features of the new model. The dynamical analysis performed in Sec. 4.3 facilitated a representation of the model in the reduced V_x–V_m subspace, in which the model's dynamics were characterized in terms of the adiabatic dynamics along the $\dot{V}_v = \dot{V}_m = 0$ nullcline and localized regions of low $\dot{V}$.

After this general characterization of the model, the rest of the chapter focused on the numerical output of the model, its dependences upon the various model parameters, and predictions of clinical relevance. In Sec. 4.5, the drive D_x was simplified to a constant level $D_x = 2\,\mathrm{mV}$ to demonstrate the main features of the new model in the absence of the complications of a time varying drive D_x. The asymmetry between the wake-sleep and sleep-wake transitions was explained in terms of the topology of the nullclines in the V_x–V_m plane, and sleep inertia was shown to depend directly on the characteristic rate of orexinergic dynamics, τ_x. In Sec. 4.6, the circadian and homeostatic inputs to the orexin group were explicitly included into the model. Inhibition from adenosine was shown to skew arousal towards the morning and the sign of the circadian coupling ν_{xc} was shown to alter the arousal time series to either exhibit a postlunch dip ($\nu_{xc} < 0$), or to peak in the middle of the day ($\nu_{xc} > 0$).

Consistent with the clinical ubiquity of the postlunch dip, we proposed that $\nu_{xc} < 0$ and then modeled both homeostatic and circadian inputs to Orx. The resulting arousal time series exhibited excellent quantitative agreement with clinical performance speed and accuracy curves. Reducing the orexinergic input to the MA was shown to produce the same qualitative features as narcolepsy.

To recapitulate, the main results of this chapter are as follows: (i) the orexin group was incorporated into a physiologically-based sleep model and its dynamics have been characterized in detail, (ii) a general framework for representing arbitrary slowly-varying drives to the model was introduced, (iii) the time constant for orexin dynamics τ_x selectively gives rise to sleep inertia, (iv) a net inhibitory circadian connection to the orexin group gives rise to a postlunch dip in arousal levels, (v) incorporating both circadian and adenosine-mediated inhibition of the orexin group yields a daytime arousal variation that quantitatively matches experimental data, (vi) the relative amounts of sleep inertia in different performance tasks can be inferred from the model, and (vi) the model was applied to narcolepsy, yielding qualitative changes consistent with narcoleptic symptoms. This is the first time that physiological causes of well known clinical features including sleep inertia (τ_x), the postlunch dip ($\nu_{xc} < 0$), and performance/arousal time series ($\nu_{xc}, \nu_{xh} < 0$) have been postulated, all in the same physiologically-justified model.

The most significant result of this chapter has been the demonstration that the variation in waking arousal is consistent with the combination of homeostatic and circadian drives to the orexin group. Models such as the 'three-process' model [6, 60, 61] for predicting vigilance and performance have been created previously. However, unlike the homeostatic and circadian drives, which are based on physiological processes, the sleep inertia component of the three-process model is an empirically-introduced variable that aims to improve the model's agreement with data. Furthermore, the physiological mechanisms of the homeostatic and circadian drives are not included. For example, the three-process alertness model proposed by Achermann and Borbély [60] uses

complicated numerically-fitted phenomenological functions with large numbers of parameters, including an 'inertia' function I that is artificially pulsed at transitions between wake and sleep (note that we use I for the inertia variable rather than the W used in the original paper to distinguish it from the unrelated wake-effort drive introduced in Chapter 2). Where the two-process model uses $S - C$ to indicate fatigue (c.f., Sec. 1.4.2), alertness in this three-process model is given by $1 - S + C - I$: an intuitively reasonable, but otherwise unjustified combination of the homeostatic (S), circadian (C), and inertial (W) drives. In our model, on the other hand, the known physiology is targeted directly and sleep inertia is shown to result specifically from the time constant τ_x of the orexin dynamics – i.e., it does not need to be artificially introduced. How H and C act physiologically to give rise to the predicted patterns is also clear. In addition, the characteristic variation of waking performance, including a rise in the morning and a postlunch dip, was reproduced. This was not done through empirical fitting, but using a modest number of physiological (e.g., mean firing rates and the inhibition/excitation of their interactions) and behavioral (e.g., sleep length) constraints. Because of the model's physiological formulation, physiological studies can be used to provide evidence for or against the model's predictions. In particular, the postlunch dip in our model results from a net inhibitory connection from the circadian drive to the MA (i.e., inhibition to the Orx and excitation from the Orx to the MA), the same sign as that from C to the VLPO. An existing physiological study [53] has implicated an excitatory connection from C to Orx. More detailed studies may shed light on the feasibility of the theory presented here. It may be, for example, that the circadian projection to Orx is indeed excitatory, but that the MA receives an additional circadian input from other sources that more than compensates, giving a net inhibition. Future clinical studies could also compare groups of subjects with different homeostatic dynamics (inferred from EEG SWA) and also different circadian phases and amplitudes (inferred from the body temperature oscillation). The current model would then distinguish

the performance curves in terms of changes in circadian amplitude and homeostatic drive strength, in a similar way to that demonstrated for the wake-effort drive curves in Sec. 3.3.4. Thus the proposed model is open to scrutiny from both clinical and physiological experimentation.

There is much scope for future improvements and further applications of the above model. The new parameters used here have been constrained by both physiology and behavior (c.f., Sec. 4.2.4). However, a more rigorous constraining process, like that performed for the original Phillips-Robinson model [1, 81], is a possible avenue for future work. Narcoleptics have disrupted ultradian dynamics, often falling straight into REM sleep, and have highly-fragmented sleep-wake cycles [100, 111]. Since the model averages over ultradian dynamics and does not include noisy external drives, neither of these features have been reproduced in this chapter, and remain targets for future work.

The current model also neglects the effect of additional inputs to the Orx group. As mentioned above, Orx receives numerous external inputs, particularly from the limbic system [111], which could be modeled in the future by adding a time dependent drive $\Delta D_x(t)$ to Orx. Since the orexin group accentuates the wake ghost (c.f., Sec. 4.5.1), another avenue for further research would involve comparing the system's response to impulsive sensory stimuli to that of the original Phillips-Robinson model, studied in Chapter 2. In the context of the performance model proposed in Sec. 3.5.3, the current model is able to determine the orexinergic input during sleep deprivation and may therefore be able to distinguish the necessary cortical component to the wake-effort W drive. A quantification of this drive may elucidate the role of the orexin group in stabilizing the waking state, reducing the cortical input required to maintain wakefulness during sleep deprivation. Combined with a 'motivational' input $\Delta D_x(t)$, the model may also be able to simulate performance variation for monotonous tasks/protocols (i.e., low motivation, low ΔD_x) compared to those for complex, more interesting tasks/protocols (i.e., higher motivation, increased ΔD_x).

Chapter 5

Concluding Remarks

The research presented in this thesis has rich potential for application and further development. In this chapter, we briefly discuss the implications of the research presented in Chapter 2–4, including natural avenues for future research. First, in Sec. 5.1, the main results of the thesis are examined, with brief reference to specific applications. In Sec. 5.2, avenues for future work are elaborated, taking into account the new developments made in this thesis as a whole.

5.1 General Outlook

The research presented in this thesis demonstrates the strengths of quantitative physiologically-based sleep modeling in providing a rigorous framework in which to interpret sleep-wake dynamics. We have demonstrated the versatility of the physiologically-based modeling approach, including its advantages over phenomenological methodologies. The approach involves three main components: (i) mathematical formulation of established physiology, (ii) dynamical analysis of the governing equations, and (iii) verifying connections between the model's output and corresponding behavioral and psychological responses. The research presented in Chapter 2 demonstrates correspondences between these

three processes most clearly: the dynamical analysis of the model's equations, in terms of the V_v–V_m plane projection (including the invariant manifolds, bifurcations, and ghosts) yields results that are directly interpretable in terms of the arousal state responses that they imply. In Chapter 3, it is the existence of the wake ghost that motivates the concept of wake-effort as an additional drive to maintain wakefulness, an approach with numerous and highly significant practical applications. In Chapter 4, the dynamic properties of the system in terms of regions of low $\dot{V}$ surrounding the $\dot{V}_v = \dot{V}_m = 0$ nullcline in the V_x–V_m plane are used to determine the mechanisms that produce the transition asymmetry that leads to sleep inertia. Unique to this approach is the ability to link rigorous mathematical analysis of the physiological interactions to clinically-relevant predictions. It is the simplicity of the Phillips-Robinson model, in focusing on the fundamental MA–VLPO system, that allows a conceptually tractable understanding of the dynamics, and also facilitates much of the dynamical analysis, which in most cases can be performed analytically. These qualities distinguish the Phillips-Robinson model from more complicated neural network models, which contain many free parameters and have limited analytic utility.

Establishing a quantitative framework that allows diverse concepts and influences to be unified and compared on a single scale has been a key achievement of this thesis. For example, representing drives as two-dimensional $\Delta\mathbf{D} = (\Delta D_v, \Delta D_m)$ vectors allows pharmaceutical, physiological, and sensory influences alike to be compared in terms of the relative effects of their mechanisms on the VLPO and MA nuclei. In addition, intuitive clinical labels such as 'alertness', 'compensatory effort', 'resource-limiting factors', 'fatigue', and 'feeling' can be expressed more precisely in terms of the mathematically-defined physiological model quantities, such as the sleep drive D and wake-effort W variables. This potential for unifying a range of seemingly disparate quantities distinguishes the physiologically-based approach, as has been well substantiated in this thesis.

5.2 Future Directions

As mentioned above, incorporating external drives into the model using the $\Delta\mathbf{D}$ vector representation is expected to facilitate further modeling in the future and, in particular, the impact of pharmaceuticals on sleep-wake dynamics. The knowledge of a given pharmaceutical's mechanism can be used to deduce its relative effect on the MA and VLPO nuclei and hence allows the construction of a $\Delta\mathbf{D}(t)$ vector. For slowly-varying drives, trajectories in drive-space (c.f., Chapter 4) can be used to explore the basic qualitative effects; for impulsive drives, trajectories through V_v–V_m space are appropriate (c.f., Chapter 2). Whatever the time scale over which $\Delta\mathbf{D}(t)$ varies, its impact can be determined by integrating the model's equations. In this way, changes in sleep latency, sleep length, arousal, the homeostatic drive, and other measurable quantities can be predicted. Such quantities can be calculated as a function of the time of intake of the drug, its concentration, and its pharmacokinetic properties. A number of drugs, including caffeine, modafinil, anesthetics, and alcohol are expected to be modeled in this way in the future, for diverse applications in arousal modulation and control. Once calibrated, the model would be able to simulate clinical protocols involving arbitrary intake schedules of the given pharmaceutical, whilst incorporating previously studied effects such as sleep deprivation. For example, the impact of different pharmaceuticals on the wake-effort time series studied in Chapter 3 could easily be determined, thereby allowing a comparison of their relative effectiveness in combating fatigue during sleep deprivation. Indeed, the optimum intake schedule could potentially be calculated and applied, with great significance for shift workers. Plotting trajectories $\Delta\mathbf{D}(t)$ for disparate external influences may also aid the construction of a pharmaceutical *basis set* to facilitate arbitrary arousal state modulation by exploiting various combinations of such influences. Realization of this more speculative goal could then be applied clinically, predicting effective therapies involving combinations of drugs, for example.

The rationale and method for predicting fatigue, as proposed in Chapter 3 for the case of total sleep deprivation, could routinely be extended to other sleep restriction protocols. The model's W drive, which we have demonstrated to correlate with subjective fatigue-related measures, is nonzero for D greater than its value at the saddle-node bifurcation of the stable wake node [c.f., Fig. 3.5(b)]. The variation in fatigue could be calculated following sleep fragmentation or sleep apnea/restless legs syndromes (which increase D due to the increased homeostatic impact of frequent nocturnal disturbances, c.f., Sec. 2.5.3), or as a result of chronic sleep reduction protocols [24, 26, 27]. Combined with a pharmaceutical analysis along the lines of that mentioned above, this research could help suggest suitable pharmacological treatments for sleep apnea or restless legs syndrome patients, for example. Given the success of the physiologically-based approach in elucidating the wake-effort drive and its clinical correspondences, we argue that much progress can be made in the future by calculating W time series for arbitrary sleep-wake schedules and determining the impact of arbitrary external drives $\Delta\mathbf{D}$ and parameter changes.

In this thesis, we have demonstrated the potential of continuum neuronal population-based modeling to produce clinically-relevant output. However, there is much more work to be done in this direction. In particular, a systematic way of calibrating the model's parameters to individuals may help to elucidate the physiological cause of inter-individual differences in sleep-wake dynamics, including behavioral responses to different clinical protocols. A calibration of this type would also allow individual-specific predictions to be made, rather than simply suggesting group-averaged dynamics, as considered in the current work. Realizing this goal would prove especially useful for suggesting treatments for sleep pathologies such as insomnia, sleep apnea, and narcolepsy, as well as guiding the sleep-wake schedules for normal subjects, including recovery from sleep deprivation, optimum napping schedules, and predicting optimum recovery from jet-lag. Individual pharmacokinetic measurements could also guide optimum intake schedules, both as treatment for symptomatic excessive

daytime sleepiness, and for optimizing performance for a given application.

As demonstrated in Chapter 4 for the orexin group, the continuum neuronal population modeling methodology used in the original Phillips-Robinson model is easily extended to incorporate additional neuronal populations, drives, and interconnections. The same method could be applied to other nuclei in the future, including the ACh group, for example, which may contribute to ultradian dynamics, an effect not yet produced by the model. In addition, when exploring sleep-wake dynamics in more detail, it may become necessary to delineate the individual components of the MA group: the TMN, LC, DR, and VTA, as separate neuronal components. This is expected to be useful for modeling the mechanisms of pharmaceuticals or for understanding cataplexy, during which the activity of individual MA nuclei is uncoordinated [201–203]. Such developments will give a progressively more detailed picture of sleep-wake dynamics. However, with the addition of each neuronal population, new parameters are added to the model: one for every new interaction and input drive, ν, and a time constant τ. Thus, unless the physiology is sufficiently well known to constrain these parameters, attempts to include such populations into a physiologically-based model are *ad hoc*. Furthermore, including additional populations is at the expense of both the conceptual simplicity and analytic utility of the model. We therefore suggest that, although the addition of the Orx group in Chapter 4 produced a number of interesting and clinically-significant results, continuing down this path of adding neuronal populations to the model is not the most fruitful direction at this stage. In the future, perhaps in collaboration with physiologists, it will be important to extend the model in size and complexity, but we argue that the simplicity of the sleep model and its ability to produce rich and significant output should be exploited as far as possible before such extensions are attempted.

Much of the work presented in this thesis has been validated by demonstrating agreement with clinical data sets – including the arousal threshold variation in Chapter 2, the fatigue curves in Chapter 3, and the performance

curves in Chapter 4. However, for many of the predictions of the model, comparative data is not yet available. These include the critical sleep latencies $\mathcal{T}$ in Chapter 2 and the dependences of the W time series on the drive parameters presented in Chapter 3, which await clinical verification. Also, the sign of the circadian projection through the orexin group to the MA, deduced from behavioral constraints in Chapter 4, could be corroborated through physiological investigations. There is therefore extensive potential for close collaboration with both physiologists and clinicians in the future.

In conclusion, the research presented in this thesis represents some of the early stages in the life of physiologically-based sleep modeling. While still in its infancy compared to phenomenological sleep models, the physiologically-based approach is shown to be extremely powerful and versatile, with immediate potential for gaining new insights into sleep-wake dynamics and the mechanisms that govern them. Given the recent progress of physiological knowledge, the current work demonstrates that moving beyond the phenomenological approach of sleep modeling is an achievable task with great potential. Future developments in the directions outlined above are expected to be particularly fruitful in guiding progress in the wider sleep research field.

Bibliography

[1] A. J. K. Phillips and P. A. Robinson. A quantitative model of sleep-wake dynamics based on the physiology of the brainstem ascending arousal system. *J. Biol. Rhythms*, 22:167–179, 2007.

[2] M. A. Carskadon and W. C. Dement. Normal human sleep: An overview. In M. H. Kyger, T. Roth, and W. C. Dement, editors, *Principles and Practice of Sleep Medicine*, chapter 2, pages 15–25. WB Saunders, Philadelphia, Third edition, 2000.

[3] H. Berger. Ueber das elektroenkephalogramm des menschen. *J. Psychol. Neurol.*, 40:160–179, 1930.

[4] T. H. Monk, D. J. Buysse, C. Reynolds III, S. Berga, D. Jarrett, A. Begley, and D. Kupfer. Circadian rhythms in human performance and mood under constant conditions. *J. Sleep Res.*, 6(1):9–18, 1997.

[5] J. Carrier and T. H. Monk. Circadian Rhythms of Performance: New Trends. *Chronobiol. Int.*, 17:719–732, 2000.

[6] S. Folkard and T. Akerstedt. *Contemporary Advances in Shiftwork Research: Theoretical and Practical Aspects in the Late Eighties*, pages 231–240. Medical Academy, Krakow, Poland, 1987.

[7] T. Akerstedt. Altered sleep/wake patterns and mental performance. *Physiol. Behav.*, 90(2-3):209–218, 2007.

[8] A. Reinberg and I. Ashkenazi. Internal desynchronization of circadian rhythms and tolerance to shift work. *Chronobiol. Int.*, 25(4):625–643, 2008.

[9] H. O De La Iglesia, T. Cambras, and A. Diez-Noguera. Circadian internal desynchronization: Lessons from a rat. *Sleep Biol. Rhythms*, 6:79–83, 2008.

[10] S. Fujiwara, S. Shinkai, Y. Kurokawa, and T. Watanabe. The acute effects of experimental short-term evening and night shifts on human circadian rhythm: the oral temperature, heart rate, serum cortisol and urinary catecholamines levels. *Int. Arch. Occup. Environ. Health*, 63:407–418, 1992.

[11] I. Tankova, A. Adan, and G. Buela-Casal. Circadian typology and individual differences. A review. *Pers. Individ. Dif.*, 16(5):671–684, 1994.

[12] R. O. Pasnau, P. Naitoh, S. Stier, and E. J. Kollar. The psychological effects of 205 hours of sleep deprivation. *Arch. Gen. Psychiat.*, 18:496–505, 1968.

[13] J. A. Horne, N. R. Anderson, and R. T. Wilkinson. Effects of sleep deprivation on signal detection measures of vigilance: Implications for sleep function. *Sleep*, 6(4):347–358, 1983.

[14] J. A. Horne and A. N. Pettitt. High incentive effects on vigilance performance during 72 hours of total sleep deprivation. *Acta Psychologica*, 58 (2):123–139, 1985.

[15] E. J. Kollar, R. O. Pasnau, R. T. Rubin, P. Naitoh, G. G. Slater, and A. Kales. Psychological, psychophysiological, and biochemical correlates of prolonged sleep deprivation. *Am. J. Psychiatry*, 126(4):488–497, 1969.

[16] M. H. Bonnet and D. L. Arand. Clinical effects of sleep fragmentation versus sleep deprivation. *Sleep Med. Rev.*, 7:297–310, 2003.

[17] M. H. Bonnet. Effect of sleep disruption on sleep, performance, and mood. *Sleep*, 8:11–19, 1985.

[18] E. J. Stepanski. The effect of sleep fragmentation on daytime function. *Sleep*, 25:268–276, 2002.

[19] N. J. Wesensten, T. J. Balkin, and G. Belenky. Does sleep fragmentation impact recuperation? a review and reanalysis. *J. Sleep Res.*, 8:237–245, 1999.

[20] M. H. Bonnet. Performance and sleepiness as a function of frequency and placement of sleep disruption. *Psychophysiology*, 23:263–271, 1986.

[21] B. Levine, T. Roehrs, E. Stepanski, F. Zorick, and T. Roth. Fragmenting Sleep Diminishes Its Recuperative Value. *Sleep*, 10(6):590–599, 1987.

[22] S. E. Martin, P. E. Brander, I. J. Deary, and N. J. Douglas. The effect of clustered versus regular sleep fragmentation on daytime function. *J. Sleep Res.*, 8:305–311, 1999.

[23] H. P. A. Van Dongen, G. Maislin, J. M. Mullington, and D. F. Dinges. The cumulative cost of additional wakefulness: Dose-response effects on neurobehavioral functions and sleep physiology from chronic sleep restriction and total sleep deprivation. *Sleep*, 26:117–126, 2003.

[24] D. J. Mullaney, L. C. Johnson, P. Naitoh, J. K. Friedmann, and G. G. Globus. Sleep During and After Gradual Sleep Reduction. *Psychophysiology*, 14(3):237–244, 1977.

[25] J. Friedmann, G. Globus, A. Huntley, D. Mullaney, P. Naitoh, and L. Johnson. Performance and mood during and after gradual sleep reduction. *Psychophysiology*, 14(3):245–250, 1977.

[26] W. B. Webb and H. W. Agnew. Sleep: Effects of a restricted regime. *Science*, 150(3704):1745–1747, 1965.

[27] W. B. Webb and H. W. Agnew. The effects of a chronic limitation of sleep length. *Psychophysiology*, 11(3):265–274, 1974.

[28] R. E. Kronauer, C. A. Czeisler, S. F. Pilato, M. C. Morre-Ede, and E. D. Weitzman. Mathematical model of the human circadian system with two interacting oscillators. *Am. J. Physiol. Regul. Integr. Comp. Physiol.*, 242:3–17, 1982.

[29] D. J. Dijk, D. G. M. Beersma, S. Daan, and A. J. Lewy. Bright morning light advances the human circadian system without affecting NREM sleep homeostasis. *Am. J. Physiol. Regul. Integr. Comp. Physiol.*, 256:106–111, 1989.

[30] E. B. Klerman, D. Dijk, R. E. Kronauer, and C. A. Czeisler. Simulations of light effects on the human circadian pacemaker: implications for assessment of intrinsic period. *Am. J. Physiol. Regul. Integr. Comp. Physiol.*, 270:271–282, 1996.

[31] RA Webster. *Neurotransmitters, Drugs and Brain Function.* Wiley, Chichester, 2002.

[32] J. R. L. Schwartz. Pharmacologic management of daytime sleepiness. *J. Clin. Psychiatry*, 65:46–49, 2004.

[33] B. Boutrel and G. F. Koob. What Keeps Us Awake: the Neuropharmacology of Stimulants and Wakefulness-Promoting Medications. *Sleep*, 27: 1181–1194, 2004.

[34] E. Szabadi. Drugs for sleep disorders: mechanisms and therapeutic prospects. *Br. J. Clin. Pharmacol.*, 61:761–766, 2006.

[35] F. Magkos and S. A. Kavouras. Caffeine use in sports, pharmacokinetics in man, and cellular mechanisms of action. *Crit. Rev. Food Sci. Nutr.*, 45:535–562, 2005.

[36] J. K. Walsh, A. C. Randazzo, K. L. Stone, and P. K. Schweitzer. Modafinil Improves Alertness, Vigilance, and Executive Function During Simulated Night Shifts. *Sleep*, 27(3):434–439, 2004.

[37] J. S. Ballon and D. Feifel. A systematic review of modafinil: Potential clinical uses and mechanisms of action. *J. Clin. Psychiatry*, 67:554–566, 2006.

[38] E. Hennevin, C. Huetz, and J. Edeline. Neural representations during sleep: From sensory processing to memory traces. *Neurobiol. Learn. Mem.*, 87:416–440, 2007.

[39] D. P. White. Central sleep apnea. In M. H. Kryger, T. Roth, and W. C. Dement, editors, *Principles and Practice of Sleep Medicine*, chapter 71, pages 827–839. WB Saunders, Philadelphia, Third edition, 2000.

[40] T. Young, P. E. Peppard, and D. J. Gottlieb. Epidemiology of obstructive sleep apnea. *Am. J. Respir. Crit. Care Med.*, 165:1217–1239, 2002.

[41] A. Malhotra and D. P. White. Obstructive sleep apnoea. *The Lancet*, 360:237–245, 2002.

[42] R. B. Berry and K. Gleeson. Respiratory Arousal From Sleep: Mechanisms and Significance. *Sleep*, 20:654–675, 1997.

[43] A. G. Bassiri and C. Guilleminault. Clinical features and evaluation of obstructive sleep apnea-hypopnea syndrome. In M.H. Kyger, T. Roth, and W.C. Dement, editors, *Principles and Practice of Sleep Medicine*, chapter 74, pages 869–878. WB Saunders, Philadelphia, Third edition, 2000.

[44] M. Younes. Role of Arousals in the Pathogenesis of Obstructive Sleep Apnea. *Am. J. Crit. Care Med.*, 169:623–633, 2004.

[45] C. M. Ryan and T. D. Bradley. Pathogenesis of obstructive sleep apnea. *J. Appl. Physiol.*, 99:2440–2450, 2005.

[46] C. J. Earley. Restless legs syndrome. *N. Engl. J. Med.*, 348:2103–2109, 2003.

[47] J. K. Walsh. Pharmacologic management of insomnia. *J. Clin. Psychiatry*, 65:41–45, 2004.

[48] S. Nishino. Clinical and neurobiological aspects of narcolepsy. *Sleep Med.*, 8:373–399, 2007.

[49] T. Gallopin, P. Fort, E. Eggermann, B. Cauli, P. H. Luppi, J. Rossier, E. Audinat, M. Mühlethaler, and M. Serafin. Identification of sleep-promoting neurons *in vitro*. *Nature*, 404(6781):992–5, 2000.

[50] E. F. Pace-Schott and J. A. Hobson. The neurobiology of sleep: Genetics, cellular physiology and subcortical networks. *Nat. Rev. Neurosci.*, 3:591–605, 2002.

[51] C. B. Saper, T. E. Scammell, and J. Lu. Hypothalamic regulation of sleep and circadian rhythms. *Nature*, 437:1257–1263, 2005.

[52] K. Yoshida, S. McCormack, A. Rodrigo, A. Crocker, and T. E. Scammell. Afferents to the Orexin Neurons of the Rat Brain. *J Comp. Neurol.*, 494: 845–861, 2006.

[53] T. C. Chou, T. E. Scammell, J. J. Gooley, S. E. Gaus, C. B. Saper, and J. Lu. Critical role of dorsomedial hypothalamic nucleus in a wide range of behavioral circadian rhythms. *J. Neurosci.*, 23:10691–10702, 2003.

[54] T. C. Chou, A. A. Bjorkum, S. E. Gaus, J. Lu, T. E. Scammell, and C. B. Saper. Afferents to the Ventrolateral Preoptic Nucleus. *J. Neurosci.*, 22: 977–990, 2002.

[55] G. Aston-Jones, S. Chen, Y. Zhu, and M. L. Oshinsky. A neural circuit for circadian regulation of arousal. *Nat. Neurosci.*, 4:732–738, 2001.

[56] A. A. Borbély. A two process model of sleep regulation. *Hum. Neurobiol.*, 1:195–204, 1982.

[57] S. Daan, D. G. M. Beersma, and A. A. Borbély. Timing of human sleep: recovery process gated by a circadian pacemaker. *Am. J. Physiol. Regul. Integr. Comp. Physiol.*, 246:161–183, 1984.

[58] A. A. Borbély and P. Achermann. Sleep Homeostasis and Models of Sleep Regulation. *J. Biol. Rhythms*, 14(6):557–568, 1999.

[59] A. Gundel, K. Marsalek, and C. Thoren. A critical review of existing mathematical models for alertness. *Somnologie*, 11:148–156, 2007.

[60] P. Achermann and A. A. Borbély. Simulation of daytime vigilance by the additive interaction of a homeostatic and a circadian process. *Biol. Cybern.*, 71(2):115–121, 1994.

[61] T. Akerstedt and S. Folkard. Validation of the s and c components of the three-process model of alertness regulation. *Sleep*, 18(1):1–6, 1995.

[62] T. C. Chou. *Regulation of Sleep-Wake Timing: Circadian Rhythms and Bistability of Sleep-Wake States*. PhD thesis, Cambridge, MA: Harvard University, 2003.

[63] Y. Tamakawa, A. Karashima, Y. Koyama, N. Katayama, and M. Nakao. A quartet neural system model orchestrating sleep and wakefulness mechanisms. *J. Neurophysiol.*, 95:2055–2069, 2006.

[64] C. G. Diniz Behn, E. N. Brown, T. E. Scammell, and N. J. Kopell. Mathematical model of network dynamics governing mouse sleep-wake behavior. *J. Neurophysiol.*, 97:3828–3840, 2007.

[65] Van M. Savage and Geoffrey B. West. A quantitative, theoretical framework for understanding mammalian sleep. *Proc. Natl. Acad. Sci. USA*, 104(3):1051–1056, 2007.

[66] R. G. Foster and K. Wulff. The rhythm of rest and excess. *Nat. Rev. Neurosci.*, 6:407–414, 2005.

[67] W. C. Dement and M. M. Mitler. It's time to wake up to the importance of sleep disorders. *JAMA*, 269(12):1548–1550, 1993.

[68] R. J. Thomas and K. Kwong. Modafinil activates cortical and subcortical sites in the sleep-deprived state. *Sleep*, 29:1471–1481, 2006.

[69] J. A. Hobson and E. F. Pace-Schott. The cognitive neuroscience of sleep: Neuronal systems, consciousness and learning. *Nat. Rev. Neurosci.*, 3: 679–693, 2002.

[70] T. Akerstedt and M. Gillberg. Effects of sleep deprivation on memory and sleep latencies in connection with repeated awakenings from sleep. *Psychophysiology*, 16(1):49–52, 1979.

[71] Y. Harrison and J. A. Horne. The impact of sleep deprivation on decision making: A review. *J. Exp. Psychol.: Appl.*, 6:236–249, 2000.

[72] A. A. Borbély, Fritz Baumann, Daniel Brandeis, Inge Strauch, and Dietrich Lehmann. Sleep deprivation: Effect on sleep stages and EEG power density in man. *Electroencephalogr. Clin. Neurophysiol.*, 51(5):483–493, 1981.

[73] P. Achermann, D. Dijk, D. P. Brunner, and A. A. Borbély. A Model of Human Sleep Homeostasis Based on EEG Slow-Wave Activity: Quantitative Comparison of Data and Simulations. *Brain Res. Bull.*, 31:97–113, 1993.

[74] S. Folkard and T. Akerstedt. *Sleep, Arousal, and Performance: A three-process model of the regulation of alertness-sleepiness*, pages 11–26. Birkhäuser, Boston, 1992.

[75] M. Nakao, A. Karashima, and N. Katayama. Mathematical models of regulatory mechanisms of sleep-wake rhythms. *Cell. Mol. Life Sci.*, 64: 1236–1243, 2007.

[76] H. P. A. Van Dongen. Comparison of mathematical model predictions to experimental data of fatigue and performance. *Aviat. Space Environ. Med.*, 75:A15–A36, 2004.

[77] A. A. Borbély and P. Achermann. Sleep homeostasis and models of sleep regulation. In M.H. Kyger, T. Roth, and W.C. Dement, editors, *Principles and Practice of Sleep Medicine*, chapter 29, pages 377–390. WB Saunders, Philadelphia, Third edition, 2000.

[78] J. E. Sherin, P. J. Shiromani, R. W. McCarley, and C. B. Saper. Activation of Ventrolateral Preoptic Neurons During Sleep. *Science*, 271: 216–219, 1996.

[79] C. B. Saper, T. C. Chou, and T. E. Scammell. The sleep switch: hypothalamic control of sleep and wakefulness. *Trends Neurosci.*, 24:726–731, 2001.

[80] D. McGinty and R. Szymusiak. The sleep-wake switch: A neuronal alarm clock. *Nat. Med.*, 6(5):510–511, 2000.

[81] A. J. K. Phillips and P. A. Robinson. Application of a quantitative physiologically-based model of the ascending arousal system to sleep deprivation. *J. Theor. Biol.*, accepted for publication, 2008.

[82] W. J. Freeman. *Mass Action in the Nervous System.* Academic Press, New York, 1975.

[83] P. L. Nunez. *Neocortical Dynamics and Human EEG Rhythms*. Oxford University Press, New York, 1995.

[84] P. A. Robinson, C. J. Rennie, and J. J. Wright. Propagation and stability of waves of electrical activity in the cerebral cortex. *Phys. Rev. E*, 56(1): 826–840, 1997.

[85] P. A. Robinson, C. J. Rennie, D. L. Rowe, and S. C. O'Connor. Estimation of multiscale neurophysiologic parameters by electroencephalographic means. *Hum. Brain Mapp.*, 23:53–72, 2004.

[86] P. A. Robinson, C. J. Rennie, D. L. Rowe, S. C. O'Connor, and E. Gordon. Multiscale brain modelling. *Phil. Trans. R. Soc. B*, 360:1043–1050, 2005.

[87] S. S. von Albada and P. A. Robinson. unpublished work, 2008.

[88] M. E. Jewett, D. B. Forger, and R. E. Kronauer. Revised limit cycle oscillator model of human circadian pacemaker. *J. Biol. Rhythms*, 14(6): 493–499, 1999.

[89] C. A. Czeisler and E. N. Brown. Models of the effect of light on the human circadian system: Current state of the art. *J. Biol. Rhythms*, 14 (6):539–543, 1999.

[90] J. M. Gregory, X. Xie, and S. A. Mengel. Sleep (sleep loss effects on everyday performance) model. *Aviat. Space Environ. Med.*, 75:A125–133, 2004.

[91] H. Babkoff, T. Caspy, and M. Mikulincer. Monotonic and rhythmic influences: A challenge for sleep deprivation research. *Psychol. Bull.*, 109 (3):411–428, 1991.

[92] T. Sakurai, A. Amemiya, M. Ishii, I. Matsuzaki, R. M. Chemelli, H. Tanaka, S. C. Williams, J. A. Richardson, G. P. Kozlowski, S. Wil-

son, J. R. S. Arch, R. E. Buckingham, A. C. Haynes, S. A. Carr, R. S. Annan, D. E. McNulty, W. Liu, J. A. Terrett, N. A. Elshourbagy, D. J. Bergsma, and M. Yanagisawa. Orexins and Orexin Receptors: A Family of Hypothalamic Neuropeptides and G Protein-Coupled Receptors that Regulate Feeding Behavior. *Cell*, 92:573–585, 1998.

[93] L. de Lecea, T. S. Kilduff, C. Peyron, X. Gao, P. E. Foye, P. E. Danielson, C. Fukuhara, E. L. F. Battenberg, V. T. Gautvik, F. S. Bartlett, W. N. Frankel, A. N. van den Pol, F. E. Bloom, K. M. Gautvik, and J. G. Sutcliffe. The hypocretins: Hypothalamus-specific peptides with neuroexcitatory activity. *Proc. Natl. Acad. Sci. USA*, 95:322–327, 1998.

[94] O. Selbach and H. L. Haas. Hypocretins: The Timing of Sleep and Waking. *Chronobiol. Int.*, 23:63–70, 2006.

[95] R. M. Chemelli, J. T. Willie, C. M. Sinton, J. K. Elmquist, T. E. Scammell, C. Lee, J. A. Richardson, S. C. Williams, Y. Xiong, Y. Kisanuki, T. E. Fitch, M. Nakazato, R. E. Hammer, C. B. Saper, and M. Yanagisawa. Narcolepsy in orexin Knockout Mice: Molecular Genetics of Sleep Regulation. *Cell*, 98:437–451, 1999.

[96] T. C. Thannickal, R. Y. Moore, R. Nienhuis, L. Ramanathan, S. Gulyani, M. Aldrich, M. Cornford, and J. M. Siegel. Reduced number of hypocretin neurons in human narcolepsy. *Neuron*, 27:469–474, 2000.

[97] C. Peyron, J. Faraco, W. Rogers, B. Ripley, S. Overeem, Y. Charnay, S. Nevsimalova, M. Aldrich, D. Reynolds, R. Albin, R. Li, M. Hungs, M. Pedrazzoli, M. Padigaru, M. Kucherlapati, J. Fan, R. Maki, G. J. Lammers, C. Bouras, R. Kucherlapati, S. Nishino, and E. Mignot. A mutation in a case of early onset narcolepsy and a generalized absence of hypocretin peptides in human narcoleptic brains. *Nat. Med.*, 6:991–997, 2000.

[98] R. Fronczek, H. A. M. Middelkoop, J. G. van Dijk, and G. J. Lammers. Focusing on vigilance instead of sleepiness in the assessment of narcolepsy: High sensitivity of the sustained attention to response task (sart). *Sleep*, 29:187–191, 2006.

[99] M. Hungs and E. Mignot. Hypocretin/orexin, sleep and narcolepsy. *Bioessays*, 23:387–408, 2001.

[100] T. E. Scammell. The Neurobiology, Diagnosis, and Treatment of Narcolepsy. *Ann. Neurol.*, 53:154–166, 2003.

[101] M. E. Jewett and R. E. Kronauer. Interactive mathematical models of subjective alertness and cognitive throughput in humans. *J. Biol. Rhythms*, 14(6):588–597, 1999.

[102] A. Lubin, D. J. Hord, M. L. Tracy, and L. C. Johnson. Effects of exercise, bedrest and napping on perforamnce decrement during 40 hours. *Psychophysiology*, 13(4):334–339, 1976.

[103] T. H. Monk, D. J. Buysse, C. F. Reynolds III, and D. J. Kupfer. Circadian determinants of the postlunch dip in performance. *Chronobiol. Int.*, 13 (2):123–133, 1996.

[104] N. Kleitman. *Sleep and Wakefulness*. University of Chicago Press, 1963.

[105] R. E. Strecker, S. Morairty, M. M. Thakkar, T. Porkka-Heiskanen, R. Basheer, L. J. Dauphin, D. G. Rainnie, C. M. Portas, R. W. Greene, and R. W. McCarley. Adenosinergic modulation of basal forebrain and preoptic/anterior hypothalamic neuronal activity in the control of behavioral state. *Behav. Brain Res.*, 115:183–204, 2000.

[106] E. R. Kandel, J. H. Schwartz, and T. M. Jessell. *Principles of Neural Science*. McGraw-Hill, New York, Fourth edition, 1991.

[107] B. E. Jones. Basic mechanisms of sleep-wake states. In M. H. Kyger, T. Roth, and W. C. Dement, editors, *Principles and Practice of Sleep Medicine*, chapter 10, pages 134–154. WB Saunders, Philadelphia, Third edition, 2000.

[108] G. Aston-Jones, C. Chiang, and T. Alexinsky. Discharge of noradrenergic locus coeruleus neurons in behaving rats and monkeys suggests a role in vigilance. *Prog. Brain. Res.*, 88:501–520, 1991.

[109] A. I. Levey, A. E. Hallanger, and B. H. Wainer. Cholinergic nucleus basalis neurons may influence the cortex via the thalamus. *Neurosci. Lett.*, 74:7–13, 1987.

[110] M. M. Thakkar, R. E. Strecker, and R. W. McCarley. Behavioral state control through differential serotonergic inhibition in the mesopontine cholinergic nuclei: A simultaneous unit recording and microdialysis study. *J. Neurosci.*, 18(14):5490–5497, 1998.

[111] T. Sakurai. The neural circuit of orexin (hypocretin): maintaining sleep and wakefulness. *Nat. Rev. Neurosci.*, 8:171–181, 2007.

[112] K. Ohno and T. Sakurai. Orexin neuronal circuitry: Role in the regulation of sleep and wakefulness. *Front. Neuroendocrinol.*, 29:70–87, 2008.

[113] J. J. Gooley, A. Schomer, and C. B. Saper. The dorsomedial hypothalamic nucleus is critical for the expression of food-entrainable circadian rhythms. *Nature Neurosci.*, 9(3):398–407, 2006.

[114] T. Porkka-Heiskanen, R. E. Strecker, M. M. Thakkar, A. A. Bjørkum, R. W. Greene, and R. W. McCarley. Adenosine: A mediator of the sleep-inducing effects of prolonged wakefulness. *Science*, 276:1265–1268, 1997.

[115] J. T. McKenna, L. J. Dauphin, K. J. Mulkern, A. M. Stronge, R. W. McCarley, and R. E. Strecker. Nocturnal Elevation of Extracellular Adenosine in the Rat Basal Forebrain. *Sleep Res. Online*, 5(155–160), 2003.

[116] M. Dworak, P. Diel, S. Voss, W. Hollmann, and H. K. Strüder. Intense exercise increases adenosine concentrations in rat brain: implications for a homeostatic sleep drive. *Neuroscience*, 150:789–795, 2007.

[117] M. Díaz-Muńoz, R. Hernández-Muńoz, J. Suárez, S. Vidrio, L. Yáńez, R. Aguilar-Roblero, A. Oksenberg, L. Rosenthal, L. Villalobos, F. Fernández-Cancino, R. Drucker-Colín, and V. C. de Sánchez. Correlation between blood adenosine metabolism and sleep in humans. *Sleep Res. Online*, 2:33–41, 1999.

[118] C. W. Berridge and B. D. Waterhouse. The locus coeruleus-noradrenergic system: modulation of behavioral state and state-dependent cognitive processes. *Brain Res. Rev.*, 42:33–84, 2003.

[119] D. G. Rainnie, H. C. Grunze, R. W. McCarley, and R. W. Greene. Adenosine inhibition of mesopontine cholinergic neurons: implications for EEG arousal. *Science*, 263:689–692, 1994.

[120] C. K. R. T. Jones. In R. Johnson, editor, *Geometric Singular Perturbation Theory (Lecture Notes in Mathematics vol 1609)*. New York: Springer, 1995.

[121] S. H. Strogatz. *Nonlinear Dynamics and Chaos: With Applications to Physics, Biology, Chemistry, and Engineering.* Westview Press, 1994.

[122] J. Guckenheimer and P. Holmes. *Nonlinear Oscillations, Dynamical Systems, and Bifurcations of Vector Fields*, chapter 1. Springer-Verlag, 1983.

[123] Glendinning. *Stability, Instability, and Chaos*, chapter 4. Cambridge University Press, 1994.

[124] ASDA Report. EEG Arousals: Scoring Rules and Examples. *Sleep*, 15 (2):173–184, 1992.

[125] P. Halasz, M. Terzano, L. Parrino, and R. Bodizs. The nature of arousal in sleep. *J. Sleep Res.*, 13(1):1–23, 2004.

[126] C. Lo, T. Chou, T. Penzel, T. E. Scammell, R. E. Strecker, H. E. Stanley, and P. Ch. Ivanov. Common scale-invariant patterns of sleep-wake transitions across mammalian species. *Proc. Natl. Acad. Sci. USA*, 101 (50):17545–17548, 2004.

[127] J. Rajkowski, P. Kubiak, and G. Aston-Jones. Locus coeruleus activity in monkey: Phasic and tonic changes are associated with altered vigilance. *Brain Res. Bull.*, 35(5/6):607–616, 1994.

[128] Y. Koyama, E. Joko, and Y. Kayama. Sensory responsiveness of "broad-spike" neurons in the laterodorsal tegmental nucleus, locus coeruleus and dorsal raphé of awake rats: implications for cholinergic and monoaminergic neuron-specific responses. *Neuroscience*, 63(4):1021–1031, 1994.

[129] B. Y. Mileykovskiy, L. I. Kiyashchenko, and J. M. Siegel. Behavioral correlates of activity in identified hypocretin/orexin neurons. *Neuron*, 46 (5):787–798, 2005.

[130] K. Takahashi, J. S. Lin, and K. Sakai. Neuronal activity of orexin and non-orexin waking-active neurons during wake-sleep states in the mouse. *Neuroscience*, 153(3):860–870, 2008.

[131] N. B. Reese, E. Garcia-Rill, and R. D. Skinner. The pedunculopontine nucleus–auditory input, arousal and pathophysiology. *Prog. Neurobiol.*, 47(2):105–133, 1995.

[132] B. E. Jones and H. H. Webster. Neurotoxic lesions of the dorsolateral pontomesencephalic tegmentum-cholinergic cell area in the cat. I. Effects

upon the cholinergic innervation of the brain. *Brain Res.*, 451(1-2):13–32, 1988.

[133] M. H. Bonnet, L. C. Johnson, and W. B. Webb. The Reliability of Arousal Threshold During Sleep. *Psychophysiology*, 15(5):412–416, 1978.

[134] M. H. Bonnet, W. B. Webb, and G. Barnard. Effect of Flurazepam, Pentobarbital, and Caffeine on Arousal Threshold. *Sleep*, 1:271–279, 1979.

[135] M. H. Bonnet. Infrequent periodic sleep disruption: Effects on sleep, performance and mood. *Physiol. Behav.*, 45:1049–1055, 1989.

[136] W. J. Lammers, P. Badia, R. Hughes, and J. Harsh. Temperature, time-of-night of testing, and responsiveness to stimuli presented while sleeping. *Psychophysiology*, 28(4):463–467, 1991.

[137] W. J. Lammers and P. Badia. Motor responsiveness to stimuli presented during sleep: The influence of time-of-testing on sleep stage analyses. *Physiol. Behav.*, 50(4):867–868, 1991.

[138] W. B. Zimmerman. Sleep mentation and auditory awakening thresholds. *Psychophysiology*, 6(5):540–549, 1970.

[139] F. B. Keefe, L. C. Johnson, and E. J. Hunter. EEG and Autonomic Response Pattern During Waking and Sleep Stages. *Psychophysiology*, 8 (2):198–212, 1971.

[140] M. Bonnet. *Biological Rhythms, Sleep, and Performance*, chapter 8: Performance during Sleep. Wiley, 1982.

[141] R. A. Wever. *The Circadian System of Man.* Springer-Verlag, 1979.

[142] R. L. Horner. Motor control of the pharyngeal musculature and implications for the pathogenesis of obstructive sleep apnea. *Sleep*, 19:827–853, 1996.

[143] V. B. Fenik, R. O. Davies, and L. Kubin. REM Sleep-like Atonia of Hypoglossal (XII) Motoneurons Is Caused by Loss of Noradrenergic and Serotonergic Inputs. *Am. J. Respir. Crit. Care Med.*, 172:1322–1330, 2005.

[144] E. Sforza, J. Krieger, and C. Petiau. Arousal Threshold to Respiratory Stimuli in OSA Patients: Evidence for a Sleep-dependent Temporal Rhythm. *Sleep*, 22:69–75, 1999.

[145] R. B. Berry, M. A. Asyali, M. I. McNellis, and M. C. K. Khoo. Within-night variation in respiratory effort preceding apnea termination and EEG delta power in sleep apnea. *J. Appl. Physiol.*, 85:1434–1441, 1998.

[146] T. E. Scammell and C. B. Saper. Orexin, drugs and motivated behaviors. *Nature Neurosci.*, 8:1286–1288, 2005.

[147] T. Sakurai, R. Nagata, A. Yamanaka, H. Kawamura, N. Tsujino, Y. Muraki, H. Kageyama, S. Kunita, S. Takahashi, K. Goto, Y. Koyama, S. Shioda, and M. Yanagisawa. Input of orexin/hypocretin neurons revealed by a genetically encoded tracer in mice. *Neuron*, 46:297–308, 2005.

[148] Y. Yoshida, N. Fujiki, T. Nakajima, B. Ripley, H. Matsumura, H. Yoneda, E. Mignot, and S. Nishino. Fluctuation of extracellular hypocretin-1 (orexin A) levels in the rat in relation to the light–dark cycle and sleep–wake activities. *Eur. J. Neurosci.*, 14:1075–1081, 2001.

[149] T. Akerstedt and J. E. Fröberg. Psychophysiological circadian rhythms in women during 72 h of sleep deprivation. *Waking Sleeping*, 1:387–394, 1977.

[150] J. E. Fröberg, C. Karisson, L. Levi, and L. Lidberg. Circadian rhythms of catecholamine excretion, shooting range performance and self-ratings of fatigue during sleep deprivation. *Biol. Psychol.*, 2:175–188, 1975.

[151] D. G. M. Beersma and M. C. M. Gordijn. Circadian control of the sleep-wake cycle. *Physiol. Behav.*, 90:190–195, 2007.

[152] M. Mikulincer, H. Babkoff, and T. Caspy. The effects of 72 hours of sleep loss on psychological variables. *Br. J. Psychol.*, 80:145–162, 1989.

[153] R. J. Heslegrave and R. G. Angus. The effects of task duration and work-session location on performance degredation induced by sleep loss and sustained cognitive work. *Behav. Res. Methods Instrum. Comput.*, 17(6):592–603, 1985.

[154] R. G. Angus and R. J. Heslegrave. Effects of sleep loss on sustained cognitive performance during a command and control simulation. *Behav. Res. Methods Instrum. Comput.*, 17(1):55–67, 1985.

[155] H. Babkoff, S. G. Genser, H. C. Sing, D. R. Thorne, and F. W. Hegge. The effects of progressive sleep loss on a lexical decision task: Response lapses and response accuracy. *Behav. Res. Methods Instrum. Comput.*, 17(6):614–622, 1985.

[156] T. Akerstedt, J. E. Fröberg, Y. Friberg, and L. Wetterberg. Melatonin excretion, body temperature and subjective arousal during 64 hours of sleep deprivation. *Psychoneuroendocrinology*, 4(3):219–225, 1979.

[157] J. E. Fröberg. Twenty-four-hour patterns in human performance, subjective and physiological variables and differences between morning and evening active subjects. *Biol. Psychol.*, 5(2):119–134, 1977.

[158] E. Kuhn and V. Brodan. Changes in the circadian rhythm of serum iron induced by a 5-day sleep deprivation. *Eur. J. Appl. Physiol.*, 49(2): 215–222, 1982.

[159] P. Achermann and A. A. Borbély. Mathematical models of sleep regulation. *Front. Biosci.*, 8:683–693, 2003.

[160] M. M. Mallis, S. Mejdal, T. T. Nguyen, and D. F. Dinges. Summary of the key features of seven biomathematical models of human fatigue and performance. *Aviat. Space Environ. Med.*, 75:A4–A14, 2004.

[161] T. E. Scammell and C. B. Saper. Orexins: looking forward to sleep, back at addiction. *Nat. Med.*, 13:126–128, 2007.

[162] T. Akerstedt and M. Gillberg. Circadian variation of catecholamine excretion and sleep. *Eur. J. Appl. Physiol.*, 51(2):203–210, 1983.

[163] M. W. Eysenck. *Attention and Arousal*. Springer-Verlag, New York, 1982.

[164] T. A. Ryan, C. L. Cottrell, and M. E. Bitterman. Muscular tension as an index of effort: The effect of glare and other disturbances in visual work. *Am. J. Psychol.*, 63:317–341, 1950.

[165] R. T. Wilkinson. Muscle tension during mental work under sleep deprivation. *J. Exp. Psychol.*, 64(6):565–571, 1962.

[166] J. F. O'Hanlon. Boredom: Practical consequences and a theory. *Acta Psychologica*, 49(1):53–82, 1981.

[167] J. May and P. Kline. Measuring the effect upon cognitive abilities of sleep loss during continuous operations. *Br. J. Psychol.*, 78:443–455, 1987.

[168] E. A. Alluisi and W. D. Chiles. Sustained performance, work-rest scheduling, and diurnal rhythms in man. *Acta Psychologica*, 27:436–442, 1967.

[169] H. Babkoff, M. Mikulincer, T. Caspy, D. Kempinski, and H. Sing. The topology of performance curves during 72 hours of sleep loss: A memory and search task. *Q. J. Exp. Psychol. A*, 40(4):737–756, 1988.

[170] F. P. M. Kruijver and D. F. Swaab. Sex hormone receptors are present in the human suprachiasmatic nucleus. *Neuroendocrinology*, 75(5):296–305, 2001.

[171] E. Iwahana, I. Karatsoreos, S. Shibata, and R. Silver. Gonadectomy reveals sex differences in circadian rhythms and suprachiasmatic nucleus androgen receptors in mice. *Horm. Behav.*, 53(3):422–430, 2008.

[172] F. C. Baker and H. S. Driver. Circadian rhythms, sleep, and the menstrual cycle. *Sleep Med.*, 8(6):613–622, 2007.

[173] Roseanne Armitage, Robert Hoffmann, Madhukar Trivedi, and A. John Rush. Slow-wave activity in nrem sleep: sex and age effects in depressed outpatients and healthy controls. *Psychiatry Res.*, 95(3):201–213, 2000.

[174] R. A. Wever. Sex differences in human circadian rhythms: Intrinsic periods and sleep fractions. *Cell. Mol. Life Sci.*, 40(11):1226–1234, 1984.

[175] B. B. Fredholm. Are methylxanthine effects due to antagonism of endogenous adenosine? *Trends Pharmacol. Sci.*, 1:129–132, 1980.

[176] A. Nehlig, J. Daval, and G. Debry. Caffeine and the central nervous system: mechanisms of action, biochemical, metabolic and psychostimulant effects. *Brain Res. Rev.*, 17:139–170, 1992.

[177] T. Mochizuki, A. Crocker, S. McCormack, M. Tanagisawa, T. Sakurai, and T. E. Scammell. Behavioral state instability in orexin knock-out mice. *J. Neurosci.*, 24:6291–6300, 2004.

[178] M. H. Silber, L. E. Krahn, E. J. Olson, and S. Pankratz. The Epidemiology of Narcolepsy in Olmsted County, Minnesota: A Population-Based Study. *Sleep*, 25:197–202, 2002.

[179] C. R. Baumann and C. L. Bassetti. Hypocretins (orexins): clinical impact of the discovery of a neurotransmitter. *Sleep Med. Rev.*, 9:253–268, 2005.

[180] J. P. Kukkonen, T. Holmqvist, S. Ammoun, and K. E. O. Akerman. Functions of the orexinergic/hypocretinergic system. *Am. J. Physiol. Cell Physiol.*, 283:1567–1591, 2002.

[181] M. Mieda, S. C. Williams, C. M. Sinton, J. A. Richardson, T. Sakurai, and M. Yanagisawa. Orexin neurons function in an efferent pathway of a food-entrainable circadian oscillator in eliciting food-anticipatory activity and wakefulness. *J. Neurosci.*, 24:10493–10501, 2004.

[182] J. K. Young, M. Wu, K. F. Manaye, P. Kc, J. S. Allard, S. O. Mack, and M. A. Haxhiu. Orexin stimulates breathing via medullary and spinal pathways. *J. Appl. Physiol.*, 98:1387–1395, 2005.

[183] A. Yamanaka, Y. Muraki, N. Tsujino, K. Goto, and T. Sakurai. Regulation of orexin neurons by the monoaminergic and cholinergic systems. *Biochem. Biophys. Res. Commun.*, 303(1):120–129, 2003.

[184] S. Zhang, J. M. Zeitzer, Y. Yoshida, J. P. Wisor, S. Nishino, D. M. Edgar, and E. Mignot. Lesions of the Suprachiasmatic Nucleus Eliminate the Daily Rhythm of Hypocretin-1 Release. *Sleep*, 27:619–627, 2004.

[185] M. M. Thakkar, S. C. Engemann, K. M. Walsh, and P. K. Sahota. Adenosine and the homeostatic control of sleep: Effects of A1 receptor blockade in the perifornical lateral hypothalamus on sleep-wakefulness. *Neuroscience*, 153(4):875–880, 2008.

[186] R. Liu, A. N. van den Pol, and G. K. Aghajanian. Hypocretins (orexins) regulate serotonin neurons in the dorsal raphe nucleus by excitatory direct and inhibitory indirect actions. *J. Neurosci.*, 22(21):9453–9464, 2002.

[187] T. L. Horvath, C. Peyron, S. Diano, A. Ivanov, G. Aston-Jones, T. S. Kilduff, and A. N. van den Pol. Hypocretin (Orexin) Activation and Synaptic Innervation of the Locus Coeruleus Noradrenergic System. *J Comp. Neurol.*, 415:145–159, 1999.

[188] K. S. Eriksson, O. Sergeeva, R. E. Brown, and H. L. Haas. Orexin/hypocretin excites the histaminergic neurons of the tuberomammillary nucleus. *J. Neurosci.*, 21(23):9273–9279, 2001.

[189] Y. Muraki, A. Yamanaka, N. Tsujino, T. S. Kilduff, K. Goto, and T. Sakurai. Serotonergic Regulation of the Orexin/Hypocretin Neurons through the 5-HT1A Receptor. *J. Neurosci.*, 24(32):7159–7166, 2004.

[190] E. Eggermann, M. Serafin, L. Bayer, D. Machard, B. Saint-Mleux, B. E. Jones, and M. Mühlethaler. Orexins/hypocretins excite basal forebrain cholinergic neurones. *Neuroscience*, 108(2):177–181, 2001.

[191] Z. Liu and X. Gao. Adenosine inhibits activity of hypocretin/orexin neurons by the a1 receptor in the lateral hypothalamus: A possible sleep-promoting effect. *J. Neurophysiol.*, 97:837–848, 2007.

[192] J. M. Zeitzer, C. L. Buckmaster, K. J. Parker, C. M. Hauck, D. M. Lyons, and E. Mignot. Circadian and homeostatic regulation of hypocretin in a primate model: Implications for the consolidation of wakefulness. *J. Neurosci.*, 23(8):3555–3560, 2003.

[193] P. M. Fuller, J. J. Gooley, and C. B. Saper. Neurobiology of the sleep-wake cycle: Sleep architecture, circadian regulation, and regulatory feedback. *J. Biol. Rhythms*, 21(6):482–493, 2006.

[194] G. Mayer, F. Hellmann, E. Leonhard, and K. Meier-Ewert. Circadian Temperature and Activity Rhythms in Unmedicated Narcoleptic Patients. *Pharmacol. Biochem. Behav.*, 58:395–402, 1996.

[195] P. Tassi and A. Muzet. Sleep inertia. *Sleep Med. Rev.*, 4:341–353, 2000.

[196] T. Akerstedt, M. Billiard, M. Bonnet, G. Ficca, L. Garma, M. Mariotti, P. Salzarulo, and H. Schulz. Awakening from sleep. *Sleep Med. Rev.*, 6 (4):267–286, 2002.

[197] M. A. Carskadon and W. C. Dement. Multiple Sleep Latency Tests During the Constant Routine. *Sleep*, 15:396–399, 1992.

[198] D. F. Dinges and R. J. Broughton. *Sleep and alertness: chronobiological, behavioral, and medical aspects of napping*. Raven Press, New York, 1989.

[199] B. Edwards, J. Waterhouse, and T. Reilly. Circadian rhythms and their association with body temperature and time awake when performing a simple task with the dominant and non-dominant hand. *Chronobiol. Int.*, 25(1):115–132, 2008.

[200] M. M. Mitler, M. A. Carskadon, C. A. Czeisler, W. C. Dement, D. F. Dinges, and R. C. Graeber. Catastrophes, sleep, and public policy: Consensus report. *Sleep*, 11(1):100–109, 1988.

[201] M. F. Wu, S. A. Gulyani, E. Yau, E. Mignot, B. Phan, and J. M. Siegel. Locus coeruleus neurons: cessation of activity during cataplexy. *Neuroscience*, 91(4):1389–1399, 1999.

[202] M. F. Wu, J. John, L. N. Boehmer, D. Yau, G. B. Nguyen, and J. M. Siegel. Activity of dorsal raphe cells across the sleep-waking cycle and during cataplexy in narcoleptic dogs. *J. Physiol.*, 554(1):202–215, 2004.

[203] J. John, M. F. Wu, L. N. Boehmer, and J. M. Siegel. Cataplexy-active neurons in the hypothalamus: Implications for the role of histamine in sleep and waking behavior. *Neuron*, 42(4):619–634, 2004.